Explaining spatial adjustments in the global atmospheric water cycle under multiple climate forcings

by

Kyle B. Heyblom
B.Eng., McMaster University, 2020

A Dissertation Submitted in Partial Fulfillment of the
Requirements for the Degree of

DOCTOR OF PHILOSOPHY

in the School of Earth and Ocean Sciences

Explaining spatial adjustments in the global atmospheric water cycle under multiple climate forcings

by

Kyle B. Heyblom
B.Eng., McMaster University, 2020

Supervisory Committee

Dr. Adam Monahan, Supervisor
(School of Earth and Ocean Sciences)

Dr. Nathan Gillett, Departmental Member
(Canadian Centre for Climate Modeling and Analysis, Environment and Climate Change Canada; School of Earth and Ocean Sciences)

Dr. Alex Cannon, Departmental Member
(Climate Research Division, Environment and Climate Change Canada; School of Earth and Ocean Sciences)

Dr. Tara Troy, Outside Member
(Department of Civil Engineering)

Dr. Adriana Bailey, Additional Member
(Department of Climate and Space Sciences and Engineering, University of Michigan)

ABSTRACT

This dissertation examines the response of the global atmospheric water cycle to various climate forcings, with a focus on understanding how and why spatial patterns of the water cycle adjust. Through a combination of model experiments and theoretical analysis, this research identifies key mechanisms driving the spatial redistribution of atmospheric water cycle attributes in a changing climate. The findings are presented in three core chapters.

The first chapter investigates the impact of variability in aerosol emissions, particularly from biomass burning, on the global hydrologic cycle. Using Earth System Model simulations, the study shows that increased variability in biomass burning emissions amplifies evaporation, atmospheric moisture, and precipitation. Regional factors, such as ocean heat storage and meridional energy transport, modulate the extent of these amplifications. This chapter underscores the significant influence of emission variability on regional hydrological projections and calls for more consistent modeling approaches in future multimodel projection efforts.

The second chapter further explores aerosol variability, specifically how interannual fluctuations in biomass burning emissions reduce the time-averaged magnitude of aerosol forcing. This work presents a mechanism that explains the intensification of the hydrologic cycle under increased aerosol variability described in the first chapter. It highlights that many emissions inventories overlook this variability, leading to possible overestimation of the cooling effect of aerosols and misrepresent the associated hydrological changes. The findings emphasize the need for improved representation of aerosol variability in climate models to better capture the spatial adjustments of the water cycle.

The third chapter introduces a new framework for understanding regional precipitation changes. This framework identifies three dominant contributors to regional precipitation shifts: global changes in evaporation, adjustments to the moisture cycling rate, and changes in atmospheric circulation. A key conclusion is that the global moisture cycling rate plays a critical role in explaining the spatial patterns of zonal-mean precipitation changes under warming. Furthermore, this control of the global moisture cycling rate on zonal-mean precipitation is robust under all forcing drivers investigated. This framework provides a mechanistic understanding of regional precipitation shifts and enhances our ability to predict these changes under various warming scenarios.

Contents

Supervisory Committee **ii**

Abstract **iii**

Table of Contents **iv**

List of Figures **vii**

Acknowledgements **xxii**

Dedication **xxiv**

1 Introduction **1**

2 The effect of variable aerosol emissions on the global hydroclimate **4**

2.1 Introduction 5

2.2 Model data 7

2.3 Cloud and surface radiative response 8

2.4 Hydrologic cycle response 8

2.5 Moderating factors to hydrologic cycle amplification 12

2.6 Implications 15

2.A Appendix to Chapter 2 17

2.A.1 Evaluating spatial statistical significance 17

2.A.2 Evaluating area-averaged statistical significance 18

2.A.3 Supplementary figures 18

3 Why aerosol emissions variability leads to large-scale surface warming **24**

3.1 Introduction 25

3.2 Methods 26

3.3 Results . . . 28
3.3.1 The effects of emissions variability on the aerosol forcing . . . 28
3.3.2 Differences in forcing are driven by differences in the cloud radiative effect . . . 30
3.3.3 Differences in cloud radiative effect are due to nonlinear aerosol-cloud interactions . . . 32
3.4 Discussion . . . 36
3.4.1 A need for more idealized experiments . . . 36
3.4.2 Implications . . . 36
3.A Appendix to Chapter 3 . . . 38
3.A.1 CESM2 Large Ensemble . . . 38
3.A.2 Aerosol emission and concentration calculations . . . 39
3.A.3 Forcing calculation . . . 39
3.A.4 Aquaplanet simulations . . . 40
3.A.5 Idealized aerosol-CRE response . . . 40
3.A.6 CMIP6-AMIP data . . . 42
3.A.7 Evaluating statistically-robust evidence of emissions-CRE nonlinearity . . . 42
3.A.8 Evaluating spatial statistical significance . . . 43
3.A.9 Supplementary figures . . . 43

4 An updated framework to understand regional mean precipitation change under warming 50
4.1 Introduction . . . 51
4.2 The role of changing moisture cycling rates on regional precipitation . 54
4.2.1 Zonal-mean precipitation response controlled by redistribution of precipitation sources . . . 54
4.2.2 Evaporation–divergence ratios play a dominant role in redistributing precipitation sources . . . 57
4.2.3 Important aspects of precipitation change explained by global moisture cycling rate . . . 60
4.3 Reduced moisture cycling rates with warming associated with robust moisture transport distance lengthening . . . 62
4.3.1 Robust moisture transport distance increases under warming across Earth System Models . . . 63

4.3.2 Lengthened moisture transport distance consistent with slowed moisture cycling rate . . . 63
4.3.3 Circulation and high latitude evaporation act to moderate moisture transport distance increase . . . 65
4.4 A simple and mechanistic framework for regional precipitation change 67
4.5 Moisture cycling rate important to regional precipitation across multiple forcing drivers under global surface temperature adjustment . . . 70
4.6 Conclusions . . . 73
4.A Appendix to Chapter 4 . . . 76
4.A.1 Moisture transport box model approximation and calculation of moisture transport length scale . . . 76
4.A.2 CMIP6 data . . . 77
4.A.3 PDRMIP data . . . 77
4.A.4 Calculation of total, fast, and slow responses . . . 78

5 Conclusion **79**
5.1 Summary and significance of key findings . . . 79
5.1.1 Chapter 2: Summary and significance of key findings . . . 79
5.1.2 Chapter 3: Summary and significance of key findings . . . 80
5.1.3 Chapter 4: Summary and significance of key findings . . . 81
5.2 Synthesis of Results . . . 82
5.3 Future Directions . . . 82

Bibliography **84**

List of Figures

Figure 2.1 **Aerosol emission scenarios and resulting differences in cloud and radiative responses.** Panel (a) shows the annual mean sum of black carbon, primary organic, and sulfate aerosol surface fluxes from HiVarBB (black line) and SmoothBB (red line) ensemble sets averaged from 40–70°N, with the vertical gray dashed lines delineating the GFED period (1997–2014). Panels (b-d) show ensemble mean differences (average of HiVarBB ensemble members minus average of SmoothBB ensemble members) in (b) vertically-integrated cloud droplet number concentration (CDNC), in 10^9 m^{-2}; (c) net surface shortwave flux, in W m^{-2}; and (d) surface temperature, in K, during the GFED period (1997–2014). Stippling signifies 95% confidence in the significance of the difference between ensemble member sets (see Appendix 2.A.1). 9

Figure 2.2 **Differences in the atmospheric hydrologic cycle.** (a,b) latent heat flux, in W m^{-2}; (c,d) column-integrated precipitable water, in kg m^{-2}; (e,f) total precipitation, in mm day^{-1}; (g,h) percentage of precipitation that is liquid; and (i,j) annual maximum daily precipitation (Rx1day) in mm day^{-1}. The left column shows the ensemble mean difference (average of HiVarBB ensemble members minus average of SmoothBB ensemble members), with stippling signifying 95% confidence (see Appendix 2.A.1). The right column shows the annual mean value, averaged from 40–90°N, in HiVarBB (black line) and SmoothBB (red line) ensemble members; thick lines denote the ensemble mean, shading denotes the range of each ensemble member set, and vertical gray dashed lines delineate the GFED period (1997–2014). 11

Figure 2.3 **Energetic limitations on hydrologic cycle amplification.** (a) upper (top 100 m) ocean heat content anomalies relative to the 1950–1979 average from 40–90°N in HiVarBB (black line) and SmoothBB (red line) simulations, in ZJ; and (b) ensemble mean difference (average of HiVarBB ensemble members minus average of SmoothBB ensemble members) in the meridional northward energy transport during the GFED period (1997–2014), in PW, including total (ΔTET; black line), atmospheric (ΔAET; yellow line), and ocean (ΔOHT; cyan line) components. In (a), thick lines denote the ensemble mean, while shading denotes the range of each member set. In (b), solid lines signify 95% confidence in the significance of the difference between HiVarBB and SmoothBB ensemble member sets (see Appendix 2.A.1). 13

Figure 2.4 **Precipitation efficiency and factors that impact it.** (a) total precipitation efficiency, in 10^{-6} s^{-1}, in HiVarBB (black line) and SmoothBB (red line) simulations, with the vertical gray dashed lines delineating the GFED period (1997–2014); (b) ensemble mean difference in the mean 40–90°N vertical moist potential temperature profile, in K; and (c) ensemble mean difference in zonal mean relative humidity from 40–90°N, in %. In (a), thick lines denote the ensemble mean, while the shaded regions denote the range of each ensemble member set. In (b) and (c), the ensemble mean differences are computed as the average of HiVarBB ensemble members minus the average of SmoothBB ensemble members during the GFED period (1997–2014). In (b), the solid line signifies 95% confidence in the significance of the difference between ensemble member sets (see Appendix 2.A.1). In (c), stippling signifies 95% confidence in the significance of the difference between ensemble member sets (see Appendix 2.A.1). 15

Figure 2.A1 **Statistical significance of area-averaged differences in the atmospheric hydrologic cycle.** (a) latent heat flux, in W m^{-2}; (b) column-integrated precipitable water, in kg m^{-2}; (c) total precipitation, in mm day^{-1}; (d) percentage of precipitation that is liquid; and (e) annual maximum daily precipitation (Rx1day) in mm day^{-1}, all from 40-90°N over the GFED period (1997–2014). The gray histogram shows a probability density distribution of means derived from a non-parametric bootstrapping test (see Appendix 2.A.2), and the blue shading indicates the region outside of the (two-sided) 95% confidence intervals; the difference between HiVarBB and SmoothBB ensemble means (red line) is statistically significant (at the 95% level) if it falls within the blue shaded region. 19

Figure 2.A2 **Differences in seasonal relative liquid precipitation.** The left and middle columns are the same as in Figure 2.2, but showing differences in percentage of precipitation that is liquid in (a-c) March-May (MAM), (d-f) June-August (JJA), (g-i) September-November (SON), (j-l) and December-February (DJF). The right column shows the statistical significance of the difference in HiVarBB and SmoothBB ensemble means from 40-90°N over the GFED period. The gray histogram shows a probability density distribution of means derived from a non-parametric bootstrapping test (see Appendix 2.A.2), and the blue shading indicates the region outside of the (two-sided) 95% confidence intervals. The difference between HiVarBB and SmoothBB ensemble means (red line) is statistically significant (at the 95% level) if it falls within the blue shaded region. 20

Figure 2.A3 **Statistical significance of area-averaged differences in moderating factors.** (a) precipitation efficiency, and (b) upper (top 100 m) ocean heat content from 40-90°N during the GFED period (1997–2014). The gray histogram shows a probability density distribution of means derived from a non-parametric bootstrapping test (see Appendix 2.A.2), and the blue shading indicates the region outside of the (two-sided) 95% confidence intervals. The difference between HiVarBB and SmoothBB ensemble means (red line) is statistically significant (at the 95% level) if it falls within the blue shaded region. 21

Figure 2.A4 **Zonal-mean ensemble mean difference of mechanisms affecting the precipitation efficiency.** (a) black carbon concentration (in ng/kg), (b) specific humidity (in g/kg), (c) shortwave heating rate (in 10^{-7} K/s) from 40-90°N. Ensemble mean differences are computed as as the average of HiVarBB ensemble members minus the average of SmoothBB ensemble members during the GFED period (1997–2014). Stippling signifies 95% confidence in the significance of the difference between ensemble member sets (see Appendix 2.A.1). 22

Figure 2.A5 **Differences in meridional atmospheric energy transport components.** Ensemble mean difference (average of HiVarBB ensemble members minus average of SmoothBB ensemble members) in the total atmospheric energy transport (ΔAET_{total}, yellow line), latent heat transport (ΔLHT, blue line), and dry static energy transport (ΔAET_{dry}, red line) during the GFED period (1997–2014), in PW. Solid lines signify 95% confidence in the significance of the difference between HiVarBB and SmoothBB ensemble member sets (see Appendix 2.A.1). 23

Figure 2.A6 **Differences in Atlantic meridional overturning circulation (AMOC).** (a) zonal-mean ensemble mean difference (average of HiVarBB ensemble members minus average of the SmoothBB ensemble members), (b) annual mean Atlantic meridional overturning maximum from HiVarBB (black curve) and SmoothBB (red curve) ensemble members; thick lines denote the ensemble mean, shading denotes one standard deviation of each ensemble member set, and horizontal gray dotted lines delineate the GFED period (1997–2014), and (c) statistical significance of the difference in Atlantic meridional overturning maximum ensemble means during the GFED period. The gray histogram shows a probability density distribution of means derived from a non-parametric bootstrapping test (see Appendix 2.A.2), and the blue shading indicates the region outside of the (two-sided) 95% confidence intervals. The difference between HiVarBB and SmoothBB ensemble means (red line) is statistically significant (at the 95% level) if it falls within the blue shaded region. 23

Figure 3.1 **Biomass burning (BB) emissions used for CMIP6 and the effect of high BB emissions variability on surface temperature in CESM2.** Panel (a) shows the annual mean biomass burning (BB) emissions averaged over 50–70°N prescribed for CMIP6 (black line) and a second smoothed emissions inventory used for 50 members of the Community Earth System Model Large Ensemble version 2 (CESM2-LE) over the recent historical period (red line), in particles m^{-2} min^{-1} (Appendix 3.A.1). The vertical grey dashed lines delineate the period of high BB emissions variability in the CMIP6 prescribed BB emissions (1997–2014). Panel (b) shows the difference in surface temperature between the CMIP6 emissions ensemble members and smoothed BB emissions ensemble members in the CESM2-LE during 1997–2014 (average of 50 CMIP6 emissions ensemble members minus average of 50 smoothed BB emissions ensemble members; in °C). Stippling signifies 90% confidence (Appendix 3.A.8). See Appendix 3.A.1 for a further description of CESM2-LE and BB emissions therein. 27

Figure 3.2 **Idealized simulations to quantify changes in effective radiative forcing (ERF) due to biomass burning (BB) emissions variability.** The center image shows the time-integrated emissions rate of BB emissions for all scenarios (in particles m^{-2} min^{-1}; Appendix 3.A.2) in red, while the surrounding insets show the time evolution of BB emissions from Zero-Var, Real-Var, and Pulse-Var (black, green, and brown lines, respectively) at selected locations. 29

Figure 3.3 **Change in effective radiative forcing (ERF) and cloud properties due to biomass burning emissions variability.** Panel (a) shows the June–September (JJAS) mean absolute ERF due to BB emissions in the Zero-Var experiment (relative to no BB emissions). Panels (b)–(g) show the JJAS mean change in ERF (b and c; denoted $\Delta\text{ERF}_{\text{BBVar}}$; in W m^{-2}), vertically integrated cloud droplet number concentration (d and e; CDNC; in 10^9 m^{-2}), and total (long and shortwave) cloud radiative effect (f and g; CRE; in W m^{-2}) due to BB emissions variability in the Real-Var (left column) and Pulse-Var (right column) experiments. Changes due to BB emissions variability are defined as the variability experiments minus the Zero-Var experiment. Stippling signifies 90% confidence (Appendix 3.A.8). 31

Figure 3.4 **Responses of CDNC and CRE to varying aerosol emissions** for June–September (JJAS) averaged over 50–70°N, relative to the Zero-Var simulations unless otherwise stated. The left column shows the relationship between column-integrated aerosol concentrations (in W m^{-2}; Appendix 3.A.2) and (a) column-integrated CDNC (in 10^9 m^{-2}) or (b) CRE (in W m^{-2}) for a collection of years (number of years displayed in the legend) drawn from each experiment. The average and range of that collection is shown by marker and whiskers. The "High" and "Low" statistics are produced by averaging the years which do and do not have BB emissions in the Pulse-Var experiment, respectively. "Fixed emissions" experiments are run under the same conditions as the Zero-Var experiments, however, use varying scaled BB emissions. CESM2-LE probability density functions (PDF) represent changes of each year in the high BB emissions variability simulations relative to the ensemble annual mean from the low BB emissions variability simulations of the CESM2-LE historical simulations from 1997 to 2014 (see Appendix 3.A.1 for a description of different CESM2-LE ensemble members). The right column shows the time evolution of the of CDNC and CRE from the Zero-Var, Real-Var, and Pulse-Var simulations. The horizontal dashed line represents the JJAS mean for the entire simulation period. 34

Figure 3.5 **Idealized cloud radiative effect (CRE) response to varying aerosol concentrations.** Panel (a) shows probability density functions (PDF) of aerosol concentrations representative of Real-Var and Zero-Var BB emissions scenarios (green and black, respectively). Panel (b) shows the cloud radiative effect (CRE) response to aerosol concentration derived from CESM2 (nonlinear; solid purple) and a linear response (dashed purple). Panel (c) shows the resulting CRE PDFs from the nonlinear and linear aerosol-CRE responses (solid and dashed lines, respectively). Vertical and horizontal lines in panels (a) and (c) represent the mean aerosol concentration and CRE, respectively, of each distribution. Panel (d) shows a 100-year aerosol concentration time series randomly drawn from the high and zero aerosol emissions variability PDFs (green and black lines, respectively). Panel (e) shows the resulting CRE from aerosol concentrations shown in panel (d) from the nonlinear and linear aerosol-CRE responses (solid and dashed lines, respectively). 35

Figure 3.A1 **Variability of biomass burning (BB) column-integrated burden in each idealized experiment.** Shown is the standard deviation of BB column-integrated burden (in 10^{12} particles m^{-2}) in the Real-Var (a and b) and Pulse-Var (c and d) experiments for annual (a and c) and June–September (JJAS; b and d) means. 44

Figure 3.A2 **Change in annual effective radiative forcing due to biomass burning emissions variability (ΔERF_{BBVar}).** Panel (a) shows the absolute ERF due to BB emissions in the Zero-Var experiment (relative to no BB emissions). ΔERF_{BBVar} is shown for the Real-Var (Panel (b)) and Pulse-Var (Panel (c)) experiments. ΔERF_{BBVar} is defined as the variability experiments minus the Zero-Var experiment. Stippling signifies 90% confidence (see Appendix 3.A.7). 45

Figure 3.A3 **Annual mean change in cloud properties due to biomass burning (BB) emissions variability.** Annual mean change in cloud droplet number concentration (CDNC; in 10^9 m^{-2}; (a) and (b)) and cloud radiative effect (CRE; in W m^{-2}; (c) and (d)) due to BB emissions variability in the Real-Var (left column) and Pulse-Var (right column) experiments. Changes due to BB emissions variability are defined as the variability experiments minus the Zero-Var experiment. Stippling signifies 90% confidence (see Appendix 3.A.7). 46

Figure 3.A4 **Change in cloud amount due to biomass burning (BB) emissions variability.** June–September (JJAS) mean change in liquid water path (LWP; in 10^{-2} kg m^{-2}; (a) and (b)) and fraction ((c) and (d)) due to BB emissions variability in the Real-Var (a) and Pulse-Var (b) experiments. Changes due to BB emissions variability are defined as the variability experiments minus the Zero-Var experiment. Stippling signifies 90% confidence (see Appendix 3.A.7). 47

Figure 3.A5 **Change in clear-sky top of atmosphere net radiative flux ($R_{TOA,clear}$) and surface albedo due to biomass burning (BB) emissions variability.** As in Figure 3.A4 but for $R_{TOA,clear}$ (in W m^{-2}; (a) and (b)) and surface albedo ((c) and (d)). 48

Figure 3.A6 **Change in cloud properties due to biomass burning (BB) emissions variability in aquaplanet simulations.** June–September (JJAS) mean change in cloud droplet number concentration (CDNC; in 10^9 m^{-2}; (a)) radiative effect (CRE; in W m^{-2}; (c)) due to BB emissions variability in the Real-Var experiment in an aquaplanet simulation. Changes due to BB emissions variability are defined as the variability experiments minus the Zero-Var experiment. Stippling signifies 90% confidence (see Appendix 3.A.7). 48

Figure 3.A7 **Cloud radiative effect (CRE) response at varying biomass burning (BB) emissions averaged in CMIP6-AMIP models.** Shown is the CRE response to varying BB emissions (shown as dry matter (DM) emissions) averaged from 50–70°N from data submitted to the CMIP6-AMIP historical simulations from 1997–2014. The number of ensemble members used for each model are shown in parentheses. See Appendix 3.A.5 for further information on data sources. CRE anomalies are relative to the monthly mean values. Black lines show linear regressions of the 80% most clean and polluted aerosol concentrations. P_{slope} (clean and polluted) refer to to the P-value of whether the slope is significant from zero for the clean and polluted regressions, respectively. P_{slope} (difference) refers to the P-value of whether the clean and polluted slopes are significantly different from each other. P-values highlight in blue (red) are (are not) significant to 90% confidence. 49

Figure 4.1 Zonal-mean precipitation change decomposed using a moisture transport framework, as described by Singh et al. (2016b) and expressed in Equation 4.3. Values are the multimodel ensemble mean from five different CMIP6 experiments. The legend in panel a describes which experiments are shown and the years that were averaged (in parentheses). Panel a shows the ensemble average zonal-mean precipitation change from each experiment. Panel b shows the change in precipitation amount that is explained by adjustments in the amount of evaporation from each source (holding relative contributions to each precipitation location constant; first term in Equation 4.3). Panel c shows the change in precipitation amount that is explained by adjustments in the relative contribution of each evaporative source to each precipitation sink (holding evaporation amount constant; second term in Equation 4.3). Panel d shows the nonlinear residual term in Equation 4.3. 56

Figure 4.2 Zonal-mean precipitation source redistribution ($\mathbf{X_e}'E$; from Equation 4.3) decomposed into contributions described by Equations 4.6, 4.10, and 4.11. Values are the multimodel ensemble mean from five different CMIP6 experiments. Changes are relative to the annual mean from each model's respective pre-industrial control simulation. The legend in panel a describes which experiments are shown and the years that were averaged (in parentheses). Dashed lines in all panels represent the total zonal-mean precipitation source redistribution ($\mathbf{X_e}'E$; also shown in Figure 4.1c). Panel a shows the precipitation source redistribution response resulting from adjustments to the evaporation–divergence ratio ($(\eta - \alpha)\nabla \cdot Q$; first term in Equation 4.6). Panel b shows the precipitation source redistribution response resulting from changes in the spatial pattern of evaporation ($\tilde{\eta}P - \mathbf{X_e}(\tilde{\eta}E)$; second term in Equation 4.6). Panel c shows the precipitation source redistribution response resulting from adjustments to the ratio of evaporation to near-surface air moisture ($\frac{\gamma'}{\gamma}\nabla \cdot Q$; first term in Equation 4.10). Panel d shows the precipitation source redistribution response resulting from the residual moisture divergence response (defined in Equation 4.9; $-\alpha_r \nabla \cdot Q$; second term in Equation 4.10). Panel e shows the precipitation source redistribution as approximated by changes in the global moisture cycling rate ($\frac{\overline{\gamma}'}{\overline{\gamma}}\nabla \cdot Q$). 59

Figure 4.3 Changes in water cycling rate and meridional moisture transport distance across multiple CMIP6 warming experiments. Top panel shows the global mean change in near-surface air moisture (a; $\overline{Q}_s'$), global-mean evaporation (b; $\overline{E}'$), global moisture cycling rate (c; $\overline{\gamma}'$), and global-mean meridional moisture transport distance (d; $\overline{\lambda}_p'$; as defined in Appendix 4.A.1). Values represent the ensemble member average from each model (described in legend; number of ensemble members used reported in parentheses). Panel e shows the change in meridional moisture transport length distance at each latitude. Values are the multimodel ensemble mean from each CMIP6 experiment (colors shown in legend). Panel f shows the relationship between global moisture cycling rate and meridional transport distance across each CMIP6 model and experiment ensemble mean. The black line represents a linear regression across all ESMs and experiments and corresponds to the equation and correlation coefficient shown on plot. 64

Figure 4.4 Changes in meridional moisture transport distance as approximated by the global moisture cycling rate across multiple CMIP6 warming experiments. Solid lines show the approximated moisture transport distance ($\hat{\lambda}'_{p,\overline{\gamma}'}$). Dashed lines show the actual moisture transport distance change (λ'_p; same as Figure 4.3e). Values are the multimodel ensemble mean from each CMIP6 simulations (colors shown in legend). 66

Figure 4.5 Changes in zonal-mean precipitation as approximated by adjustments in global mean evaporation ($\overline{\eta}$), the global water cycling rate ($\overline{\gamma}'$), and the residual moisture divergence response (α_r), which appear in Equation 4.13. Results shown represent the multimodel ensemble mean from the CMIP6 Abrupt 4xCO_2 experiment. The black dashed line represents the simulated zonal-mean precipitation response. The blue line represents a change in zonal-mean precipitation when approximated using only the response in global evaporation (first term in Equation 4.13). The red line represents a change in zonal-mean precipitation when also accounting for adjustments in the global moisture cycling rate (first two terms in Equation 4.13). The pink line represents a change in zonal-mean precipitation when accounting for all three terms in Equation 4.13. 69

Figure 4.6 Changes in zonal-mean precipitation as approximated by adjustments in global evaporation ($\overline{\eta}$), the global moisture cycling rate ($\overline{\gamma}'$), and residual moisture divergence response (α_r), which appear in Equation 4.13. Results shown represent multimodel means of total (left column), slow (middle column), and fast (right column) response of the three terms in Equation 4.13 from various PDRMIP forcing scenario experiments. Black dashed lines represent the simulated zonal-mean precipitation responses. Blue lines represent a change in zonal-mean precipitation when approximated using only the response in global evaporation (first term in Equation 4.13). Red lines represent a change in zonal-mean precipitation when also accounting for adjustments in the global-mean moisture cycling rate (first two terms in Equation 4.13). Pink lines represent a change in zonal-mean precipitation when accounting for all three terms in Equation 4.13. 72

Figure 4.7 Relationship between global-mean atmospheric moisture cycling rate and meridional moisture transport distance across each PDRMIP models and forcing scenarios. Shown are global-mean total (left), slow (middle), and fast (right) responses. The black line represents a linear regression across all models and experiments and corresponds to the equation and correlation coefficient shown on each plot. 73

Figure 4.A1 **One-dimensional meridional moisture transport box model.** P_i, E_i, F_i represent the zonal mass of precipitation, evaporation, and column-integrated moisture transport at latitude location i. 76

ACKNOWLEDGEMENTS

First, to my mentor, Hansi Singh: Thank you for your nearly four years of supervision. Your guidance fostered immense academic, professional, and personal growth for me. I am deeply grateful for how you helped shape me into the researcher I am today, and I will always be thankful for your support.

Second, to Adriana Bailey: From the beginning of my graduate studies, I thoroughly enjoyed working with you. It was with great pleasure to receive your direct mentorship over the past year. Learning from and working closely with you accelerated my development as a researcher. I am grateful that you stepped in to support me at a time when I needed it. Your influence will always make me better in the work I do.

Third, to Adam Monahan: Thank you for taking over as my supervisor. In a world where time and attention are our most valuable assets, I deeply appreciate that you dedicated yours to guiding me. Your advice and support have been instrumental in getting me to this point.

Further, thank you to the rest of my supervisory committee: Nathan Gillett, Alex Cannon, and Tara Troy. Your insights and guidance throughout my studies have been invaluable.

I would also like to thank Phil Rasch. Your expertise, guidance, and mentorship made so much of this work possible. I am grateful for the time and attention you invested in me.

I extend my thanks to everyone else I had the pleasure of working with during the research for this dissertation. In particular, I want to thank Haruki Hirasawa and Patricia DeRepentigny for your collaboration on the work included within.

Finally, I want to thank all the friends I've made along the way at the University of Victoria. You have made my time here a true pleasure.

In nature nothing exists alone.
Rachel Carson, Silent Spring

This work was supported by a Canada Graduate Scholarships - Doctoral program award from the Natural Sciences and Engineering Research Council of Canada.

DEDICATION

For my parents, Caroline and Duncan, whose unwavering love and lifelong support have been the cause for everything I have achieved.

Chapter 1

Introduction

The global water cycle describes the continuous movement of water throughout Earth's atmosphere, oceans, land, and cryosphere via processes such as evaporation, condensation, precipitation, and runoff. This transport of water in vapor, liquid, and solid phases sustains ecosystems and regulates the climate by redistributing mass and energy on a large scale (Peixoto and Oort, 1992). Like all living organisms, humans are deeply dependent on the water cycle, with the atmospheric component playing a particularly crucial role. It governs when, where, and how much evaporation and precipitation occur, affecting weather patterns, agricultural productivity, and freshwater availability. Oceanic evaporation, for instance, is the primary source of freshwater used for drinking, agriculture, and industry (Gimeno et al., 2012; Schewe et al., 2014; D'Odorico et al., 2018; Djehdian et al., 2019). Freshwater is undeniably the most essential natural resource on Earth (Mekonnen and Hoekstra, 2016; Djehdian et al., 2019), underpinning nearly all of the United Nations' Sustainable Development Goals (Miranda et al., 2023).

Disruptions to the water cycle, particularly those driven by human activities, can lead to extreme weather events, water scarcity, and ecosystem imbalances, with profound implications for human well-being and economic stability (Douville et al., 2021; Caretta et al., 2023). Climate-change-induced shifts in water availability or seasonal distribution have long been recognized by the United Nations Intergovernmental Panel on Climate Change and global development agencies as critical factors influencing food security and economic prosperity (Bates et al., 2008; Schewe et al., 2014; Mekonnen and Hoekstra, 2016; Caretta et al., 2023). As of 2016, over four billion people face severe freshwater scarcity for at least one month per year, and half a billion endure such scarcity year-round (Mekonnen and Hoekstra, 2016). With

global climate changes intensifying, the strain on human societies is expected to grow (Caretta et al., 2023). It is therefore essential to understand how the atmospheric water cycle is evolving and to develop accurate projections and better adapt to and mitigate future risks.

Despite significant progress in understanding how human-induced changes to our atmosphere, ocean, land, and cryosphere affect our atmospheric water cycle, important knowledge gaps remain (Douville et al., 2021, and references therein). One such gap pertains to how and why the spatial patterns of the water cycle change under climate forcing. This dissertation seeks to address this open area of research by investigating the mechanisms driving some of these spatial changes. Two central themes are explored: the influence of aerosol emission variability on the global water cycle and the role of the global moisture cycling rate in shaping spatial precipitation patterns under climate warming. At its core, this work argues that we can further improve our understanding of forced regional-scale changes of the global water cycle by employing our understanding of large-scale climate dynamics.

Chapter 2 investigates the impact of biomass burning emissions variability on water cycle amplification in high latitudes. Using Earth System Model simulation output, the analysis reveals that increased variability in biomass burning emissions leads to significant increases in atmospheric moisture, latent heat fluxes, and precipitation. Furthermore, this amplification is moderated by large-scale adjustments, including enhanced ocean heat storage and reduced meridional energy transport. These findings highlight the importance of considering emissions variability in Earth System Models, as it can markedly influence projections of future precipitation and atmospheric moisture distributions.

Chapter 3 delves into the mechanisms behind the influence of aerosol emissions variability on water cycle amplification. Specifically, it explores how temporal variability in emissions affects aerosol-cloud interactions and, consequently, aerosol radiative forcing. The study demonstrates, using a set of Earth System Model simulations, that interannual variability in emissions results in weaker time-averaged aerosol forcing compared to scenarios with temporally smoothed emissions. This outcome stems from nonlinear aerosol-cloud interactions, which are sensitive to emissions variability. These results underscore the necessity of accurately representing emissions variability in Earth System Models to improve projections of aerosol forcing and future climate change.

Chapter 4 presents a new framework for understanding regional mean precipita-

tion changes in response to climate forcing. The study identifies three key drivers of regional mean precipitation adjustments: changes in global evaporation, alterations in the global moisture cycling rate, and circulation changes that influence moisture transport. Of these, the global moisture cycling rate emerges as particularly important, as it determines the distance moisture travels before precipitating. This control of the global moisture cycling rate on zonal-mean precipitation is robust under all forcing drivers investigated. As warming slows the cycling rate, moisture is transported farther, redistributing precipitation from the subtropics to the deep tropics and extratropics. This mechanism provides a robust explanation for the well-known "wet-get-wetter, dry-get-drier" response to warming and is consistently observed across multiple Earth System Models. The proposed framework offers both interpretive and predictive insights into how regional mean precipitation may evolve under various climate scenarios.

The contents of Chapters 2 and 3 have been published as Heyblom et al. (2022) and Heyblom et al. (2023), respectively. At the time of writing, Chapter 4 has been submitted for consideration to the Journal of Climate.

Chapter 5 provides general conclusions.

Chapter 2

The effect of variable aerosol emissions on the global hydroclimate

Historical simulations performed for the Coupled Model Intercomparison Project Phase 6 (CMIP6) used biomass burning emissions between 1997–2014 containing higher spatial and temporal variability compared to emission inventories specified for earlier years, and compared to emissions used in previous (e.g., CMIP5) simulation intercomparisons. Using the Community Earth System Model version 2 (CESM2) Large Ensemble, we show this increased biomass burning emissions variability leads to amplification of the hydrologic cycle poleward of 40°N. Notably, the high variability of biomass burning emissions leads to increased latent heat fluxes, column-integrated precipitable water, and precipitation. Greater ocean heat uptake, weaker meridional energy transport from the tropics, greater atmospheric shortwave and longwave absorption, and lower relative humidity act to moderate this hydrologic cycle amplification. Our results suggest it is not only the secular changes (on multidecadal timescales) in biomass burning emissions that impact the hydrologic cycle, but also the shorter timescale variability in emissions.

The contents of this chapter were published in Geophysical Research Letters as *Increased Variability of Biomass Burning Emissions in CMIP6 Amplifies Hydrologic Cycle in the CESM2 Large Ensemble* (Heyblom et al., 2022).

2.1 Introduction

Many factors affect the atmospheric hydrologic cycle, and aerosols are among the most important of these factors. Aerosols impact regional and global scale precipitation through their direct radiative forcing and indirect microphysical effects (e.g., see Ramanathan et al., 2001; Szopa et al., 2021, and references therein). Simulation of the hydrologic cycle in historical and future projections is highly dependent on accurate modelling of aerosols. Indeed, aerosol-cloud interactions and their associated radiative forcing are among the most uncertain components of the historical radiative forcing of Earth's climate (Kiehl, 2007; Seinfeld et al., 2016; Smith et al., 2021; Szopa et al., 2021)

While aerosols are a topic of great interest to the climate community, comparatively little attention has been directed to how the variability of aerosol emissions affect the climate system (rather than the total amount of such emissions). Current knowledge is mostly based on scenarios which are inherently idealized. For example, the latest Geoengineering Model Intercomparison Project Phase 6 (GeoMIP6; Kravitz et al., 2015) experiments prescribe aerosol emissions as either constant in time, increasing at a fixed rate, or as an instantaneous change. Many others have used instantaneous change approaches to study the precipitation response to aerosols (Andrews et al., 2010; Kvalevåg et al., 2013; Ming et al., 2010; Richardson et al., 2016). Fast and slow precipitation responses (e.g., see Andrews and Forster, 2010; Bala et al., 2010) to aerosols were evaluated in the Precipitation Driver and Response Model Intercomparison Project (PDRMIP; Myhre et al., 2017; Samset et al., 2016) using a single instantaneous change in both black carbon and sulfate aerosol concentrations. Both the Model Intercomparison Project on the climatic response to volcanic forcing (VolMIP; Zanchettin et al., 2016) and the fourth phase of the Paleoclimate Model Intercomparison Project (PMIP4; Jungclaus et al., 2017) simulate the effect of volcanic emissions, which are necessarily episodic. However, the volcanic events simulated in these experiments are large and occur infrequently (i.e., they are years to decades apart). None of the above studies explore the climate impact of interannual emissions variability, or compare the impacts of variable aerosol emissions to continuous emissions.

Unlike the emissions used in many previous intercomparison activities, the biomass burning emissions prescribed for the sixth phase of the Climate Model Intercomparison Project (CMIP6) historical simulations (BB4CMIP6; see van Marle et al., 2017)

contain separate periods characterized by low and high interannual variability, thereby providing an opportunity to explore how such variability impacts the climate system. The methods and measurements used to construct this aerosol emission inventory utilized a variety of strategies over different intervals within the historical period (1850–2014) that produce different variability in estimated emissions. Between 1997 and 2014, the Global Fire Emissions Database version 4 with small fires (hereafter GFED; van der Werf et al., 2017) was used to estimate biomass burning emissions. These estimates include much higher temporal variability compared to prior years. Similar strategies were used for other aerosol sources (Hoesly et al., 2018). The interannual variability of black carbon, sulfate, and primary organics emissions prescribed between 40–70°N during 1997–2014 is approximately six times greater than the 18 years prior to it (as assessed from the standard deviation; see Figure 2.1a, black line). This large change in variability is new to the CMIP6 forcing and was not present in CMIP5, where decadal means were used to construct historical gridded biomass burning emissions (Lamarque et al., 2010). The prescribed biomass burning emissions largely consist of primary aerosols and reactive gases (van Marle et al., 2017), many of which result in the formation of secondary organic aerosols (Pandis et al., 1992).

Recent studies by DeRepentigny et al. (2022) and Fasullo et al. (2022) have compared the climate impacts of these (high variability) BB4CMIP6 emissions with simulations using emissions with less variability. Both studies find that it is not only the magnitude of aerosol emissions that impact the climate system, but also their temporal variability. Fasullo et al. (2022) showed that the sudden increase in aerosol emissions variability from 1997–2014 acts to decrease time-average cloud droplet number concentrations and low cloud amount, which increases downwelling shortwave radiation. DeRepentigny et al. (2022) further showed that greater variability in biomass burning emissions accelerated Arctic sea ice loss over this time period. Given that aerosols have a profound impact on the hydrologic cycle, a natural question that arises is the following: how does such a change in the temporal variability of biomass burning emissions affect the hydrologic cycle?

This study addresses this very question. Following the findings of DeRepentigny et al. (2022) and Fasullo et al. (2022), the Community Earth System Model version 2 Large Ensemble Community Project (CESM2-LE; Rodgers et al., 2021) forced half of its ensemble members with the original CMIP6 biomass burning emissions, and the second half with smoothed biomass burning emissions during the period of increased variability (from 1997–2014; Figure 2.1a, red line). Here, we utilize these two sets of

simulations to investigate the impact that this increase in biomass burning emissions variability has on the global atmospheric hydrologic cycle. We find the high variability of biomass burning emissions amplifies the atmospheric hydrologic cycle, defined here as increased evaporation, column-integrated precipitable water, and precipitation. Conversely, we find that several moderating factors act to mitigate this amplification of the hydrologic cycle. We conclude with a discussion of the implications of our findings for research utilizing CMIP6 output over the historical period.

2.2 Model data

We assess the impact of biomass burning emissions variability on the atmospheric hydrologic cycle using the Community Earth System Model version 2 Large Ensemble Community Project (CESM2-LE; Rodgers et al., 2021). This large ensemble project used the fully coupled CESM2 configured with the Community Atmosphere Model version 6 (CAM6; Danabasoglu et al., 2020), Parallel Ocean Program version 2 (POP2; Smith et al., 2010), Los Alamos Sea Ice Model version 5.1.2 (Hunke et al., 2015), and Community Land Model version 5 (CLM5; Lawrence et al., 2019). Aerosols were simulated using the four-mode version of the Modal Aerosol Module (MAM4; Liu et al., 2016). Each component was configured at a nominal 1° spatial resolution (Rodgers et al., 2021).

We analyze 80 CESM2-LE ensemble members subject to historical emissions (1850–2014) and the future SSP3-7.0 emissions (a medium-to-high emission scenario from 2015–2100; see O'Neill et al., 2016). Half of these 80 members were forced with the standard CMIP6 biomass burning emissions (hereafter HiVarBB; Figure 2.1a, black line; van Marle et al., 2017). The other half instead used a temporally smoothed biomass burning emission inventory (hereafter SmoothBB; Figure 2.1a, red line). This temporal smoothing was achieved by using an 11-year running mean filter from 1990–2020. This smoothing method reduced the interannual variability such that it aligned more closely with the variability of biomass burning emissions before the GFED period (1997–2014), but still nearly preserved the total cumulative amount of aerosol emissions through this period. Because fires varied from one year to another, the temporally smoothed emission inventory is also spatially smoother. The 80 members were initialized from four different years of the pre-industrial control simulation (years 1231, 1251, 1281, and 1301). Each initialization year was selected based on the phase of the Atlantic Meridional Overturning Circulation (AMOC) strength

(see Rodgers et al., 2021). Twenty members were started from each initialization year by randomly perturbing the temperature field. Half of each 20 member set used the HiVarBB emissions, while the other half used the SmoothBB emissions. In addition to differences in biomass burning emissions variability, the two ensemble member sets were forced with slight differences in SO_4 and SOAG emissions and CO_2 uptake which were the result of small bug corrections. These differences were determined to be too small to have an effect on climate results (Rodgers et al., 2021). We evaluate the relative impact of the increase in biomass burning variability by comparing the HiVarBB and SmoothBB simulations over the GFED period (1997–2014).

2.3 Cloud and surface radiative response

In the CESM2-LE, the choice of biomass burning emissions (HiVarBB or SmoothBB; Figure 2.1a, black and red lines, respectively) impacts clouds and surface radiation. Cloud droplet number concentrations (CDNC) are lower in ensemble members subjected to the CMIP6 biomass burning emissions relative to those subjected to the smoothed biomass burning emissions during the GFED period (i.e., the average of HiVarBB ensemble members minus the average of the SmoothBB ensemble members from 1997–2014; Figure 2.1b). The difference in CDNC is particularly large over the North American and Asian boreal forest regions. This time-integrated change in CDNC is likely due to a nonlinearity in CDNC response to aerosol emissions (as described by Carslaw et al., 2013). This cloud thinning effect in HiVarBB ensemble members, relative to SmoothBB ensemble members, leads to greater surface absorption of shortwave radiation (Figure 2.1c; see also DeRepentigny et al., 2022; Fasullo et al., 2022). This larger net surface shortwave radiation leads to surface warming in HiVarBB ensemble members relative to SmoothBB ensemble members during the GFED period (Figure 2.1d).

2.4 Hydrologic cycle response

We find that the hydrologic cycle amplifies when biomass burning emissions variability is high during the GFED period. Surface latent heat fluxes are greater in HiVarBB ensemble members compared to SmoothBB ensemble members over most of the area poleward of 40°N (Figure 2.2a). In general, regions with greater latent heat fluxes correspond to those that experience more surface shortwave heating (compare spatial

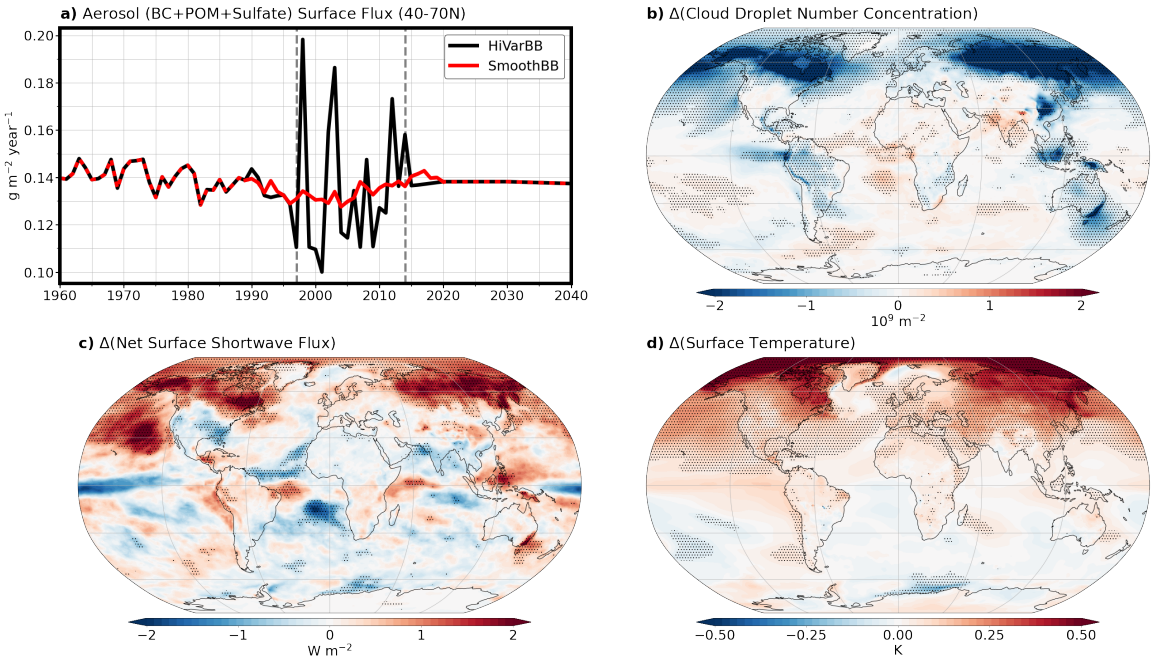

Figure 2.1: **Aerosol emission scenarios and resulting differences in cloud and radiative responses.** Panel (a) shows the annual mean sum of black carbon, primary organic, and sulfate aerosol surface fluxes from HiVarBB (black line) and SmoothBB (red line) ensemble sets averaged from 40–70°N, with the vertical gray dashed lines delineating the GFED period (1997–2014). Panels (b-d) show ensemble mean differences (average of HiVarBB ensemble members minus average of SmoothBB ensemble members) in (b) vertically-integrated cloud droplet number concentration (CDNC), in 10^9 m^{-2}; (c) net surface shortwave flux, in W m^{-2}; and (d) surface temperature, in K, during the GFED period (1997–2014). Stippling signifies 95% confidence in the significance of the difference between ensemble member sets (see Appendix 2.A.1).

patterns of net surface shortwave flux differences and latent heat flux differences in Figures 2.1c and 2.2a, respectively). These areas with larger latent heat flux are expected as more energy at the surface is available for evaporation (Peixoto and Oort, 1992). Poleward of 40°N, the surface latent heat flux is 0.8% (0.3 W/m^2) larger in the HiVarBB ensemble members compared to the SmoothBB ensemble members during the GFED period (Figures 2.2b, S1a).

These greater latent heat fluxes in the HiVarBB simulations are accompanied by greater column-integrated precipitable water over most of the Northern Hemisphere (NH) relative to the SmoothBB simulations (Figure 2.2c). Regional differences are statistically significant over most regions of the NH and all regions north of 30°N. Poleward of 40°N, the area-averaged column-integrated precipitable water is 1.4% (0.2 kg/m^2) larger in the HiVarBB simulations relative to the SmoothBB simulations (Figure 2.2d), a difference that is statistically significant (Figure 2.A1b). This difference corresponds to a 5.7% increase in water vapor per Kelvin of surface air warming, a rate smaller than expected from the Clausius–Clapeyron scaling factor of ∼7%/K (e.g., Trenberth et al., 2003; Held and Soden, 2006). This weaker scaling is consistent with a reduction in relative humidity (O'Gorman and Muller, 2010, also see Section 2.5).

Consistent with greater evaporation and atmospheric precipitable water, the HiVarBB emissions also increase precipitation over most regions poleward of 40°N relative to the SmoothBB emissions (Figure 2.2e). When averaged poleward of 40°N, greater precipitation in the HiVarBB simulations is clear (Figure 2.2f) and statistically significant (Figure 2.A1c). Specifically, total precipitation poleward of 40°N is 0.5% (0.01 mm/day) greater in the HiVarBB simulations relative to the SmoothBB simulations during the GFED period. Greater precipitation is expected with higher surface temperatures that arise from greater net surface shortwave fluxes (e.g., Allen and Ingram, 2002; Andrews et al., 2009).

There is also a discernible northward shift in the Inter-Tropical Convergence Zone (ITCZ) in the HiVarBB simulations relative to the SmoothBB simulations (in agreement with Broccoli et al., 2006, and described further in Section 2.5). This is apparent in Figure 2.2e as a statistically significant northward ITCZ shift over the Atlantic Ocean and drying of the South Pacific Convergence Zone (SPCZ).

Higher surface temperatures in the NH in the HiVarBB simulations relative to SmoothBB simulations also leads to a shift in precipitation phase. In the NH high latitudes, a larger fraction of precipitation falls as rain rather than snow in HiVarBB

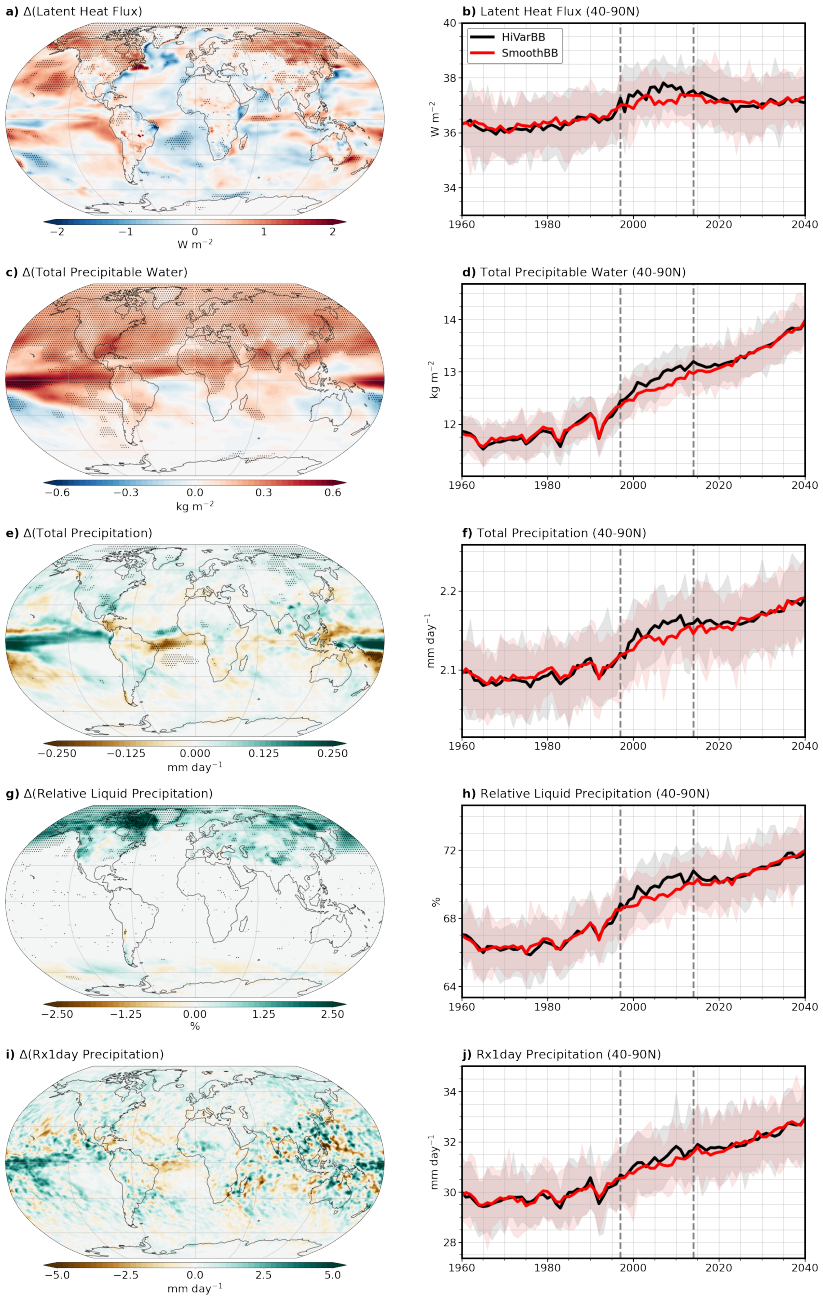

Figure 2.2: **Differences in the atmospheric hydrologic cycle.** (a,b) latent heat flux, in W m^{-2}; (c,d) column-integrated precipitable water, in kg m^{-2}; (e,f) total precipitation, in mm day^{-1}; (g,h) percentage of precipitation that is liquid; and (i,j) annual maximum daily precipitation (Rx1day) in mm day^{-1}. The left column shows the ensemble mean difference (average of HiVarBB ensemble members minus average of SmoothBB ensemble members), with stippling signifying 95% confidence (see Appendix 2.A.1). The right column shows the annual mean value, averaged from 40–90°N, in HiVarBB (black line) and SmoothBB (red line) ensemble members; thick lines denote the ensemble mean, shading denotes the range of each ensemble member set, and vertical gray dashed lines delineate the GFED period (1997–2014).

ensemble members relative to SmoothBB ensemble members (Figure 2.2g). Regional differences in the relative amount of liquid precipitation (proportion of liquid to total precipitation) are statistically significant over much of the NH high latitudes. Averaged poleward of 40°N over the GFED period, the proportion of precipitation that falls as rain is 0.8% larger in the HiVarBB ensemble members relative to the SmoothBB ensemble members (Figure 2.2h) and is statistically significant (Figure 2.A1d). This shift in precipitation phase is present in all seasons, but most apparent during boreal summer (JJA; Figure 2.A2).

We also find the annual maximum daily precipitation is larger in the HiVarBB simulations compared to SmoothBB simulations over the GFED period for most regions poleward of 40°N. Unlike total precipitation, there is no statistical significance in regional differences in annual maximum daily precipitation (Figure 2.2i). However, there is statistical significance in the 40–90°N mean difference during the GFED period. Specifically, the annual maximum daily precipitation is 0.7% (0.2 mm/day) larger in the HiVarBB simulations relative to SmoothBB simulations (Figure 2.2j), and this difference is statistically significant (Figure 2.A1e). Greater intensity of extreme precipitation events in HiVarBB ensemble members compared to SmoothBB ensemble members is generally consistent with greater precipitable water (Allen and Ingram, 2002; Trenberth et al., 2003) and more surface warming (Utsumi et al., 2011).

2.5 Moderating factors to hydrologic cycle amplification

As we have shown, the hydrologic cycle is sensitive to biomass burning emissions variability. However, other compensating ocean and atmospheric processes act to moderate the extent to which increased biomass burning emissions variability amplifies the hydrologic cycle. Most notably, larger ocean heat storage and weaker meridional energy convergence constrain evaporation increases poleward of 40°N. At the same time, changes in atmospheric absorption of shortwave radiation and relative humidity (RH) reduce precipitation efficiency in the HiVarBB simulations, which act to constrain precipitation increases.

First, greater ocean heat storage in HiVarBB simulations moderates hydrologic cycle amplification (Figure 2.3a). Poleward of 40°N, upper ocean heat content (from 0 to 100m depth) is 1.6 ZJ larger in the HiVarBB simulations compared to the SmoothBB

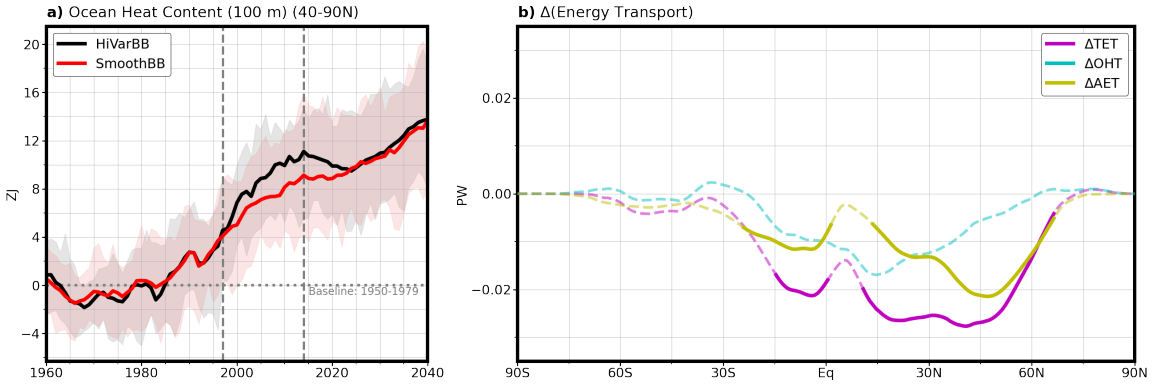

Figure 2.3: **Energetic limitations on hydrologic cycle amplification.** (a) upper (top 100 m) ocean heat content anomalies relative to the 1950–1979 average from 40–90°N in HiVarBB (black line) and SmoothBB (red line) simulations, in ZJ; and (b) ensemble mean difference (average of HiVarBB ensemble members minus average of SmoothBB ensemble members) in the meridional northward energy transport during the GFED period (1997–2014), in PW, including total (ΔTET; black line), atmospheric (ΔAET; yellow line), and ocean (ΔOHT; cyan line) components. In (a), thick lines denote the ensemble mean, while shading denotes the range of each member set. In (b), solid lines signify 95% confidence in the significance of the difference between HiVarBB and SmoothBB ensemble member sets (see Appendix 2.A.1).

simulations during the GFED period, a difference which is statistically significant (Figure 2.A3b). With greater ocean heat storage, not all surplus energy input (from greater surface shortwave radiative fluxes, as shown in Figure 2.1c) immediately goes to increasing evaporative fluxes, thereby moderating their rise. Greater upper ocean heat content in HiVarBB simulations persists for approximately ten years after the end of the GFED period, indicating that ocean heat storage both moderates and lengthens the time scale of the climate response (as described by Barsugli and Battisti, 1998).

Adjustments in meridional energy transport further mitigate hydrologic cycle differences poleward of 40°N between HiVarBB and SmoothBB simulations. Figure 2.3b shows the difference in energy transport between the two simulation ensemble sets, including total, atmospheric, and ocean components. NH total energy transport is lower in HiVarBB simulations relative to SmoothBB simulations (Figure 2.3b, black line) during the GFED period. This lower energy transport is a response to greater energy input poleward of 40°N (Figure 2.1c), which tends to flatten the meridional moist static energy gradient and thereby weaken energy transport (Hwang and Frierson, 2010). Indeed, the total atmospheric energy transport is weaker in HiVarBB simu-

lations compared to SmoothBB simulations (Figure 2.3b, yellow line). This anomalously southward atmospheric energy transport is consistent with a stronger Southern Hemisphere Hadley Cell in HiVarBB simulations (see dry and moist components of atmospheric energy transport in Figure 2.A5) which drives the ITCZ further north (recall Figure 2.2e) and increases net southward atmospheric energy transport in the deep tropics (see Broccoli et al., 2006; Kang et al., 2008). Likewise, lower ocean heat transport also contributes to weaker NH total energy transport (Figure 2.3b, cyan line). Although the lower ocean heat transport is not statistically significant, the weakening of the Atlantic Meridional Ocean Circulation (AMOC) is significant (Figure 2.A6), indicating a decline in ocean heat transport in the Atlantic basin. Weaker meridional energy transport in HiVarBB simulations reduces the energy available for surface warming and evaporation, thereby moderating hydrologic cycle amplification.

Despite greater total precipitation in the HiVarBB simulations, the precipitation efficiency (defined here as the ratio of precipitation to column-integrated precipitable water evaluated locally) is lower in HiVarBB simulations relative to SmoothBB simulations (Figure 2.4a). The average precipitation efficiency poleward of 40°N is 0.9% (1.7×10^{-8} s^{-1}) lower in HiVarBB ensemble members compared to SmoothBB ensemble members, a difference that is statistically significant (Figure 2.A3a). Lower precipitation efficiency means that the atmosphere is less able to precipitate the moisture that is contained within it. Three mechanisms act to lower precipitation efficiency in the HiVarBB simulations relative to the SmoothBB simulations. First, greater atmospheric black carbon aerosol burdens (likely the result of a nonlinear response in atmospheric removal of black carbon) and atmospheric water vapor in the HiVarBB simulations result in greater atmospheric absorption of shortwave radiation (Figures S4a, b, c), which acts to reduce condensation (Mitchell et al., 1987; O'Gorman et al., 2012; Previdi, 2010), and also increases static stability in the lower troposphere (by increasing moist potential temperature between 990 and 950 hPa; see Figure 2.4b). Greater static stability in HiVarBB simulations acts to suppress vertical motion and cloud formation relative to the SmoothBB simulations (consistent with O'Gorman and Schneider, 2009; Richter and Xie, 2008). Second, greater upper tropospheric water vapor (see Figure 2.A4b) decreases atmospheric radiative cooling (Allen and Ingram, 2002; Previdi, 2010). Third, because lower tropospheric RH is lower poleward of 40°N in the HiVarBB simulations (Figure 2.4c), more energy is required to raise air parcels to their lifting condensation level relative to the SmoothBB simulations. Additionally, air parcels are less likely to be lifted to levels where they can saturate,

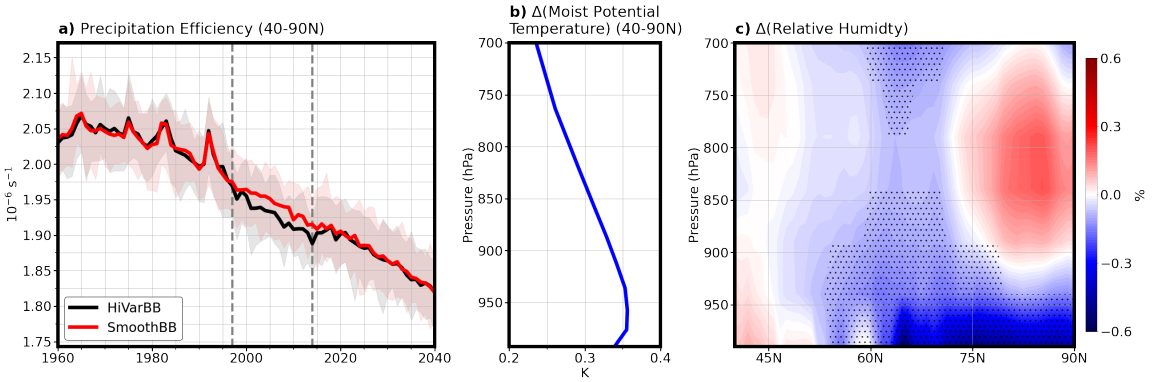

Figure 2.4: **Precipitation efficiency and factors that impact it.** (a) total precipitation efficiency, in 10^{-6} s^{-1}, in HiVarBB (black line) and SmoothBB (red line) simulations, with the vertical gray dashed lines delineating the GFED period (1997–2014); (b) ensemble mean difference in the mean 40–90°N vertical moist potential temperature profile, in K; and (c) ensemble mean difference in zonal mean relative humidity from 40–90°N, in %. In (a), thick lines denote the ensemble mean, while the shaded regions denote the range of each ensemble member set. In (b) and (c), the ensemble mean differences are computed as the average of HiVarBB ensemble members minus the average of SmoothBB ensemble members during the GFED period (1997–2014). In (b), the solid line signifies 95% confidence in the significance of the difference between ensemble member sets (see Appendix 2.A.1). In (c), stippling signifies 95% confidence in the significance of the difference between ensemble member sets (see Appendix 2.A.1).

as the atmosphere is more statically stable in the HiVarBB simulations (Wallace and Hobbs, 2006). This lower RH is likely caused by water limitations over land, where the largest differences in surface shortwave absorption and surface temperature occur (Figure 2.1c, d; O'Gorman and Muller, 2010).

2.6 Implications

Our results provide clear evidence that variability in biomass burning emissions affect the hydrologic cycle. We show that greater biomass burning emissions variability, as used in CMIP6 historical simulations during the GFED period (1997–2014), amplifies the hydrologic cycle in CESM2. Evaporation, atmospheric precipitable water, mean precipitation, precipitation extremes, and fraction of rain precipitation all increase with greater biomass burning emissions variability. This amplification is consistent with the thermodynamic impact of warming (e.g., Allan et al., 2022; Held and Soden,

2006; Stott et al., 2010). Conversely, this hydrologic cycle amplification is moderated by several competing factors: greater ocean heat storage moderates the available energy for evaporation over ocean; weaker meridional energy transport decreases the energy available for surface warming; and greater atmospheric radiative absorption and lower RH in HiVarBB ensemble members leads to lower precipitation efficiency poleward of 40°N.

It is possible these findings extend to other models participating in CMIP6, not just CESM2. All CMIP6 historical simulations use the same biomass burning emissions, including the increase in variability during the GFED period. Indeed, Fasullo et al. (2022) and DeRepentigny et al. (2022) find evidence of characteristic increases in downwelling shortwave radiation and Arctic sea ice loss, respectively, during the GFED period in several other CMIP6 models. This suggests that other models may also be sensitive to greater biomass burning emissions variability. Further care is required for future treatments of biomass burning emissions variability in historical simulations. If the biomass burning emissions variability over the entire historical and future projection periods was corrected to be more continuous (whether to align with the variability of the GFED estimates, or the estimates prior), the hydrologic cycle would likely change. We note, however, that although each model is subject to the same increase in variability, this does not mean that every model is sensitive to this change (DeRepentigny et al., 2022; Fasullo et al., 2022). We also note that differing model sensitivities to this variability may increase the inter-model spread, and therefore uncertainty, over the GFED period. This highlights the need for further study into how greater biomass burning variability during the GFED period affects hydrologic cycle in a range of CMIP6 models. To assess whether the results presented here from CESM2 are robust, it would be appropriate to run similar modelling experiments using other CMIP6 Earth system models.

As indicated by these findings, care is required when analyzing hydrologic cycle fields within CMIP6 and CESM2-LE historical simulations. Precipitation robustly increases in most areas poleward of 40°N in CMIP6 future projections (Cook et al., 2020). If a baseline includes the GFED period (1997–2014), precipitation increases over future time periods are likely to be computed as lower than if adjacent baseline periods are used. For example, the change in mean precipitation poleward of 40°N from 1995–2015 to 2080–2100 is approximately 7% smaller in the HiVarBB simulations than the SmoothBB simulations. Furthermore, the difference in precipitation between HiVarBB and SmoothBB simulations during the GFED period represents 6% of the

total mean precipitation signal between 1950–1980 to 2070–2100 in CESM2. Similar issues are likely even worse for other hydrologic cycle variables, such as atmospheric water vapor, as the relative difference between HiVarBB and SmoothBB simulations is even larger. As such, this study highlights a previously unknown source of uncertainty in hydrologic cycle projections.

Our findings demonstrate that the interannual variability of biomass burning emissions may be an important factor that determines the strength of the atmospheric hydrologic cycle. More research is required to better understand the mechanisms driving the climate response to biomass burning emissions variability, particularly that of aerosols and aerosol-adjacent compounds. We underscore the need for studies using multiple models to better parse out the underlying mechanisms by which biomass burning emissions variability impacts the hydrologic cycle and the greater climate system.

2.A Appendix to Chapter 2

Here, we present the methods we used to evaluate statistical significance (Appendices 2.A.1 and 2.A.2), as well as supplemental figures that further our findings on differences between CMIP6 (HiVarBB) and smoothed (SmoothBB) biomass burning emission scenarios in the CESM2 Large Ensemble. These figures show: statistical significance of area-averaged differences of metrics shown in Figure 2.2 (Figure 2.A1), seasonal differences in relative liquid precipitation (Figure 2.A2), statistical significance of differences in precipitation efficiency and ocean heat content (Figure 2.A3), differences in atmospheric and cloud properties (Figure 2.A4), differences in the moist and dry atmospheric energy transport components (Figure 2.A5), and differences in the Atlantic meridional overturning circulation (AMOC; Figure 2.A6).

2.A.1 Evaluating spatial statistical significance

We assess spatial (i.e., grid point, zonally-averaged, and vertical profile) statistical significance using a Welch's t-test. We additionally limit significance determinations for false discoveries using the recommendations made by Wilks (2016), given that many statistical significance tests are performed simultaneously. We use an α_{FDR} of 0.10 to approximate a global significance level of 0.05.

2.A.2 Evaluating area-averaged statistical significance

We use a non-parametric bootstrapping approach to determine the statistical significance of the area-average differences between fields in HiVarBB and SmoothBB ensemble member sets. We conduct this test by randomly dividing all 80 members into two groups and determining the difference in the means of each group. We repeat this random selection a hundred thousand times to develop a distribution of random differences. We determine significance if the mean difference between the HiVarBB and SmoothBB ensemble member sets is outside of the 2.5 and 97.5 percentile range, signifying the two-tail 95% confidence interval of the distribution of differences between randomly divided members. This test allows us to determine whether, with 95% confidence, the mean difference between the HiVarBB and SmoothBB ensemble member sets is greater than what could be generated by chance if the mean difference was only influenced by internal variability. To verify that significant differences are unique to the GFED period, we also conduct sensitivity tests by running the test over multiple time periods, both before and after the GFED period.

2.A.3 Supplementary figures

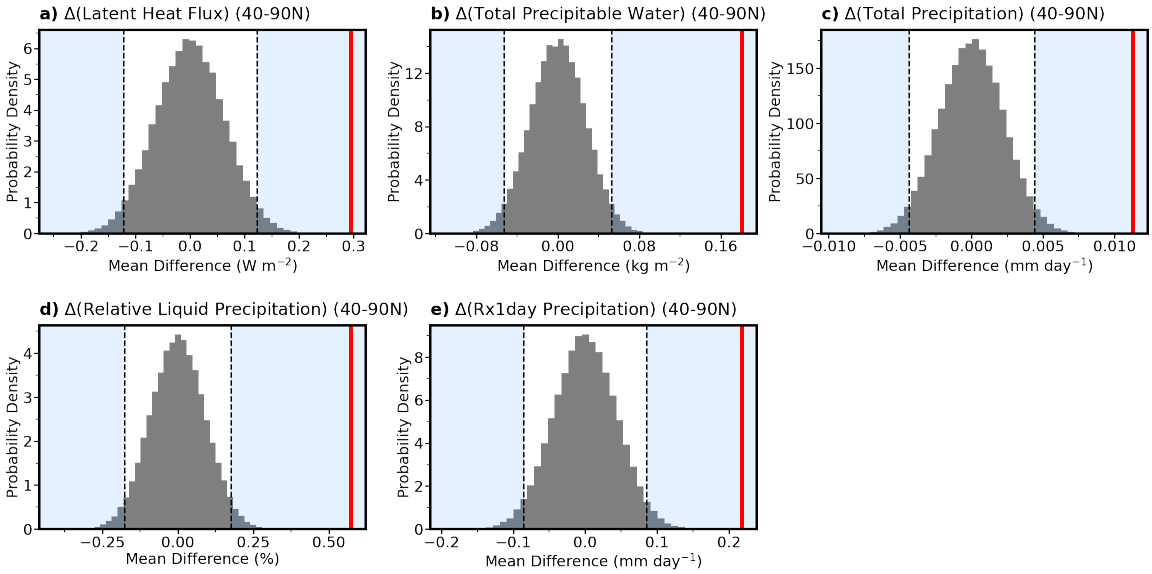

Figure 2.A1: **Statistical significance of area-averaged differences in the atmospheric hydrologic cycle.** (a) latent heat flux, in W m^{-2}; (b) column-integrated precipitable water, in kg m^{-2}; (c) total precipitation, in mm day^{-1}; (d) percentage of precipitation that is liquid; and (e) annual maximum daily precipitation (Rx1day) in mm day^{-1}, all from 40-90°N over the GFED period (1997–2014). The gray histogram shows a probability density distribution of means derived from a non-parametric bootstrapping test (see Appendix 2.A.2), and the blue shading indicates the region outside of the (two-sided) 95% confidence intervals; the difference between HiVarBB and SmoothBB ensemble means (red line) is statistically significant (at the 95% level) if it falls within the blue shaded region.

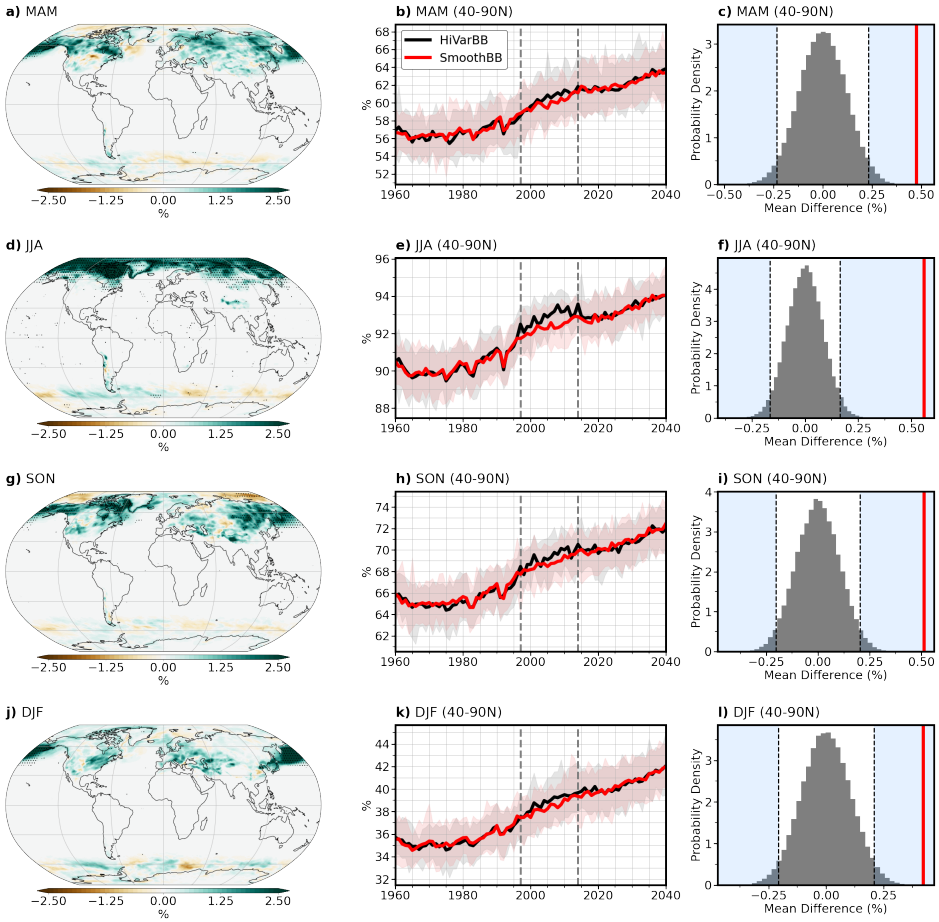

Figure 2.A2: **Differences in seasonal relative liquid precipitation.** The left and middle columns are the same as in Figure 2.2, but showing differences in percentage of precipitation that is liquid in (a-c) March-May (MAM), (d-f) June-August (JJA), (g-i) September-November (SON), (j-l) and December-February (DJF). The right column shows the statistical significance of the difference in HiVarBB and SmoothBB ensemble means from 40-90°N over the GFED period. The gray histogram shows a probability density distribution of means derived from a non-parametric bootstrapping test (see Appendix 2.A.2), and the blue shading indicates the region outside of the (two-sided) 95% confidence intervals. The difference between HiVarBB and SmoothBB ensemble means (red line) is statistically significant (at the 95% level) if it falls within the blue shaded region.

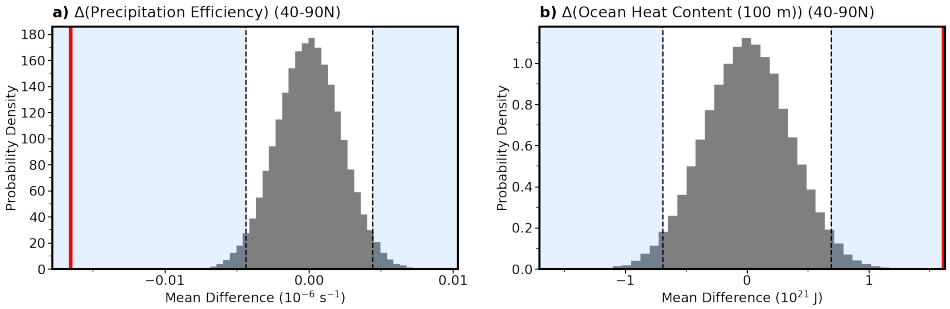

Figure 2.A3: **Statistical significance of area-averaged differences in moderating factors.** (a) precipitation efficiency, and (b) upper (top 100 m) ocean heat content from 40-90°N during the GFED period (1997–2014). The gray histogram shows a probability density distribution of means derived from a non-parametric bootstrapping test (see Appendix 2.A.2), and the blue shading indicates the region outside of the (two-sided) 95% confidence intervals. The difference between HiVarBB and SmoothBB ensemble means (red line) is statistically significant (at the 95% level) if it falls within the blue shaded region.

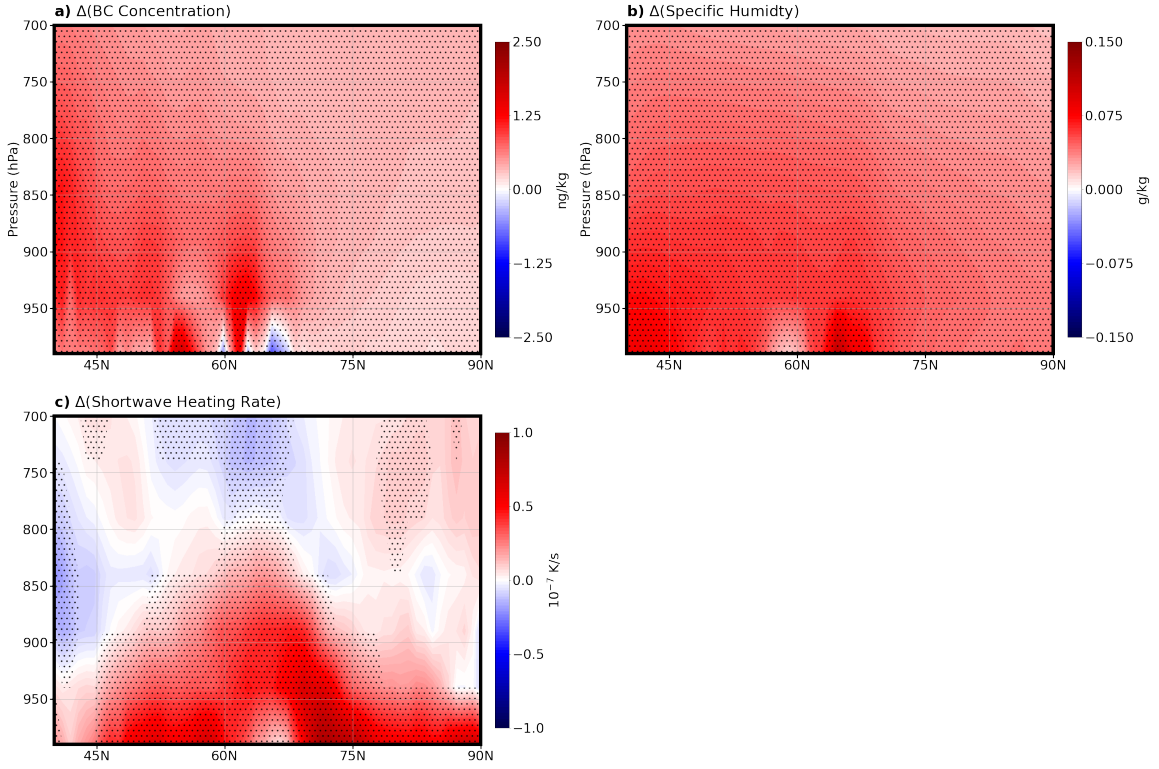

Figure 2.A4: **Zonal-mean ensemble mean difference of mechanisms affecting the precipitation efficiency.** (a) black carbon concentration (in ng/kg), (b) specific humidity (in g/kg), (c) shortwave heating rate (in 10^{-7} K/s) from 40-90°N. Ensemble mean differences are computed as as the average of HiVarBB ensemble members minus the average of SmoothBB ensemble members during the GFED period (1997–2014). Stippling signifies 95% confidence in the significance of the difference between ensemble member sets (see Appendix 2.A.1).

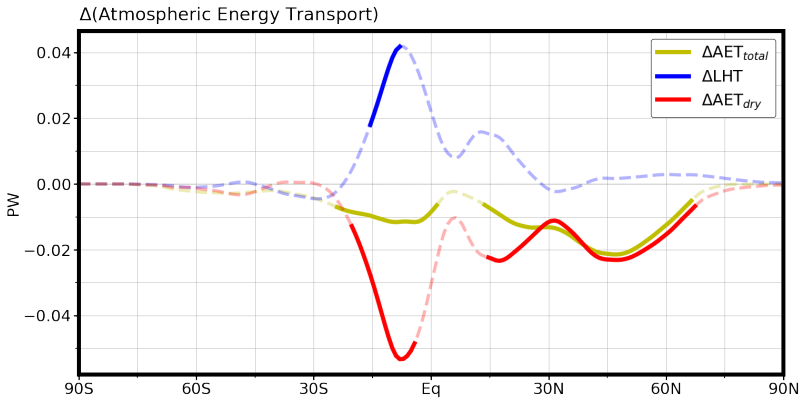

Figure 2.A5: **Differences in meridional atmospheric energy transport components.** Ensemble mean difference (average of HiVarBB ensemble members minus average of SmoothBB ensemble members) in the total atmospheric energy transport (ΔAET_{total}, yellow line), latent heat transport (ΔLHT, blue line), and dry static energy transport (ΔAET_{dry}, red line) during the GFED period (1997–2014), in PW. Solid lines signify 95% confidence in the significance of the difference between HiVarBB and SmoothBB ensemble member sets (see Appendix 2.A.1).

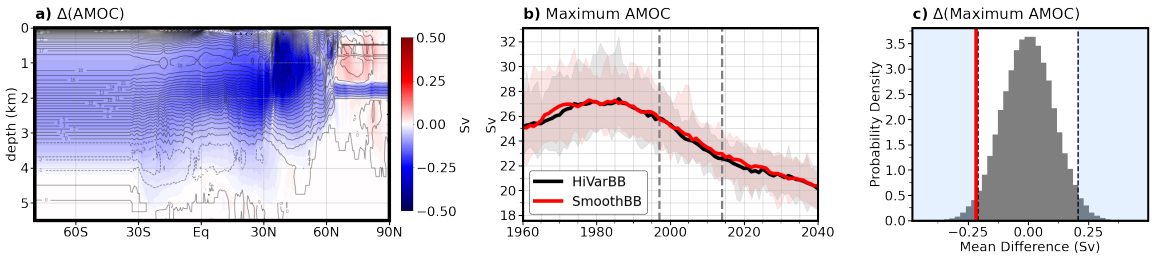

Figure 2.A6: **Differences in Atlantic meridional overturning circulation (AMOC).** (a) zonal-mean ensemble mean difference (average of HiVarBB ensemble members minus average of the SmoothBB ensemble members), (b) annual mean Atlantic meridional overturning maximum from HiVarBB (black curve) and SmoothBB (red curve) ensemble members; thick lines denote the ensemble mean, shading denotes one standard deviation of each ensemble member set, and horizontal gray dotted lines delineate the GFED period (1997–2014), and (c) statistical significance of the difference in Atlantic meridional overturning maximum ensemble means during the GFED period. The gray histogram shows a probability density distribution of means derived from a non-parametric bootstrapping test (see Appendix 2.A.2), and the blue shading indicates the region outside of the (two-sided) 95% confidence intervals. The difference between HiVarBB and SmoothBB ensemble means (red line) is statistically significant (at the 95% level) if it falls within the blue shaded region.

Chapter 3

Why aerosol emissions variability leads to large-scale surface warming

The aerosol forcing magnitude remains among the largest unknowns when assessing climate sensitivity over the historical period. Here, we quantify and explain a crucial but often overlooked source of uncertainty in aerosol forcing: the temporal variability of aerosol emissions. We show that time-variability in biomass burning (BB) emissions weakens the time-averaged total aerosol forcing, particularly in the Northern Hemisphere mid- to high-latitudes. BB emissions variability produces weaker (less negative) mean effective radiative forcing (ERF) compared to scenarios with no interannual variability in emissions. Satellite-estimated BB emissions (and associated variability) result in a June–September absolute ERF (relative to zero BB emissions) of -7.7 W m^{-2} from 50–70°N, compared to -10.4 W m^{-2} when no emissions variability is used in the Community Earth System Model version 2 (CESM2). This difference in forcing is attributable to nonlinear aerosol-cloud interactions. Aerosol forcing will be overestimated (i.e. more negative) if emissions are temporally-smoothed.

The contents of this chapter were published in Geophysical Research Letters as *Variability in Biomass Burning Emissions Weakens Aerosol Forcing due to Nonlinear Aerosol-Cloud Interactions* (Heyblom et al., 2023).

3.1 Introduction

Atmospheric aerosols are a critical component of the climate system, but the complex processes governing their production, deposition, and interactions with clouds are difficult to observe and model. Uncertainty in the aerosol forcing is one of the greatest challenges for understanding historical climate change and projecting near-future climate evolution (Kiehl, 2007; Forster et al., 2021).

Previous research on aerosol radiative forcing has focused on the effect of secular change in aerosol emissions, with little consideration of the impact of shorter timescale variability in the emissions. For example, the fifth Coupled Model Intercomparison Project (CMIP5; Taylor et al., 2012) historical and future simulations use biomass burning (BB) emissions estimates that are smooth temporally compared to real-world emissions, particularly on inter- and sub-annual time scales. Real-world BB emissions in the extratropics occur episodically and stochastically, and may depend on weather conditions (precipitation, drought, lightning) or human activity (agricultural burning, forest clearing, arson) (Lamarque et al., 2010; van der Werf et al., 2017).

To incorporate more realistic aerosol emissions variability, the latest CMIP (sixth phase; CMIP6; Eyring et al., 2016) includes BB emissions estimates derived from satellite observations for historical simulations from 1997 to 2014 (Figure 3.1a; van Marle et al., 2017). Historical CMIP6 BB emissions in this time period have much higher temporal variability than those used in previous model intercomparison efforts (e.g., the CMIP5 historical simulations). However, the BB emissions used for CMIP6 prior to 1997 (before satellite measurement capability) are similar to the CMIP5 inventories, with weak temporal variability (Figure 3.1a black line; Lamarque et al., 2010; van Marle et al., 2017).

Recent analyses in the Community Earth System Model version 2 (Danabasoglu et al., 2020, CESM2;) have estimated the climate effect of this change in BB emissions variability by comparing simulation scenarios with temporally-smoothed BB emissions to scenarios with time-varying CMIP6 emissions over the 1997 to 2014 period (DeRepentigny et al., 2022; Fasullo et al., 2022; Heyblom et al., 2022; Rodgers et al., 2021). The largest set of these comparison simulations is the CESM2 Large Ensemble (CESM2-LE; Figure 3.1a Rodgers et al., 2021). Studies using the CESM2-LE show that the sudden change in BB emissions variability in the CMIP6 late-historical simulations leads to shifts in the climate, producing increases in simulated downwelling shortwave radiation and enhancing surface warming (Fasullo et al., 2022, also

Figure 3.1b), increases in atmospheric water vapor and precipitation (Heyblom et al., 2022), and accelerated Arctic sea ice loss (DeRepentigny et al., 2022). These studies postulated that nonlinearities in the climate system's response to BB aerosols produced these climate effects. However, the coupled climate model simulations used in these studies did not allow for the decoupling of climate forcing and feedback, making attribution of the cause difficult.

Here, we use idealized Earth System Model (ESM) simulations to show that the temporal variability of BB aerosol emissions substantially impacts the magnitude of the forcing attributable to these emissions. We show that BB emissions variability impacts BB aerosol forcing because of a nonlinear response of aerosol-cloud interactions to atmospheric aerosol concentrations. Our study provides direct evidence that temporal variability of BB aerosol weakens the time-averaged aerosol cloud radiative effect in a state-of-the-art ESM, and that temporal smoothing will lead to a much stronger BB aerosol radiative effect.

3.2 Methods

To quantify the impact that greater interannual variability in biomass burning (BB) emissions has on the total radiative forcing attributable to these emissions, we conduct simulations using the Community Earth System Model version 2 (Danabasoglu et al., 2020, CESM2;) with idealized BB emissions perturbations. In each simulation we configure CESM2 in the same way as the CESM2-LE (Appendix 3.A.1), but fix sea surface temperatures (SSTs), sea ice concentrations, and all forcings (except BB emissions) to the 2000 climatology (mean monthly values from 1995 to 2005). We use three different simulations, each of which treat BB emissions variability differently (Figure 3.2). Each simulation is run for 54 years.

The first simulation (hereafter "Real-Var"; Figure 3.2 green line) uses BB emissions as prescribed for CMIP6 historical simulations from 1997 to 2014 (van der Werf et al., 2017; van Marle et al., 2017). The emissions estimates for this period are thus taken to represent a best estimate of real-world BB emissions. These 18 years of emissions are repeated three times. The second simulation (hereafter "Pulse-Var"; Figure 3.2 yellow line) prescribes an idealized high-temporal variability emissions scenario where all emissions for each grid cell occur every six years in phase with all other grid cells. Total emissions in years that simulate a pulse of BB emissions are equal to six times the annual mean emissions from the Real-Var experiment at each grid cell;

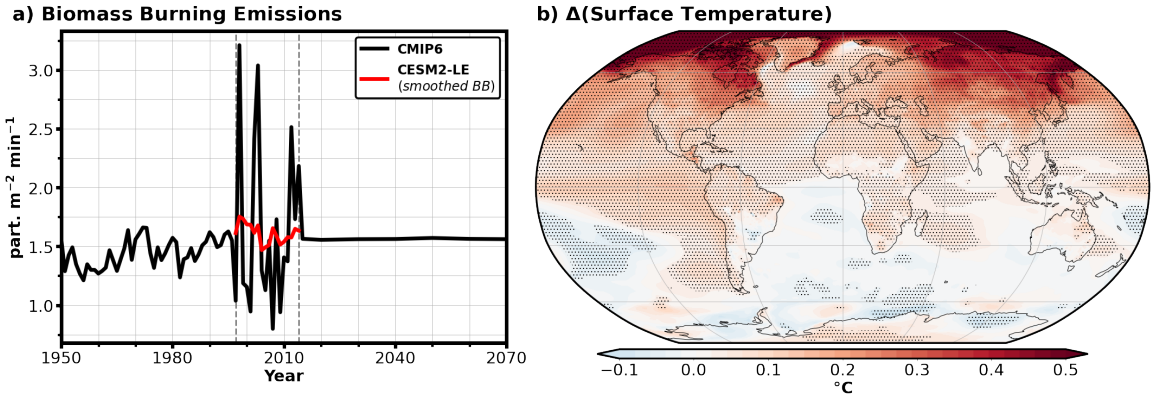

Figure 3.1: **Biomass burning (BB) emissions used for CMIP6 and the effect of high BB emissions variability on surface temperature in CESM2.** Panel (a) shows the annual mean biomass burning (BB) emissions averaged over 50–70°N prescribed for CMIP6 (black line) and a second smoothed emissions inventory used for 50 members of the Community Earth System Model Large Ensemble version 2 (CESM2-LE) over the recent historical period (red line), in particles m^{-2} min^{-1} (Appendix 3.A.1). The vertical grey dashed lines delineate the period of high BB emissions variability in the CMIP6 prescribed BB emissions (1997–2014). Panel (b) shows the difference in surface temperature between the CMIP6 emissions ensemble members and smoothed BB emissions ensemble members in the CESM2-LE during 1997–2014 (average of 50 CMIP6 emissions ensemble members minus average of 50 smoothed BB emissions ensemble members; in °C). Stippling signifies 90% confidence (Appendix 3.A.8). See Appendix 3.A.1 for a further description of CESM2-LE and BB emissions therein.

during other years BB emissions are zero. A third experiment (hereafter "Zero-Var"; Figure 3.2 black line) uses emissions based upon a climatology that repeats each year, and thus has no interannual variability in BB emissions. It is important to note that due to the aggregation of emissions in time, the Pulse- and Zero-Var inventories are also spatially smoother than the Real-Var inventory.

All simulations use fixed SSTs to allow the direct quantification of the effective radiative forcing (ERF) in the absence of most feedbacks (Hansen et al., 2005; Forster et al., 2021, Appendix 3.A.3;). Because the time-integrated emissions are equal across these three simulations, differences in ERF are attributable entirely to differences in the variability of BB emissions.

In addition, we utilize the outcomes obtained from our fixed-SST simulations to create a heuristic model that illustrates the underlying mechanism responsible for the differences in ERF when variations in BB emissions variability are specified. To achieve this, we derive synthetic distributions that represent the aerosol concentrations present in the Zero-Var (black) and Real-Var (green) simulations by fitting normal and log-normal probability density functions to the Zero-Var and Real-Var simulation concentrations, respectively. We then demonstrate how each of these idealized aerosol concentration distributions leads to different distributions of cloud radiative effect (CRE).

3.3 Results

3.3.1 The effects of emissions variability on the aerosol forcing

Figure 3.3a–c shows that the BB aerosol effective radiative forcing (ERF) weakens (i.e., becomes less negative) when emissions vary in time (as in Real-Var and Pulse-Var) compared to when there is no interannual variability (as in Zero-Var). We denote the change in ERF due to BB emissions variability as $\Delta\mathrm{ERF}_{\mathrm{BBVar}}$, computed as the difference in the ERF between scenarios with time-varying emissions (Pulse-Var and Real-Var) and Zero-Var. The $\Delta\mathrm{ERF}_{\mathrm{BBVar}}$ is strongest over regions of high column-integrated aerosol concentration variability (Figure 3.A1), particularly over the NH mid- to high-latitudes from June–September (JJAS; the period of most active fires in this region; see Figure 3.A2 for annual mean difference). For example, averaged from 50–70°N, we find a +1.1 W m^{-2} (+0.1 W m^{-2} global) annual mean and +2.7

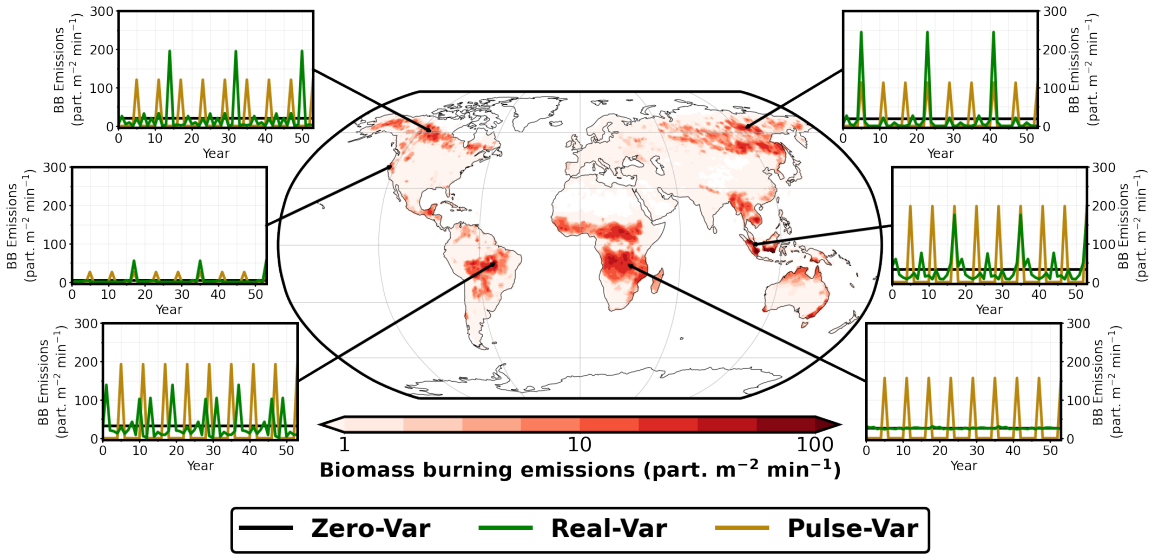

Figure 3.2: **Idealized simulations to quantify changes in effective radiative forcing (ERF) due to biomass burning (BB) emissions variability.** The center image shows the time-integrated emissions rate of BB emissions for all scenarios (in particles m^{-2} min^{-1}; Appendix 3.A.2) in red, while the surrounding insets show the time evolution of BB emissions from Zero-Var, Real-Var, and Pulse-Var (black, green, and brown lines, respectively) at selected locations.

W m^{-2} (+0.42 W m^{-2} global) JJAS mean ERF weakening in the Real-Var experiment relative to Zero-Var. Interestingly, a region of strong ΔERF_{BBVar} is apparent in the eastern tropical Atlantic in the Pulse-Var simulation, but not the Real-Var simulation. We suggest that this discrepancy is the result of unrealistic interannual biomass burning emissions variability imposed over central Africa (where emissions interannual variability is typically quite low; see corresponding Figure 3.2 inset). In effect, episodic BB emissions leads to a weaker (i.e., less negative) aerosol forcing associated with biomass burning.

3.3.2 Differences in forcing are driven by differences in the cloud radiative effect

ERF sensitivity to emissions variability (i.e., ΔERF_{BBVar}) is due to a weaker time-averaged cloud response to aerosol emissions when BB emissions are variable. Figure 3.3d–g shows how time-averaged cloud properties are affected by BB emissions variability. Each panel displays selected JJAS cloud property changes for the higher variability simulation compared to the Zero-Var simulation (Real-Var and Pulse-Var simulations in the left and right column respectively; also see Figure 3.A3 for annual mean change). Averaged cloud droplet number concentration (CDNC; Figure 3.3d,e) is smaller in the simulations with higher interannual BB variability. Similar to ERF changes, the largest sensitivity in CDNC is found in regions where BB emissions interannual variability is large (i.e. predominately over the NH mid- to high-latitudes land regions). There are similar reductions in cloud amount and liquid water path with increased BB emissions variability (Figure 3.A4).

The time-averaged increase in absorbed radiation due to changes in clouds is shown in Figure 3.3f,g as the cloud radiative effect (CRE). The CRE change due to BB emissions variability is highly correlated with ΔERF_{BBVar}: global Pearson pattern correlation coefficient of the annual means of 0.87 in the Real-Var experiment and 0.93 in the Pulse-Var experiment. These correlations, and the similar magnitudes of CRE and ΔERF_{BBVar}, indicate that ΔERF_{BBVar} is driven by changes in time-averaged cloud properties when BB emissions are variable.

We note that there is a small region over Arctic land where there is increased absorbed radiation that is not due to changes in clouds (Figure 3.A5a,b; shown as clear-sky top of atmosphere net radiative flux). The increase in absorbed radiation in the absence of clouds is due to a decrease in land-surface albedo over the same region

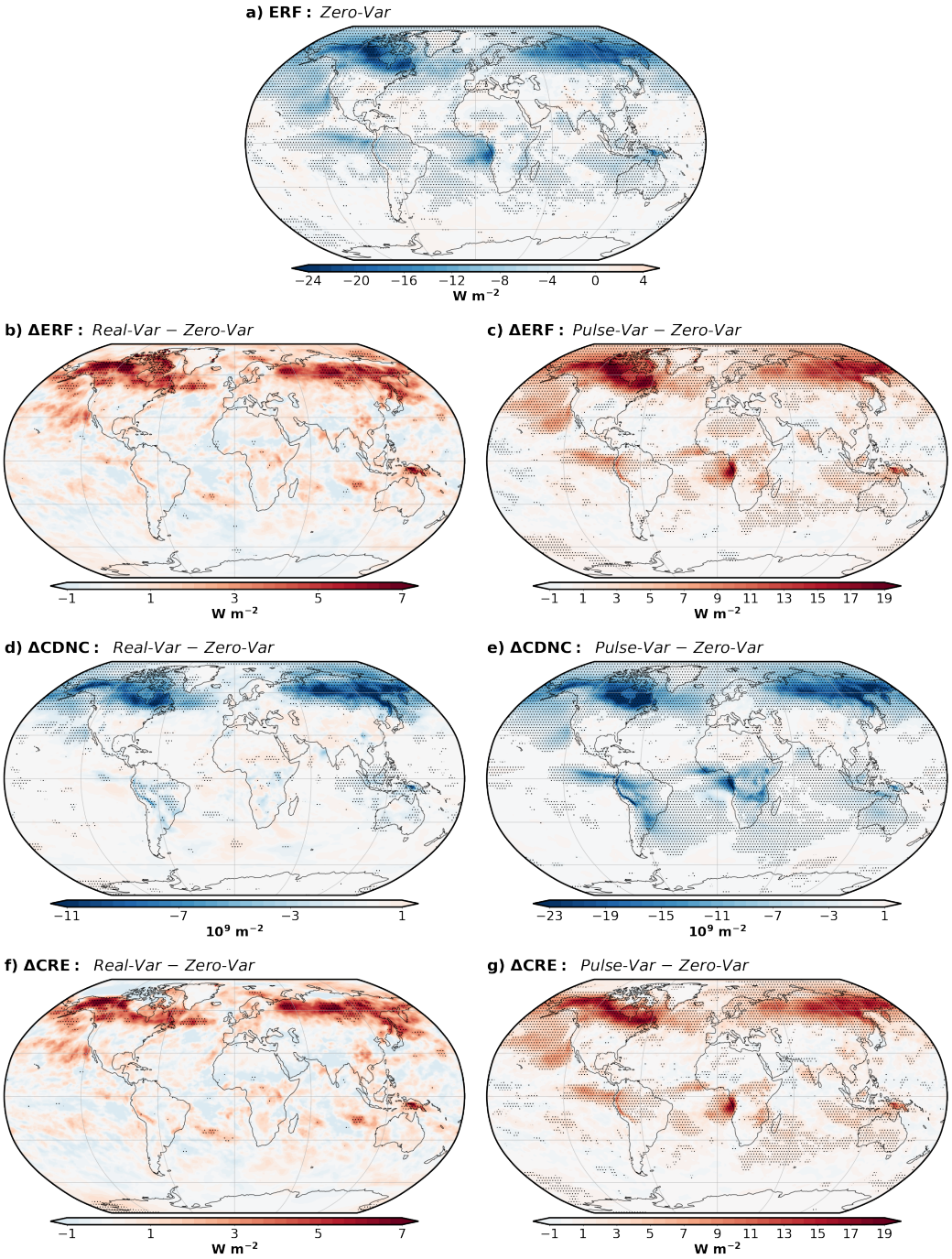

Figure 3.3: **Change in effective radiative forcing (ERF) and cloud properties due to biomass burning emissions variability.** Panel (a) shows the June–September (JJAS) mean absolute ERF due to BB emissions in the Zero-Var experiment (relative to no BB emissions). Panels (b)–(g) show the JJAS mean change in ERF (b and c; denoted $\Delta\text{ERF}_{\text{BBVar}}$; in W m^{-2}), vertically integrated cloud droplet number concentration (d and e; CDNC; in 10^9 m^{-2}), and total (long and shortwave) cloud radiative effect (f and g; CRE; in W m^{-2}) due to BB emissions variability in the Real-Var (left column) and Pulse-Var (right column) experiments. Changes due to BB emissions variability are defined as the variability experiments minus the Zero-Var experiment. Stippling signifies 90% confidence (Appendix 3.A.8).

(Figure 3.A5c,d), which is a feedback resulting from the difference in forcing. Though the configuration and method used here to quantify the ERF is a widely accepted approach (Appendix 3.A.3; also see Hansen et al., 2005; Smith et al., 2020; Forster et al., 2021), it does allow for the possibility that computed changes in ERF are due differences in land-surface feedbacks not corrected for in our computation (Appendix 3.A.3). We replicated the Real-Var experiment in an aquaplanet configuration with CESM2 (in which land surfaces are replaced with an idealized ocean; Appendix 3.A.4; Marshall et al., 2007) and find qualitatively similar results (Figure 3.A5). From this, we conclude the cloud response to BB emissions variability is not driven by land surface interactions. Though nonlinear land feedbacks, such as the land surface albedo, may be amplifying the change in ERF (as computed in this study) due to differences in BB emissions variability, they are not the driver of the model response.

3.3.3 Differences in cloud radiative effect are due to nonlinear aerosol-cloud interactions

We now show that the time-averaged CRE weakens when BB emissions are more variable because of a nonlinear relationship between atmospheric aerosol concentrations and their effects on cloud properties. Nonlinearity in aerosol-cloud interactions are expected from both modelling and observational studies. As aerosol concentrations increase, they less effectively nucleate to become cloud droplets (Twomey, 1977; Rissman et al., 2004; Reutter et al., 2009; Carslaw et al., 2013; Bougiatioti et al., 2016; Kacarab et al., 2020). Because cloud droplet nucleation becomes less effective at higher aerosol concentrations, the relationship between aerosol concentration and CRE is nonlinear.

Figure 3.4 confirms that the time- and area-averaged relationship of CDNC and CRE is indeed nonlinear over 50–70°N during JJAS. Shown in this figure are the cloud responses to varying fixed BB emissions rates (purple), as well as Real-Var (green) and Pulse-Var (yellow) simulations. Figure 3.4 also shows responses to varying aerosol concentrations in the CESM2-LE during the simulated high BB emissions variability period from 1997 to 2014 (blue; shown as probability density function). From the left column of Figure 3.4, it is clear that CDNC and CRE depend nonlinearly on aerosol concentration. This nonlinear response is apparent across the fixed aerosol emissions simulations, as well as in the Real-Var experiment and CESM2-LE.

The nonlinear response to BB emissions influences the temporal evolution of the

simulations, seen in the right column of Figure 3.4. When emissions are higher than the Zero-Var case, the incremental change in CDNC and CRE is smaller in magnitude than when emissions are lower than the Zero-Var case. As a result, over low emissions years, there is a larger increase in absorbed solar energy (relative to the Zero-Var baseline) compared to the decrease in absorbed solar energy over high emissions years, explaining the time-averaged effects seen in Figure 3.3.

We use a heuristic model to further demonstrate how nonlinearities in aerosol-cloud interactions lead to a weakening of the time-averaged CRE if aerosol emissions are variable in time. Figure 3.5a shows distributions representative of the 50–70°N area mean aerosol concentration resulting from emissions in the Zero-Var (normal distribution; black) and Real-Var (log-normal distribution; green) experiments, both of which have the same mean (overlapping vertical green and black lines). Note that the Zero-Var distribution has some variability (i.e., width) because of meteorological variability within these simulations, not BB emissions variability itself, which is nil. Figure 3.5b shows nonlinear (logarithmic; solid) and linear (dashed) functions describing two separate inferred relationships between aerosol concentrations and CRE, derived from Figure 3.4b (see Appendix 3.A.5 for further description).

Figure 3.5c shows the projected distributions of CRE using the functions shown in Figure 3.5b. Comparing CRE distributions resulting from nonlinear (solid lines) and linear (dashed lines) aerosol-CRE functions shows the effect of nonlinearity in the aerosol-CRE relationship (Figure 3.5c). First, any aerosol distribution will be skewed towards weakened CRE values as the nonlinear aerosol-CRE function deviates further from the linear function at lower aerosol concentrations than at higher concentrations. Second, realistic emissions variability (such as in Real-Var) has a much higher frequency of low concentration years (where the nonlinear relationship deviates the most from the linear function) compared to high concentration years, resulting in further CRE weakening. The combination of these two effects results in a weaker mean CRE for the log-normal aerosol concentration distribution when using the nonlinear aerosol-CRE function (horizontal solid green line) compared to the linear aerosol-CRE function (horizontal dashed green and black lines). We note that the mean CRE is also weaker for the normal aerosol concentration distribution when using the nonlinear aerosol-CRE function (horizontal solid black line) compared to if the linear aerosol-CRE function is used, though the change is small (and not visible on Figure 3.5c) as the variability is low.

Two synthetic time series of aerosol concentrations (Figure 3.5d) and the resulting

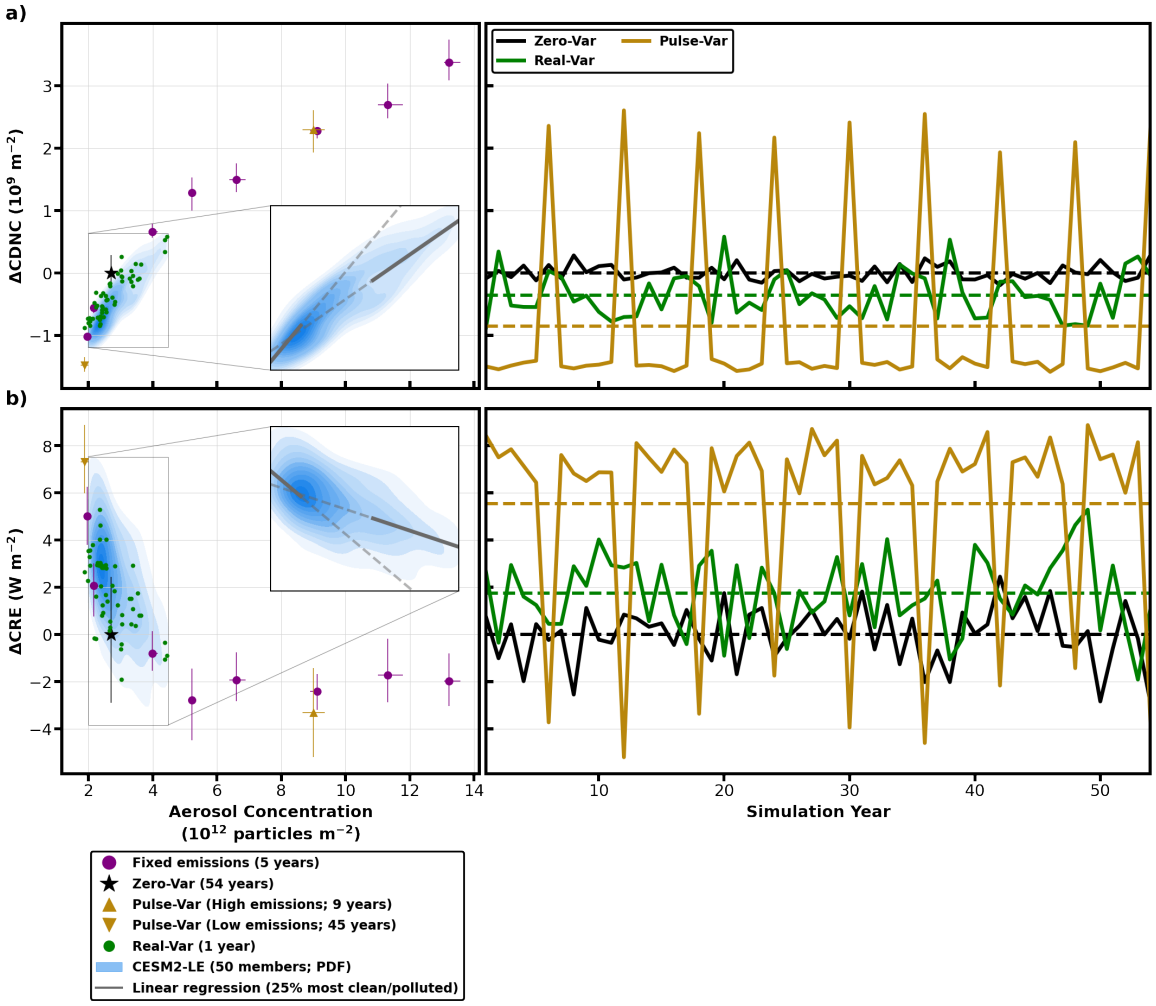

Figure 3.4: **Responses of CDNC and CRE to varying aerosol emissions** for June–September (JJAS) averaged over 50–70°N, relative to the Zero-Var simulations unless otherwise stated. The left column shows the relationship between column-integrated aerosol concentrations (in W m^{-2}; Appendix 3.A.2) and (a) column-integrated CDNC (in 10^9 m^{-2}) or (b) CRE (in W m^{-2}) for a collection of years (number of years displayed in the legend) drawn from each experiment. The average and range of that collection is shown by marker and whiskers. The "High" and "Low" statistics are produced by averaging the years which do and do not have BB emissions in the Pulse-Var experiment, respectively. "Fixed emissions" experiments are run under the same conditions as the Zero-Var experiments, however, use varying scaled BB emissions. CESM2-LE probability density functions (PDF) represent changes of each year in the high BB emissions variability simulations relative to the ensemble annual mean from the low BB emissions variability simulations of the CESM2-LE historical simulations from 1997 to 2014 (see Appendix 3.A.1 for a description of different CESM2-LE ensemble members). The right column shows the time evolution of the of CDNC and CRE from the Zero-Var, Real-Var, and Pulse-Var simulations. The horizontal dashed line represents the JJAS mean for the entire simulation period.

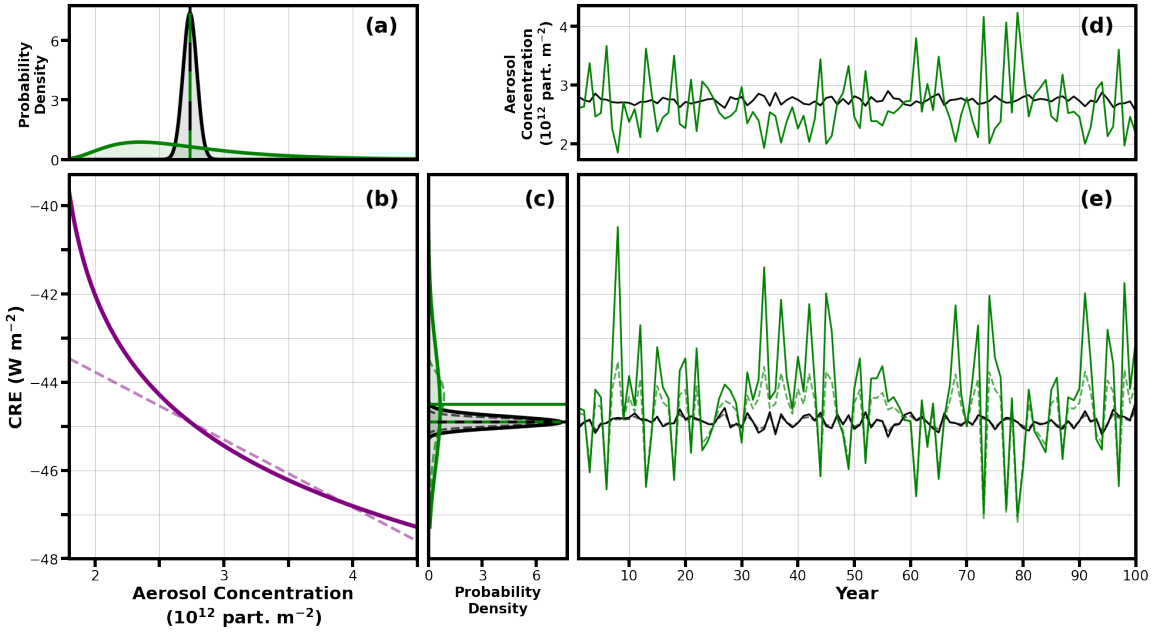

Figure 3.5: **Idealized cloud radiative effect (CRE) response to varying aerosol concentrations.** Panel (a) shows probability density functions (PDF) of aerosol concentrations representative of Real-Var and Zero-Var BB emissions scenarios (green and black, respectively). Panel (b) shows the cloud radiative effect (CRE) response to aerosol concentration derived from CESM2 (nonlinear; solid purple) and a linear response (dashed purple). Panel (c) shows the resulting CRE PDFs from the nonlinear and linear aerosol-CRE responses (solid and dashed lines, respectively). Vertical and horizontal lines in panels (a) and (c) represent the mean aerosol concentration and CRE, respectively, of each distribution. Panel (d) shows a 100-year aerosol concentration time series randomly drawn from the high and zero aerosol emissions variability PDFs (green and black lines, respectively). Panel (e) shows the resulting CRE from aerosol concentrations shown in panel (d) from the nonlinear and linear aerosol-CRE responses (solid and dashed lines, respectively).

CRE values (Figure 3.5e) confirm the time-averaged effect leading to differences in mean CRE shown in the time series in Figure 3.4. When emissions are low (and CRE is less negative), a nonlinear aerosol-CRE relationship results in much weaker (less negative) CRE values than if the relationship is linear (compare large positive deviations in CRE due to nonlinear and linear aerosol-CRE relationships).

3.4 Discussion

3.4.1 A need for more idealized experiments

To-date, there have been few sets of experiments that can be used to infer the impacts of BB emissions variability on the climate system. To the best of our knowledge, there has only been experiments conducted by Fasullo et al. (2022) and DeRepentigny et al. (2022), the CESM2-LE (Rodgers et al., 2021), and those performed for this study (Methods). As the only difference in forcing is the treatment of BB emissions variability, these experiments can be used to directly quantify the impact of BB emissions variability on the climate. Furthermore, we have conducted a set of idealized ESM simulations that allow us to quantify the difference in radiative forcing attributed to BB emissions variability.

It is important to assess how the radiative forcing is affected in more ESMs to understand how model-specific aerosol and cloud microphysics parameterizations may affect the forcing uncertainty attributable to aerosol emissions variability. For example, $\Delta\text{ERF}_{\text{BBVar}}$ may be particularly noticeable in CESM2 as it has relatively strong aerosol-cloud interactions (Smith et al., 2020). Understanding the strength of the $\Delta\text{ERF}_{\text{BBVar}}$ in ESMs is important for the design of future intercomparisons. Further idealized experiments, such as those described here, are necessary to detect and quantify the effect of aerosol variability on the effective radiative forcing due to aerosol-cloud interactions in a variety of ESMs. Current model intercomparison projects (i.e., those for CMIP6) are not adequate to attribute changes in the climate to differences in BB emissions variability because it is unlikely that quantifying statistically robust differences in climate is feasible without a direct comparison between high and low BB emissions variability scenarios. Indeed, we find no robust evidence of nonlinearity between annual BB emissions and CRE in individual ESM output submitted to the CMIP6 historical Atmospheric Model Intercomparison Project (AMIP; Figure 3.A7; Appendix 3.A.7; Gates et al., 1999; Eyring et al., 2016).

3.4.2 Implications

The temporal variability in BB aerosol emissions changes the climate forcing attributable to these aerosols. In particular, we show that realistic BB emissions variability leads to a weaker (less negative) forcing, compared to low emissions variability. This effect is particularly strong and widespread over the NH mid- to high-latitudes.

This ERF change (reduction in the magnitude of the total aerosol forcing) induced by BB emissions variability is due to nonlinear aerosol-cloud interaction effects.

These findings are of particular importance when considering the total aerosol forcing over historical periods and into the future. Most emissions inventories neglect realistic interannual variability (e.g., van Marle et al., 2017; Hoesly et al., 2018; O'Neill et al., 2016), which would lead to a more negative ERF due to aerosol-cloud interaction effects (ERF_{ACI}). Furthermore, many modelling approaches used to evaluate ERF_{ACI} do not prescribe realistic variability in aerosol emissions, if at all. For example, the Radiative Forcing Model Intercomparison Project (RFMIP) uses either fixed present-day or CMIP6 historical aerosol emissions that include only secular trends to quantify the radiative forcing of aerosols in CMIP6 ESMs; they do not include realistic BB emissions variability prior to 1997 (Pincus et al., 2016). Likewise, emissions prescribed for future projection scenarios (after 2014) also neglect temporal variability in aerosol emissions (recall Figure 3.1a; Riahi et al., 2017). We also note that, while the issues have been discussed here in the context of the interannual variability of BB emissions, these issues are likely relevant to other emissions sources that are sensitive to natural and anthropogenic variability (e.g., DMS emissions that are sensitive to ocean variability).

As treatments of aerosol variability differ in the historical, present-day, and future scenario simulations, significant biases in the total aerosol forcing may be present. The inclusion of interannual variability for some years, and neglect of it in others, will introduce discrepancies and discontinuities in the aerosol forcing that may be significant (such as spurious sea ice trends, as shown in DeRepentigny et al., 2022). To properly evaluate aerosol forcings and model past, present, and future climates, the temporal variability of aerosol emissions should be treated consistently and more realistically.

Past (prior to the satellite era) and future biomass burning aerosol emissions (and thus their variability) are uncertain. They will depend on many different factors, including changes in fire weather and fuel loads. As ESMs simulate aerosol-cloud interactions using more and more complex physics, they must also consider how BB aerosol emissions variability has changed through the past and into the future. Ideally, emissions variability should be prescribed with a carefully stated, well understood set of assumptions with impacts that can be evaluated and quantified. Alternatively, to avoid any assumptions of emissions variability, prognostic fire models should be integrated into the next generation of ESMs.

3.A Appendix to Chapter 3

Here, we present additional information regarding the Community Earth System Model version 2 Large Ensemble (CESM2-LE) data used for this study (Appendix 3.A.1); the methods we use to compute aerosol emissions and concentrations (Appendix 3.A.2); the methods we use to compute differences in effective radiative forcing (ERF; Appendix 3.A.3); aquaplanet simulations run to verify the driving role of aerosol-cloud interaction nonlinearities to differences in cloud properties (Appendix 3.A.4); the methods that we use to derive our heuristic model of the CRE response to aerosol concentration variability shown in Figure 3.5 (Appendix 3.A.5); the data we use from the Coupled Model Intercomparison Project Phase 6 (CMIP6) Atmospheric Model Intercomparison Project (AMIP) historical simulations (Appendix 3.A.6); methods used to evaluate if statistically-robust evidence of nonlinearities in aerosol emissions and cloud radiative effect exist (Appendix 3.A.7); and methods used to evaluate spatial statistical significance (Appendix 3.A.8).

We also present supplemental figures that further our findings in the main text. These figures show: the variability of biomass burning (BB) emissions prescribed in each idealized experiment from this study (Figure 3.A1); change in annual effective radiative forcing due to BB emissions variability (Figure 3.A2); change in annual cloud properties due to BB emissions variability (Figure 3.A3); change in cloud amount due to BB emissions variability (Figure 3.A4); change in clear-sky top of atmosphere net radiative flux and surface albedo due to BB emissions variability (Figure 3.A5); change in cloud properties due to BB emissions variability in aquaplanet simulations (Figure 3.A6); and cloud radiative effect (CRE) response at varying BB emissions averaged in CMIP6-AMIP models (Figure 3.A7).

3.A.1 CESM2 Large Ensemble

The Community Earth System Model version 2 Large Ensemble (CESM2-LE) is a project which contains data from 100 total ensemble members using CESM2 with CMIP6 historical forcing from 1850 to 2014 and future SSP3-7.0 (a medium-to-high emissions scenario) forcing from 2015 to 2100 (Rodgers et al., 2021; O'Neill et al., 2016). 50 ensemble members (of the total 100) were forced with the biomass burning (BB) emissions prescribed for CMIP6 historical and SSP3-7.0 scenario simulations. The other 50 ensemble members were forced with temporally smoothed BB emissions

during the late historical and early future projection periods, achieved with an 11-year running mean filter from 1990 to 2020. This smoothing reduces temporal variability in this ensemble set, but nearly preserves total emissions compared to the ensemble set containing the higher BB emissions variability (Rodgers et al., 2021). Each of the 100 ensemble members were simulated using a fully coupled configuration of CESM2 which is comprised of the Community Atmosphere Model version 6 (Danabasoglu et al., 2020, CAM6;), Parallel Ocean Program version 2 (Smith et al., 2010, POP2;), Los Alamos Sea Ice Model version 5.1.2 (Hunke et al., 2015, CICE5;), and Community Land Model version 5 (Lawrence et al., 2019, CLM5;). Aerosols were simulated using the four-mode version of the Modal Aerosol Module (Liu et al., 2016, MAM4;). Each component was configured at a nominal 1° spatial resolution (Rodgers et al., 2021). Each individual ensemble member was initialized using a combination of micro and macro perturbations to the temperature field; 80 members initialized from different phases of the Atlantic Meridional Overturning Circulation strength and 20 members initialized from randomly chosen years from a pre-industrial control run (Rodgers et al., 2021). We evaluate the impact of BB emissions variability (Figure 3.1 and 3.4) as the difference between the ensemble mean of the high BB emissions variability members and of the low BB emissions variability members, unless otherwise specified.

3.A.2 Aerosol emission and concentration calculations

Aerosol emissions (as shown in Figures 3.1 and 3.2 and concentrations (as shown in Figures 3.4 and 3.5) are computed as the sum of particle number amounts of each aerosol mode (i.e. num_a1, num_a2, num_a3, num_a4 in CESM2). Aerosol emissions are computed as the surface flux, as prescribed for each simulation. Aerosol concentrations are computed as the column-integrated atmospheric concentration.

3.A.3 Forcing calculation

We approximate the effective radiative forcing (ERF) by running simulations in CESM2 with fixed sea surface temperatures (SSTs). By holding SSTs constant, we remove most climate feedbacks by preventing the surface temperature from changing (Hansen et al., 2005; Forster et al., 2021). The land surface, however, is still active in our simulations, and thus able to change temperature in the presence of a forcing.

We adjust our ERF approximation for changes in land temperature by approximating the Planck feedback due to this land temperature change using a radiative kernel, as recommended by Forster et al. (2021). We use the land radiative kernel provided by Pendergrass et al. (2018). We thus use the following to calculate the ERF:

$$ERF = \Delta F_{fSST} - k\Delta T_{land} \tag{3.1}$$

Where ΔF_{fSST} is the change in net radiation flux at the top of atmosphere, k is the land radiation kernel, and ΔT_{land} is the change in land surface temperature. Differences are taken as the difference between high BB emissions variability scenarios (i.e., Real-Var and Pulse-Var) and the zero interannual variability baseline (Zero-Var).

We note that the radiative kernels provided by Pendergrass et al. (2018) were derived using a previous version to CAM6 used in this study (i.e., CAM5), however, radiative kernels derived from different models have been found to have little effect on the computed ERF (e.g., Gettelman et al., 2019; Smith et al., 2018, 2020; Zelinka et al., 2020).

3.A.4 Aquaplanet simulations

To evaluate if the response in clouds to changes in BB emissions variability is the result of land surface feedbacks, we simulate the Real-Var and Zero-Var scenarios using an aquaplanet configuration with CESM2. The aquaplanet simulations have no topography, land, or sea ice (i.e., are entirely covered by oceans), but otherwise use the same boundary conditions as our idealized fixed-SST simulations (see Section 2). Additionally, SSTs are prescribed to vary only with latitude and the orbital parameters are set to perpetual equinox conditions (Neale and Hoskins, 2000).

3.A.5 Idealized aerosol-CRE response

Figure 3.5 shows how the nonlinearity in the aerosol-CRE relationship results in a weakening of the magnitude (less negative) of CRE when there is greater aerosol emissions variability. Panel (a) in Figure 3.5 shows probability density functions (PDF) of aerosol concentrations that are representative of the Zero-Var (black) and Real-Var (green). The idealized aerosol PDFs are determined by fitting normal and

log-normal distributions to the June–September (JJAS) mean aerosol concentrations (Aer) averaged from Zero-Var and Real-Var simulations, respectively, averaged over 50–70°N. Panel (b) shows idealized CRE responses to aerosol concentration. The solid purple line shows a realistic nonlinear aerosol-CRE response, determined by fitting a logarithmic curve to the JJAS 50–70°N mean CRE responses to aerosol concentrations from all experiments used in this study (and shown in Figure 3.4, except the CESM2-LE). A nonlinear aerosol-CRE response is represented by the following equation (where a, b, c are fit constants):

$$CRE = a \cdot \ln(Aer + b) + c \tag{3.2}$$

The dashed purple lines shows a theoretical linear aerosol-CRE response, representative of an assumption that emissions variability has no effect on the time-averaged CRE response. The linear aerosol-CRE response is determined by fitting a linear curve to the JJAS 50–70°N mean CRE responses to aerosol concentrations from the Real-Var. The linear aerosol-CRE response is represented by the following equation (where d, e are fit constants):

$$CRE = d \cdot Aer + e \tag{3.3}$$

Panel (c) shows the resulting CRE PDFs from the normal and log-normal aerosol concentration PDFs. Solid (dashed) CRE PDFs show the transformation due to the nonlinear (linear) aerosol-CRE responses. Nonlinear CRE PDF transformations were performed by:

$$PDF_{CRE} = \left|\frac{Aer + b}{a}\right| \cdot PDF_{Aer} \tag{3.4}$$

Linear CRE PDF transformations were performed by:

$$PDF_{CRE} = \left|\frac{1}{d}\right| \cdot PDF_{Aer} \tag{3.5}$$

Panel (d) shows a time series of aerosol concentrations comprised of 100 randomly selected years from the normal and log-normal aerosol concentration PDFs (black and green lines, respectively). Panel (e) shows the corresponding CRE responses to the aerosol concentrations in panel (d). Solid (dashed) lines in panel (e) represent the response due to the nonlinear (linear) aerosol-CRE curves shown in panel (b).

3.A.6 CMIP6-AMIP data

We use Coupled Model Intercomparison Project Phase 6 (CMIP6) Atmospheric Model Intercomparison Project (AMIP) historical simulations to evaluate whether characteristic aerosol-cloud interaction nonlinearities can be found in other Earth System Models (ESMs; Figure 3.A7). We use all data available at the time of writing to compute the cloud radiative effect. The models (number of ensemble members) used are as follows: ACCESS-ESM1-5 (1), BCC-CSM2-MR (1), BCC-ESM1 (1), CAMS-CSM1-0 (3), CanESM5 (7), CESM2 (2), CESM2-FV2 (1), CESM2-WACCM (3), CESM2-WACCM-FV2 (1), CNRM-CM6-1 (1), CNRM-CM6-1-HR (1), CNRM-ESM2-1 (1), E3SM-1-0 (2), EC-Earth3-Veg (1), FGOALS-f3-L (3), GFDL-AM4 (1), GFDL-CM4 (1), GISS-E2-1-G (15), GISS-E2-2-G (1), HadGEM3-GC31-LL (5), HadGEM3-GC31-MM (2), INM-CM4-8 (1), INM-CM5-0 (1), IPSL-CM6A-LR (11), KACE-1-0-G (1), MIROC6 (10), MPI-ESM1-2-HR (1), MRI-ESM2-0 (3), NESM3 (5), NorCPM1 (1), NorESM2-LM (1), SAM0-UNICON (1), UKESM1-0-LL (2). Results are evaluated by pooling all ensemble members together. Cloud radiative effects simulated by each CMIP6-AMIP model are evaluated against the the CMIP6 prescribed BB emissions(van Marle et al., 2017).

We note that using BB emissions is less likely to yield statistically-robust evidence of nonlinear relationships to CRE, as compared to atmospheric aerosol concentrations. We suggest that aerosol concentrations would yield a better possibility of showing a statistically-robust evidence of a nonlinear relationship to CRE because the concentrations also consider differences in dispersion and deposition that may be influenced by emission variability. However, insufficient aerosol concentration data was provided to CMIP6.

3.A.7 Evaluating statistically-robust evidence of emissions-CRE nonlinearity

We categorize the response of cloud radiative effect (CRE) to biomass burning (BB) emissions to have statistically-robust evidence of the expected nonlinear response (based on CESM2 results; see Figure 3.4b; and past observational evidence Twomey, 1977; Rissman et al., 2004; Reutter et al., 2009; Bougiatioti et al., 2016; Kacarab et al., 2020) if the following criteria are met: (1) if the P-value of both (low and high BB emissions value) regression slopes are less than 0.1 using a Wald Test with

t-distribution; (2) if the P-value of the difference in slopes is less than 0.1 using an unpooled t-test; (3) if both slopes values are negative; (4) if the slope of the regression over low BB emissions values is more negative than the slope of the regression over high BB emissions values.

3.A.8 Evaluating spatial statistical significance

We use a Welch's t-test to assess the the statistical significance of differences at spatial scales (i.e., grid point; shown in figures as stippling). We additionally limit significance determinations for false discoveries (Wilks, 2016). We use an α_{FDR} of 0.20 to approximate a global significance level of 0.1.

3.A.9 Supplementary figures

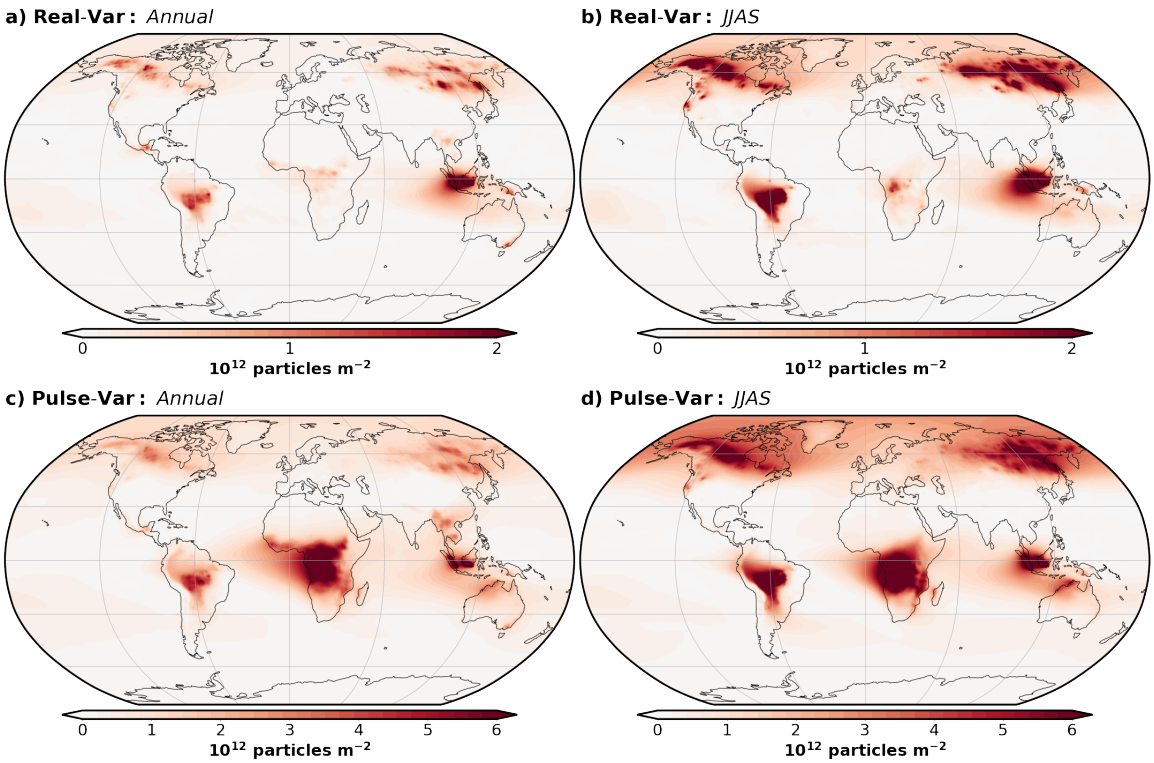

Figure 3.A1: **Variability of biomass burning (BB) column-integrated burden in each idealized experiment.** Shown is the standard deviation of BB column-integrated burden (in 10^{12} particles m^{-2}) in the Real-Var (a and b) and Pulse-Var (c and d) experiments for annual (a and c) and June–September (JJAS; b and d) means.

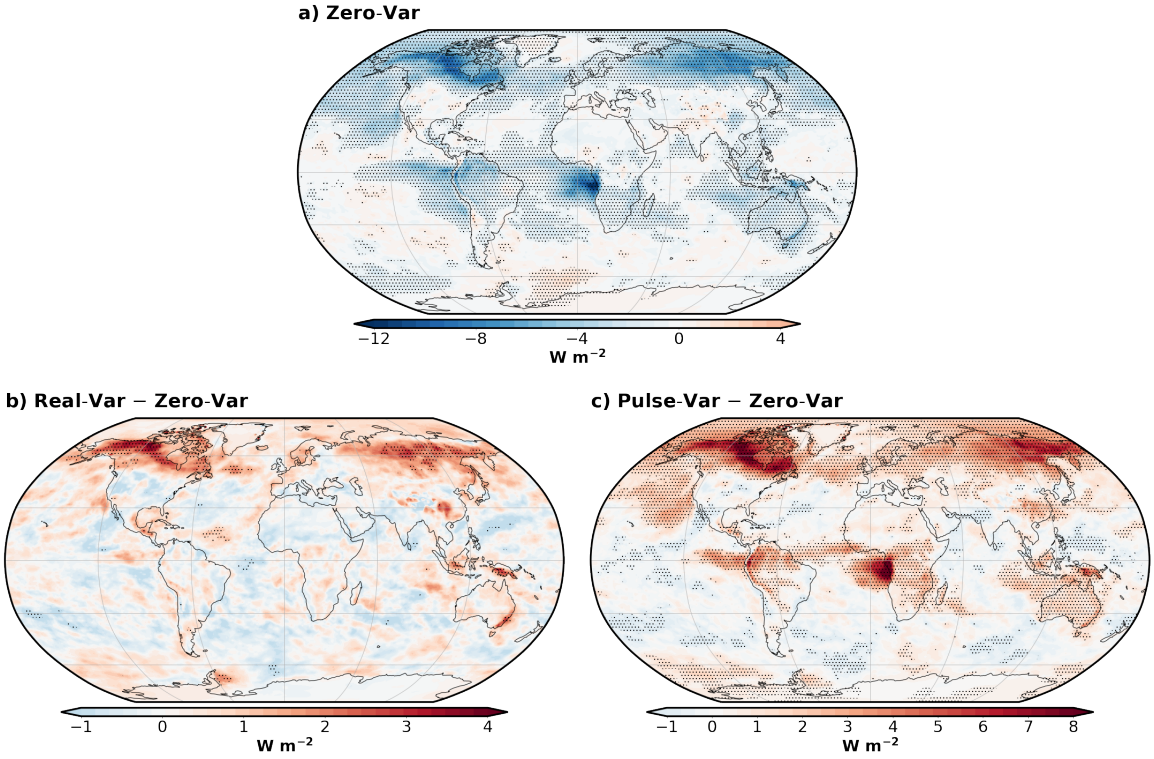

Figure 3.A2: **Change in annual effective radiative forcing due to biomass burning emissions variability (ΔERF_{BBVar}).** Panel (a) shows the absolute ERF due to BB emissions in the Zero-Var experiment (relative to no BB emissions). ΔERF_{BBVar} is shown for the Real-Var (Panel (b)) and Pulse-Var (Panel (c)) experiments. ΔERF_{BBVar} is defined as the variability experiments minus the Zero-Var experiment. Stippling signifies 90% confidence (see Appendix 3.A.7).

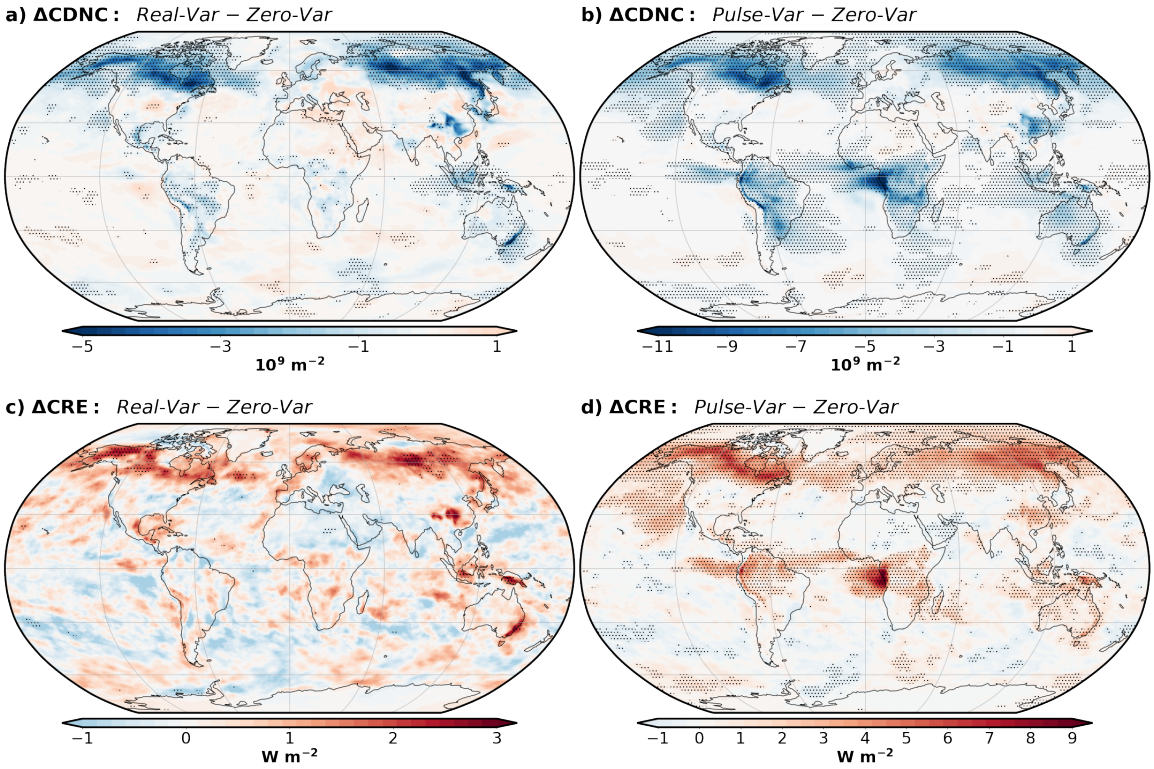

Figure 3.A3: **Annual mean change in cloud properties due to biomass burning (BB) emissions variability.** Annual mean change in cloud droplet number concentration (CDNC; in 10^9 m^{-2}; (a) and (b)) and cloud radiative effect (CRE; in W m^{-2}; (c) and (d)) due to BB emissions variability in the Real-Var (left column) and Pulse-Var (right column) experiments. Changes due to BB emissions variability are defined as the variability experiments minus the Zero-Var experiment. Stippling signifies 90% confidence (see Appendix 3.A.7).

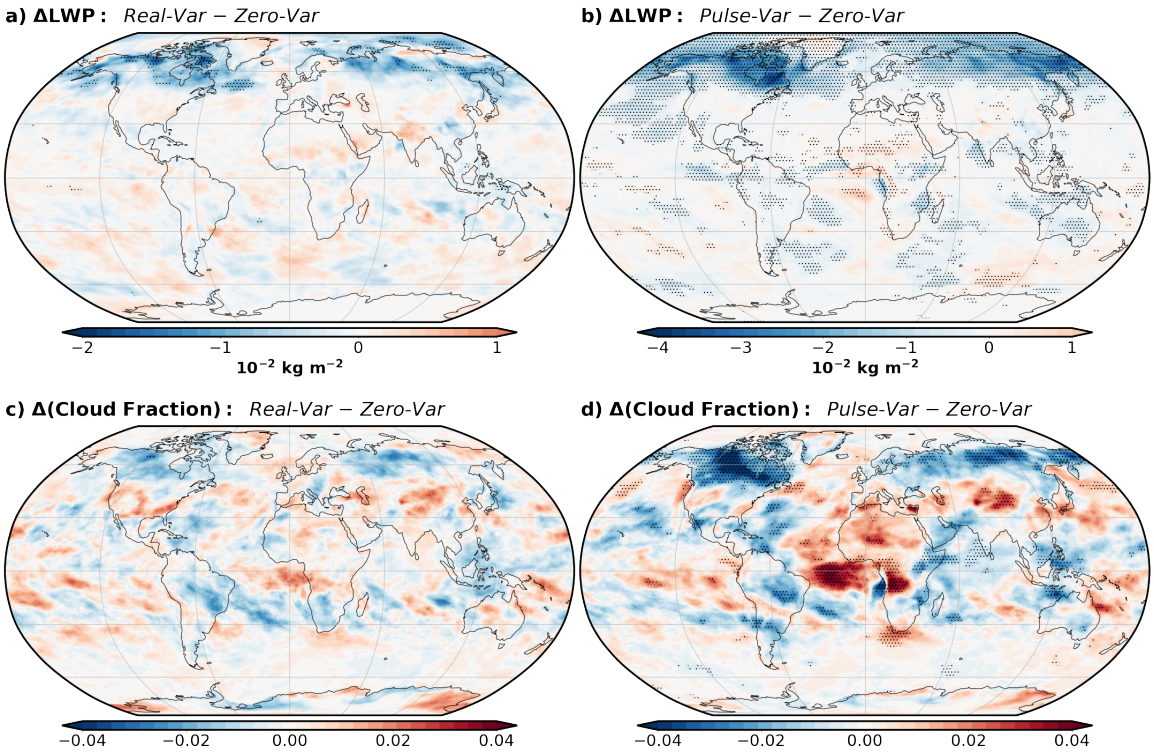

Figure 3.A4: **Change in cloud amount due to biomass burning (BB) emissions variability.** June–September (JJAS) mean change in liquid water path (LWP; in 10^{-2} kg m^{-2}; (a) and (b)) and fraction ((c) and (d)) due to BB emissions variability in the Real-Var (a) and Pulse-Var (b) experiments. Changes due to BB emissions variability are defined as the variability experiments minus the Zero-Var experiment. Stippling signifies 90% confidence (see Appendix 3.A.7).

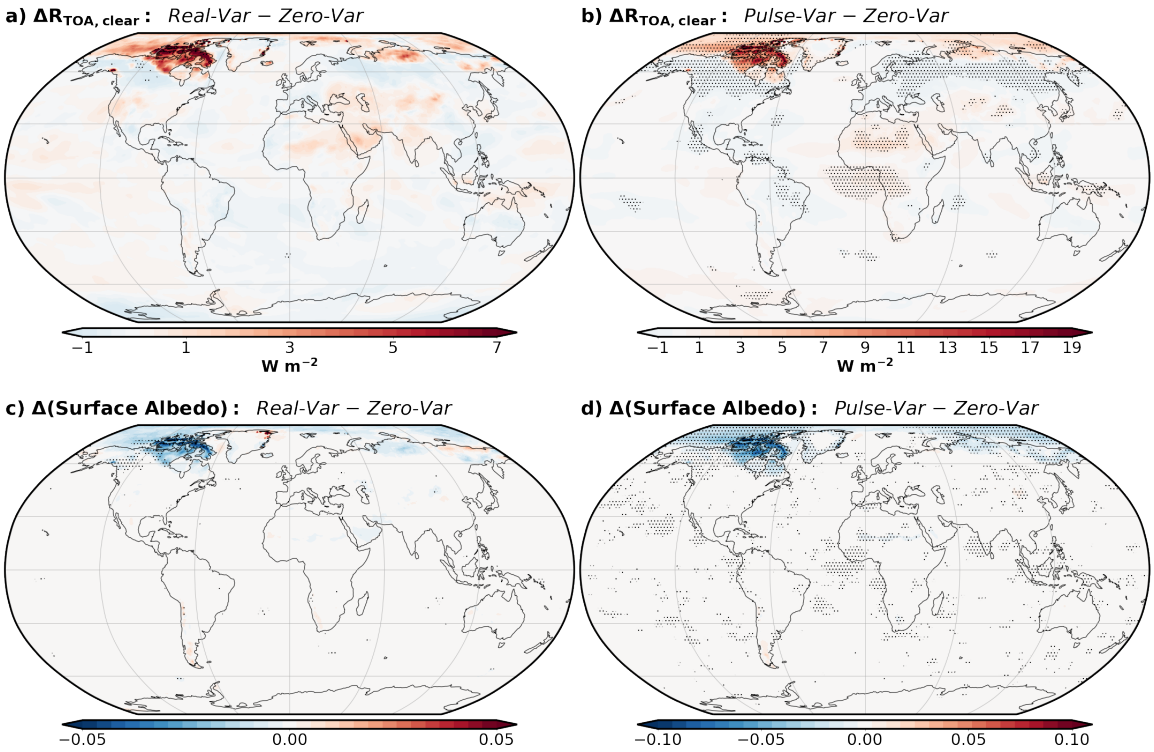

Figure 3.A5: **Change in clear-sky top of atmosphere net radiative flux ($R_{TOA,clear}$) and surface albedo due to biomass burning (BB) emissions variability.** As in Figure 3.A4 but for $R_{TOA,clear}$ (in W m^{-2}; (a) and (b)) and surface albedo ((c) and (d)).

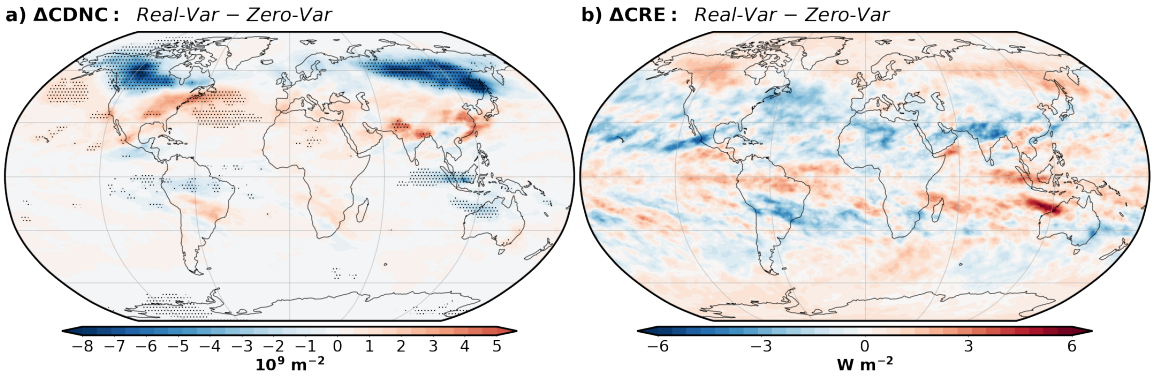

Figure 3.A6: **Change in cloud properties due to biomass burning (BB) emissions variability in aquaplanet simulations.** June–September (JJAS) mean change in cloud droplet number concentration (CDNC; in 10^9 m^{-2}; (a)) radiative effect (CRE; in W m^{-2}; (c)) due to BB emissions variability in the Real-Var experiment in an aquaplanet simulation. Changes due to BB emissions variability are defined as the variability experiments minus the Zero-Var experiment. Stippling signifies 90% confidence (see Appendix 3.A.7).

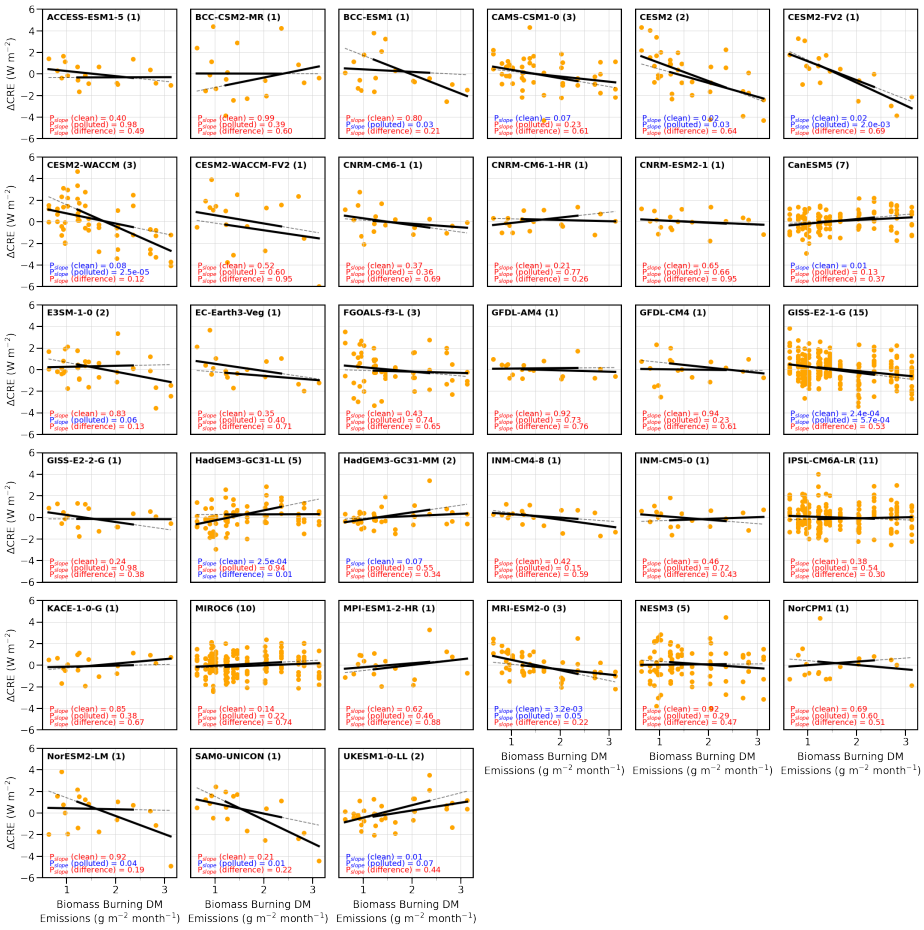

Figure 3.A7: **Cloud radiative effect (CRE) response at varying biomass burning (BB) emissions averaged in CMIP6-AMIP models.** Shown is the CRE response to varying BB emissions (shown as dry matter (DM) emissions) averaged from 50–70°N from data submitted to the CMIP6-AMIP historical simulations from 1997–2014. The number of ensemble members used for each model are shown in parentheses. See Appendix 3.A.5 for further information on data sources. CRE anomalies are relative to the monthly mean values. Black lines show linear regressions of the 80% most clean and polluted aerosol concentrations. P_{slope} (clean and polluted) refer to to the P-value of whether the slope is significant from zero for the clean and polluted regressions, respectively. P_{slope} (difference) refers to the P-value of whether the clean and polluted slopes are significantly different from each other. P-values highlight in blue (red) are (are not) significant to 90% confidence.

Chapter 4

An updated framework to understand regional mean precipitation change under warming

This study presents an updated framework for understanding regional precipitation change under climate forcing. We propose that most adjustments in regional precipitation (represented by the zonal mean) can be explained by three additive drivers: changes in global evaporation alter the overall availability of moisture for precipitation; shifts in the global moisture cycling rate affect the distance over which moisture is transported before precipitating; and atmospheric circulation adjustments further moderate changes in moisture transport distance. The global cycling rate of atmospheric moisture effectively explains many key features of the spatial pattern of zonal mean precipitation change, including the well-documented "wet-get-wetter, dry-get-drier" response. Furthermore, we find that the response of the global moisture cycling rate and its corresponding impact on moisture transport distance are robust across several state-of-the-art Earth System Models and forcing scenarios. Given the high level of certainty in how the global moisture cycling rate adjusts to warming, we can use the proposed framework to better understand, observe, and project changes in regional mean precipitation under current climate change.

The contents of this chapter have been submitted for consideration in the Journal of Climate as *Global moisture cycling rate an important control on regional mean*

precipitation under warming.

4.1 Introduction

As the world continues to warm, annual precipitation patterns are expected to change. We have high confidence that global precipitation will increase at a rate of approximately 2–3% per Kelvin of global-mean surface warming (Mitchell et al., 1987; Allen and Ingram, 2002; Douville et al., 2021). However, this global scaling does not apply uniformly across regions. Along with the overall increase, precipitation patterns will shift spatially, leading to heterogeneous changes. Some regions will see precipitation increases exceeding the global mean, while others will experience decreases (e.g., Douville et al., 2021).

Under current warming, these redistributions are expected to produce significant adjustments in regional precipitation. Generally, regions that already receive more precipitation (e.g., deep tropical and extratropical zones) are projected to become wetter, while drier regions (e.g., the subtropical zones) are expected to become drier (e.g., Held and Soden, 2006; Lau et al., 2013; Liu and Allan, 2013; Douville et al., 2021). Observational evidence suggests these expected changes may already be detectable (e.g., Seager and Naik, 2012; Liu and Allan, 2013; Chou et al., 2013; Polson et al., 2013; Douville et al., 2021). This enhancement of existing precipitation patterns, termed the "wet-get-wetter, dry-get-drier" response, aligns with projected moisture flux divergence patterns (Mitchell et al., 1987; Chou and Neelin, 2004; Held and Soden, 2006). Additional localized responses are expected, such as a narrowing of the Intertropical Convergence Zone (ITCZ), with intensified precipitation in the ITCZ core and drying at the edges (Byrne and Schneider, 2016), and a poleward expansion of the subtropical dry belt and midlatitude storm tracks (Seidel et al., 2008; Seager et al., 2010; Scheff and Frierson, 2012b,a).

Despite the societal relevance of these changes, understanding and constraining the projected spatial redistribution of precipitation remains challenging. One way to conceptualize and quantify these changes is to decompose total precipitation shifts into individual driving mechanisms. Approaches that rely on local-scale mass or energy balance frameworks are commonly used to analyze changes in regional precipitation (e.g., Held and Soden, 2006; Muller and O'Gorman, 2011; Richardson et al., 2016, 2018; Siler et al., 2018; Bonan et al., 2023a; Siler et al., 2023). However, these methods often fail to explain the underlying mechanisms by which global temperature

increases cause spatial shifts in precipitation.

For instance, local precipitation can be decomposed into contributions from radiative heating, sensible heat flux, and dry static energy flux divergence (Muller and O'Gorman, 2011). This energetic balance framework has been used to attribute precipitation changes to adjustments in each of these factors, with dry static energy flux divergence being the dominant term explaining changes in the spatial pattern (e.g., Muller and O'Gorman, 2011; Richardson et al., 2018; Bonan et al., 2023a). However, it remains unclear whether changes in dry static energy flux divergence cause changes in precipitation, or if the reverse is true (e.g., Fajber et al., 2023).

Alternatively, local mass balance can describe precipitation as the difference between surface evaporation and moisture flux divergence, based on the assumption that these three fluxes balance on long time scales (Peixoto and Oort, 1992):

$$P = E - \nabla \cdot Q \tag{4.1}$$

Where P, E, and $\nabla \cdot Q$ represent local annual mean precipitation, surface evaporation, and moisture flux divergence, respectively. Previous studies have used this simple mass balance of precipitation to infer changes from known adjustments in moisture flux divergence and surface evaporation (e.g., Held and Soden, 2006; Hwang and Frierson, 2010; Seager et al., 2010; Siler et al., 2018; Armour et al., 2019; Bonan et al., 2023b; Siler et al., 2023). For example, Held and Soden (2006) demonstrated that if moisture flux divergence scales with near-surface air moisture at approximately 7% K^{-1} and surface evaporation at 2% K^{-1}, the resulting first-order approximation of precipitation change mirrors the "wet-get-wetter, dry-get-drier" response of moisture flux divergence.

While the mass balance framework in Equation 4.1 offers insights into regional precipitation changes, we argue that simply separating surface evaporation from moisture flux divergence does not fully explain precipitation changes. In this study, we refine the framework to show how changes in both surface evaporation and moisture flux divergence, acting in unison, can be reframed and represented by global quantities that explain much of the simulated changes in precipitation. Specifically, we demonstrate that regional changes can be described by two well-constrained global quantities: hydrological sensitivity (the global rate of change of precipitation or evaporation per unit of global mean surface warming) and the rate of change in global moisture cycling. Hydrological sensitivity quantifies the extra moisture available for

global precipitation in a warmer climate, while changes in the moisture cycling rate reflect how long moisture remains in the atmosphere and how far it travels before precipitating. We show that changes in transport distance explain why regional precipitation shifts align with moisture flux divergence patterns (i.e., the "wet-get-wetter, dry-get-drier" paradigm; Held and Soden, 2006). Additionally, we attribute the remaining regional precipitation changes to shifts in atmospheric circulation.

Although increases in moisture transport distances under warming have been shown in the Community Earth System Model version 1 (CESM1; Singh et al., 2016b), and tied to reduced moisture cycling rates (Singh et al., 2016b; Siler et al., 2023), the direct influence of moisture cycling on precipitation changes has yet to be quantified across a broader set of Earth System Models (ESMs) and forcing scenarios. Here, we explain the spatial redistribution of zonal-mean precipitation in state-of-the-art ESMs as a lengthening of moisture transport distances. We demonstrate that the relationship between global moisture cycling rates and transport distances is robust across models and warming scenarios. By leveraging well-constrained global adjustments, the framework presented herein improves our understanding of why regional precipitation patterns change under warming.

Our work is organized as follows:

- Section 4.2 builds on existing understanding of global and regional scale moisture mass balance to develop an updated framework explaining changes in regional precipitation, showing that most zonal-mean precipitation responses to warming can be understood through global evaporation and water cycling rate adjustments, as well as atmospheric circulation changes.

- Section 4.3 shows that the response of zonal-mean precipitation to global water cycling rate adjustments can be understood as causing a lengthening of moisture transport distances, a robust feature across multiple Coupled Model Intercomparison Project Phase 6 (CMIP6) ESMs and warming scenarios.

- Section 4.4 leverages the framework from Section 4.2 and the explanation in Section 4.3 to demonstrate that important aspects of projected regional mean precipitation change can be explained using only well-constrained global-mean evaporation and moisture cycling rate adjustments.

- Section 4.5 uses ESM experiments with different forcing drivers to show that moisture cycling's effects on zonal-mean precipitation are a general feature of

global warming or cooling.

In this work, we represent the regional-mean precipitation change using zonal-mean quantities. Though we acknowledge this does not represent the full spatial extent of change (i.e., does not represent changes in the zonal direction), we use this method out of necessity for approximations in Sections 4.2 and 4.3, as well as for simplicity in proceeding analysis. We suggest that many of the following analyses and frameworks can be extended to both zonal and meridional precipitation adjustments and urge for this to be evaluated in future study.

4.2 The role of changing moisture cycling rates on regional precipitation

In this section, we develop an updated mass balance framework to describe zonal-mean precipitation change, leveraging two perspectives of moisture mass balance. First, we use the moisture source-to-sink framework developed by Singh et al. (2016a) and Singh et al. (2016b), which we describe briefly in the following subsection. This source-to-sink perspective provides intuition into regional precipitation as the sum of moisture sourced from all local and remote evaporation regions. We then combine this source-to-sink framework with a moisture mass balance at each location to show how local and remote changes in evaporation and moisture transport are influenced by the global moisture cycling rate, providing a lens through which to understand much of the simulated changes in regional mean precipitation.

4.2.1 Zonal-mean precipitation response controlled by redistribution of precipitation sources

Singh et al. (2016a) demonstrated that the spatial pattern of zonal-mean precipitation can be understood as the sum of moisture from all evaporative source regions, which can be numerically expressed as:

$$P = \mathbf{X_e} E \tag{4.2}$$

where P and E are vectors of precipitation and evaporation at each location, and $\mathbf{X_e}$ is a matrix of the fractional contributions to precipitation from each evaporation source. $\mathbf{X_e}$ indirectly describes the mass transport of moisture from each evaporative

source to precipitation sink. We hereafter refer to $\mathbf{X_e}$ as the precipitation source connectivity term. In this study, we approximate the precipitation source fractions ($\mathbf{X_e}$) using a one-dimensional box model (described in detail in Appendix 4.A.1). This approximation of meridional source regions is similar to that used by Siler et al. (2021), though structurally different.

Starting from Equation 4.2, we can describe precipitation changes as:

$$\begin{aligned} P' &= \mathbf{X_e}E' + \mathbf{X_e}'E + \mathbf{X_e}'E' \\ &\approx \mathbf{X_e}E' + \mathbf{X_e}'E \end{aligned} \tag{4.3}$$

where $[\cdot]'$ represents a change from a climatological state and the covariance term is negligible ($\mathbf{X_e}'E'$; see Figure 4.1d). Equation 4.3 shows that regional precipitation change results primarily from two contributors: first, a change in evaporation amount occurring at each source region ($\mathbf{X_e}E'$; first term), indicating how precipitation would change if the amount of evaporation from each source were to adjust; and second, a redistribution of the relative contribution of each moisture source ($\mathbf{X_e}'E$; second term; hereafter defined as precipitation source redistribution).

Using numerical water tracers in the Community Earth System Model version 1 (CESM1), Singh et al. (2016b) demonstrated that under CO_2 doubling, changes to the spatial structure of precipitation are predominantly driven by precipitation source redistribution ($\mathbf{X_e}'E$). We use our one-dimensional box model approximation of moisture source regions (see Appendix 4.A.1) to test if this result is robust across state-of-the-art Earth System Models (ESMs) and warming scenarios. In Figure 4.1, we show the influence of the two terms in Equation 4.3 on zonal-mean precipitation within different Coupled Model Intercomparison Project Phase 6 (CMIP6) warming scenarios (panel a shows the total zonal-mean changes from each ESM's preindustrial control simulation; see Appendix 4.A.2 for an overview of CMIP6 model output used). In panels b and c of Figure 4.1, the effects of warming on precipitation as described by Equation 4.3 are evident. Warming results in large-scale increases in evaporation, leading to more available moisture traveling from nearly all sources and increasing precipitation at all latitudes ($\mathbf{X_e}E'$; panel b). These precipitation adjustments due to increases in evaporation alone vary only slightly with latitude and consistently exhibit moderate increases in the deep tropics and northern hemisphere high latitudes. Summed over all sources, this first term represents the global adjustment of available moisture for precipitation and thus explains the expected global mean precipitation

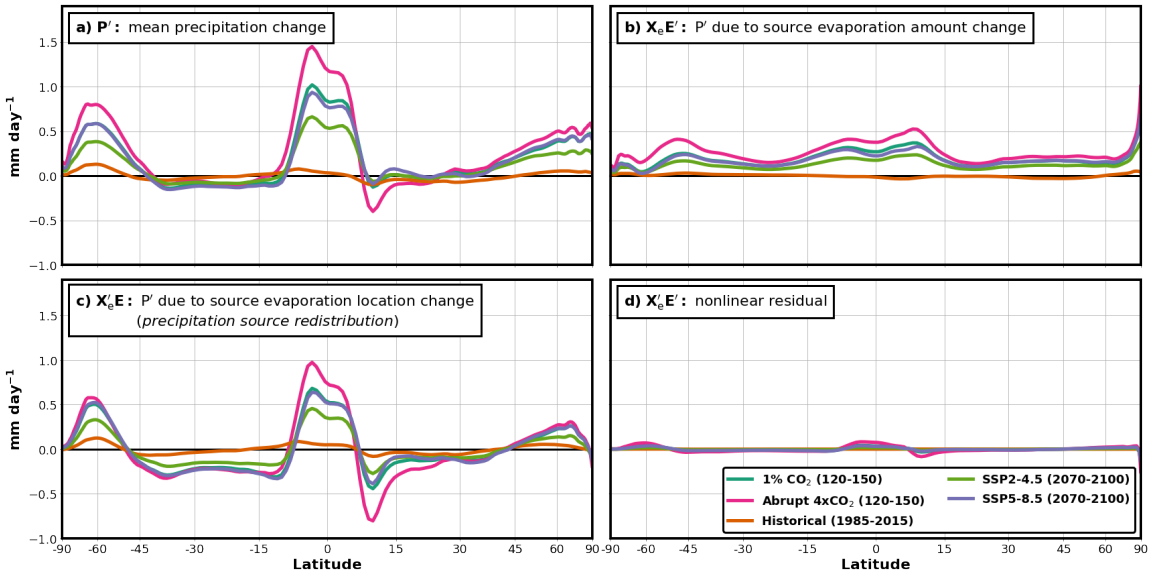

Figure 4.1: Zonal-mean precipitation change decomposed using a moisture transport framework, as described by Singh et al. (2016b) and expressed in Equation 4.3. Values are the multimodel ensemble mean from five different CMIP6 experiments. The legend in panel a describes which experiments are shown and the years that were averaged (in parentheses). Panel a shows the ensemble average zonal-mean precipitation change from each experiment. Panel b shows the change in precipitation amount that is explained by adjustments in the amount of evaporation from each source (holding relative contributions to each precipitation location constant; first term in Equation 4.3). Panel c shows the change in precipitation amount that is explained by adjustments in the relative contribution of each evaporative source to each precipitation sink (holding evaporation amount constant; second term in Equation 4.3). Panel d shows the nonlinear residual term in Equation 4.3.

change.

In contrast, many of the expected spatial features of zonal-mean precipitation change are explained by precipitation source redistribution ($\mathbf{X_e}'E$; panel c). For example, it is precipitation source redistribution that leads to an amplification and narrowing of the precipitation band within the deep tropics, a drying and widening of the subtropics, and some of the increased precipitation in the midlatitudes, including the poleward shift of the storm tracks. Our results are generally consistent with those of Singh et al. (2016b). Here we confirm that similar results are obtained across CMIP6 ESMs for each warming scenario examined. We can thus use the redistribution of precipitation sources as an explanation for why zonal-mean precipitation change is not determined by the global mean precipitation change.

4.2.2 Evaporation–divergence ratios play a dominant role in redistributing precipitation sources

To explain the influence of moisture cycling rates on regional mean precipitation, we combine the descriptions of global precipitation source redistribution ($\mathbf{X_e}'E$; as in Equation 4.3 and Figure 4.1c) and local mass balance.

Returning to Equation 4.1, we can rewrite changes in zonal-mean precipitation as:

$$P' = \eta E - \alpha \nabla \cdot Q \tag{4.4}$$

Where η and α represent the local fractional changes of E and $\nabla \cdot Q$, respectively (i.e., $\eta \equiv \frac{E'}{E}$ and $\alpha \equiv \frac{\nabla \cdot Q'}{\nabla \cdot Q}$). We then incorporate moisture mass balance (Equation 4.1) to obtain:

$$P' = \eta P + (\eta - \alpha) \nabla \cdot Q \tag{4.5}$$

Equation 4.5 shows that local-scale precipitation can be influenced by the fractional change in evaporation (ηP) or by a disparate fractional change in moisture divergence relative to evaporation ($(\eta - \alpha) \nabla \cdot Q$). This second term modulates precipitation scaling with local evaporation by removing more or less moisture via divergent transport. We refer to this difference in the fractional change in evaporation and moisture divergence ($\eta - \alpha$) as the change in the evaporation–divergence ratio, noting that $\eta - \alpha$ is the linear approximation of changes in the ratio of evaporation to moisture flux divergence. This term provides some physical intuition about local moisture cycling rates. As the magnitude of the evaporation–divergence ratio decreases, divergence dominates over evaporation, causing regions of divergence to experience less precipitation and regions of convergence to experience more. Though not an exact description of the local moisture cycling rate, this term provides a way to understand why local cycling rates change (see Läderach and Sodemann, 2016, for similar arguments). We can thus gain intuition on how moisture cycling rates influence zonal-mean precipitation by determining how the evaporation–divergence ratio affects precipitation source redistribution.

Combining Equations 4.2, 4.3, and 4.5 yields:

$$\begin{aligned} \mathbf{X_e}'E &= P' - \mathbf{X_e}E' \\ &= \eta(\mathbf{X_e}E) + (\eta - \alpha)\nabla \cdot Q - \mathbf{X_e}(\eta E) \end{aligned}$$

Further decomposing η into components representing the global mean and spatial anomaly from the global mean ($\overline{\eta}$ and $\tilde{\eta}$, respectively), we can express our representation of precipitation source redistribution as:

$$\begin{aligned} \mathbf{X_e}'E &= (\eta - \alpha)\nabla \cdot Q + \overline{\eta}(\mathbf{X_e}E) + \tilde{\eta}(\mathbf{X_e}E) - \mathbf{X_e}(\overline{\eta}E) - \mathbf{X_e}(\tilde{\eta}E) \\ &= (\eta - \alpha)\nabla \cdot Q + \left[\tilde{\eta}P - \mathbf{X_e}(\tilde{\eta}E)\right] \end{aligned} \tag{4.6}$$

The first term on the RHS of Equation 4.6 represents precipitation source redistribution due to adjustments in the evaporation–divergence ratio, while the term in square brackets represents precipitation source redistribution caused by spatial anomalies in the fractional change of evaporation.

Figures 4.2a and b show the influence of these two terms of Equation 4.6 (solid lines) on zonal-mean precipitation source redistribution. The total precipitation source redistribution ($\mathbf{X_e}'E$) is shown on each panel as dashed lines for reference. In panel a, we see that evaporation–divergence ratio adjustments result in a strong spatial redistributions of precipitation. Conversely, changes in the spatial pattern of evaporation (as described by the spatial anomaly from the global mean fractional change) are important for changing precipitation source redistribution only in high latitudes (panel b). Large relative increases in local evaporation in the high latitudes drive increased local precipitation, while smaller than average increases in evaporation over the Southern Ocean reduce local precipitation. The relative importance of changing evaporation for zonal-mean precipitation in the high latitudes supports the findings of Bintanja and Selten (2014), Singh et al. (2017), and Siler et al. (2021).

Outside of the high latitudes, the pattern of evaporation change has a negligible effect on precipitation source redistribution. Therefore, changes in precipitation driven by spatial redistribution can be well approximated using only evaporation–divergence ratio adjustments ($\eta - \alpha$). Hence, precipitation source redistribution can be closely approximated as:

$$\mathbf{X_e}'E \approx (\eta - \alpha)\nabla \cdot Q \tag{4.7}$$

Since the evaporation–divergence ratio is a proxy for changes in regional moisture cycling rates, this provides us a first step toward interpreting precipitation source redistribution in terms of adjustments to global moisture cycling.

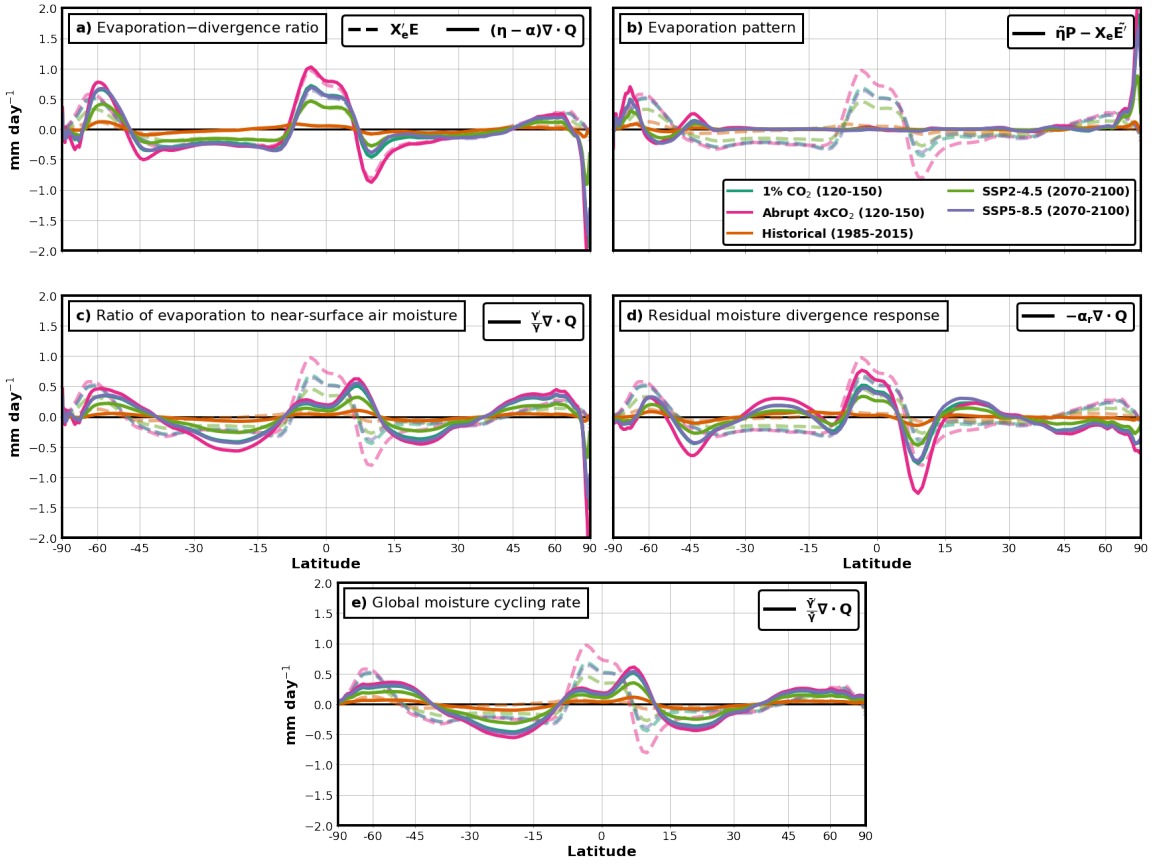

Figure 4.2: Zonal-mean precipitation source redistribution ($\mathbf{X_e}'E$; from Equation 4.3) decomposed into contributions described by Equations 4.6, 4.10, and 4.11. Values are the multimodel ensemble mean from five different CMIP6 experiments. Changes are relative to the annual mean from each model's respective pre-industrial control simulation. The legend in panel a describes which experiments are shown and the years that were averaged (in parentheses). Dashed lines in all panels represent the total zonal-mean precipitation source redistribution ($\mathbf{X_e}'E$; also shown in Figure 4.1c). Panel a shows the precipitation source redistribution response resulting from adjustments to the evaporation–divergence ratio ($(\eta - \alpha)\nabla \cdot Q$; first term in Equation 4.6). Panel b shows the precipitation source redistribution response resulting from changes in the spatial pattern of evaporation ($\tilde{\eta}P - \mathbf{X_e}(\tilde{\eta}E)$; second term in Equation 4.6). Panel c shows the precipitation source redistribution response resulting from adjustments to the ratio of evaporation to near-surface air moisture ($\frac{\gamma'}{\gamma}\nabla \cdot Q$; first term in Equation 4.10). Panel d shows the precipitation source redistribution response resulting from the residual moisture divergence response (defined in Equation 4.9; $-\alpha_r \nabla \cdot Q$; second term in Equation 4.10). Panel e shows the precipitation source redistribution as approximated by changes in the global moisture cycling rate ($\frac{\overline{\gamma}'}{\overline{\gamma}}\nabla \cdot Q$).

4.2.3 Important aspects of precipitation change explained by global moisture cycling rate

Though the evaporation–divergence ratio provides an approximate understanding of moisture cycling rate adjustments, other factors are also influential. For example, changes in evaporation–divergence ratio can also be driven by changes in atmospheric circulation. We begin to isolate these other influences by decomposing the evaporation–divergence ratio into two components: one approximating local moisture cycling rates more closely and another approximating changes due to circulation.

Held and Soden (2006) showed that, to first approximation, the proportional change in moisture divergence (α) can be represented as the proportional change in near-surface air moisture ($\alpha_q \equiv Q_s'/Q_s$). We thus can separate the influence of mean near-surface air moisture (α_q) from all other factors influencing moisture divergence (α_r), which we call the residual moisture divergence response:

$$\alpha = \alpha_q + \alpha_r \tag{4.8}$$

The residual moisture divergence response (α_r) can be understood as a response to changes in atmospheric circulation and the covariance of moisture content and circulation (Seager et al., 2010). Since changes in the covariance are relatively small (Seager et al., 2010; Siler et al., 2023), changes in atmospheric circulation can be assumed the dominant influence on the residual moisture divergence response. Equation 4.8 allows us to expand Equation 4.7 to represent precipitation source redistribution as:

$$\mathbf{X_e}'E \approx (\eta - \alpha_q)\nabla \cdot Q - \alpha_r \nabla \cdot Q \tag{4.9}$$

Next, we define the ratio of evaporation to near-surface air moisture as $\gamma \equiv E/Q_s$. This local ratio is similar to the depletion time constant used by Läderach and Sodemann (2016) and more closely approximates the rate at which moisture cycles through the atmosphere locally (relative to the evaporation-divergence ratio). Notably, $(\eta - \alpha_q)$ is the linear approximation of fractional changes in this ratio (i.e., $\eta - \alpha_q \approx \gamma'/\gamma$). Thus, Equation 4.9 becomes:

$$\mathbf{X_e}'E \approx \frac{\gamma'}{\gamma}\nabla \cdot Q - \alpha_r \nabla \cdot Q \tag{4.10}$$

Figure 4.2c shows that changes in the mean ratio of evaporation to near-surface

air moisture (γ'/γ) explain important features of precipitation source redistribution (first term of Equation 4.10). This first-order approximation explains much of the well-documented "wet-get-wetter, dry-get-drier" response (as previously explained by Held and Soden, 2006, for moisture divergence), except in the high latitudes where changes in local evaporation drive much of the increase, and in the deep tropics (Figure 4.2c). In comparison, the residual moisture divergence response contributes to the narrowing of the ITCZ, the expansion of the subtropics, and some of the poleward shift in midlatitude precipitation maxima (storm tracks), especially notable in the Southern Hemisphere. In essence, the residual moisture divergence response further modifies the precipitation source redistribution by regionally modulating the changes attributable to γ. To understand more about the residual moisture divergence response, we direct the reader to studies on this topic (e.g., Held and Soden, 2006; Scheff and Frierson, 2012a,b; Lorenz, 2014; Vallis et al., 2015; Byrne and O'Gorman, 2015; Siler et al., 2018).

Given that fractional changes in evaporation and near-surface air moisture at the local scale are well approximated by their respective global mean values (not shown), fractional changes in γ are also well approximated by the ratio of global mean evaporation and near-surface air moisture (i.e., $\overline{E}/\overline{Q_s}$; we define this ratio as $\overline{\gamma}$). Furthermore, since global changes in total column water vapor (Q) are well approximated by near-surface air moisture (O'Gorman and Muller, 2010), we arrive at the following approximation from fractional changes in γ:

$$\frac{\gamma'}{\gamma} \approx \frac{\overline{\gamma}'}{\overline{\gamma}} \tag{4.11}$$

Indeed, Figure 4.2e shows that the precipitation source redistribution under warming approximated by the fractional change in moisture cycling rate estimates the γ-driven precipitation response well (compare Figures 4.2c and e). We further note that $\overline{\gamma}$ represents the global moisture cycling rate, as described in the following section.

Equation 4.11 and Figure 4.2e suggest two powerful implications. First, we can explain important aspects of zonal-mean precipitation sensitivity to forcing using only two well-constrained global mean quantities: the sensitivities of global-mean evaporation and atmospheric moisture. Second, an understanding of precipitation source redistribution controlled by the global moisture cycling rate can be used to enhance our mechanistic understanding of why the spatial distribution of precipitation adjusts under warming. We use the following sections to dive deeper into the power of

these implications for explaining zonal-mean precipitation adjustment under warming.

4.3 Reduced moisture cycling rates with warming associated with robust moisture transport distance lengthening

Given that the global cycling rate of atmospheric moisture ($\overline{\gamma}$) can be computed as the ratio of global mean moisture content to evaporation, we can approximate its fractional change as:

$$\frac{\overline{\gamma}'}{\overline{\gamma}} \approx \frac{\overline{E}'}{\overline{E}} - \frac{\overline{Q}'}{\overline{Q}} \tag{4.12}$$

Thus, the global moisture cycling rate changes with warming based on the relative difference in the rates at which global mean evaporation and global atmospheric water content adjust. In the present-day climate, global mean evaporation is expected to increase at a rate of ∼2–3% K^{-1} (equal to global mean precipitation on sufficiently long time scales) and global mean moisture content at a rate of ∼7% K^{-1} (based on the Clausius-Clapeyron relation; Manabe and Wetherald, 1975; Mitchell et al., 1987; Stephens et al., 1994; Allen and Ingram, 2002; Held and Soden, 2006; O'Gorman and Muller, 2010). From Equation 4.12, we can thus expect a reduction in moisture cycling rate of ∼4–5% K^{-1}

The top panel of Figure 4.3 shows that the expected changes in global atmospheric moisture content (Figure 4.3a, expressed as near-surface air moisture) and global evaporation (Figure 4.3b) are consistent with changes simulated by CMIP6 ESMs under various warming scenarios (see Appendix 4.A.2 for further information on CMIP6 data used). Correspondingly, Figure 4.3c shows that there is a reduction in global moisture cycling rate, consistent with an expected reduction of approximately 4–5% K^{-1}.

Given this reduction in moisture cycling rate, we expect that lengthening of moisture transport distances must occur (i.e., if moisture lasts longer in the atmosphere, it must travel further distances if atmospheric circulation does not change). In this section, we provide evidence of robust increases in moisture transport distance, as well as a robust relationship between changes in global moisture cycling rate and transport distance under warming across virtually all models and warming scenario experiments. We further show that circulation and high latitude evaporation responses act

to moderate increases in global moisture transport distance.

4.3.1 Robust moisture transport distance increases under warming across Earth System Models

Model evidence suggests that moisture transport distances do indeed increase under warming. Singh et al. (2016b) demonstrated this in CESM1 under CO_2 doubling, and Siler et al. (2021) showed it under idealized zonal-mean temperature change. Here, we evaluate whether there is evidence of increases in moisture transport distance across CMIP6 ESMs under various idealized and scenario-based warming simulations.

We find consistent evidence of increased moisture transport distance in output from all ESMs submitted to CMIP6 under the different forced warming scenarios analyzed (see Appendix 4.A.2 for further information on CMIP6 data used). Figures 4.3a and b show the global and zonal-mean changes in moisture transport distance in each CMIP6 simulation. In this study, the moisture transport distance is defined as the approximated mass-weighted mean meridional distance that moisture is transported to its location of precipitation. The approximation is computed using the one-dimensional box model described in Section 4.2 (see Appendix 4.A.1 for details of this approximation).

Under warming, there is a robust global increase in moisture transport distance (Figure 4.3d). In the global average, this increase in meridional transport distance is projected to increase at a rate of approximately 4% K^{-1} of global surface warming. Figure 4.3e shows that the largest absolute increases in meridional transport distance occur in the mid- to high latitudes, with a tropical local maximum in the deep tropics. We suggest that little increases occur over the subtropics because these remain the major global evaporative source regions even in forced conditions (and thus supply moisture for precipitation locally). There is also a simulated decrease in transport distance in the Arctic, which is expected due to increases in local evaporation.

4.3.2 Lengthened moisture transport distance consistent with slowed moisture cycling rate

Figure 4.3f shows that increases in global mean moisture transport distance under warming within CMIP6 simulations are consistent with decreasing global moisture cycling rate across ESMs and forcing scenarios. However, there is not a direct one-

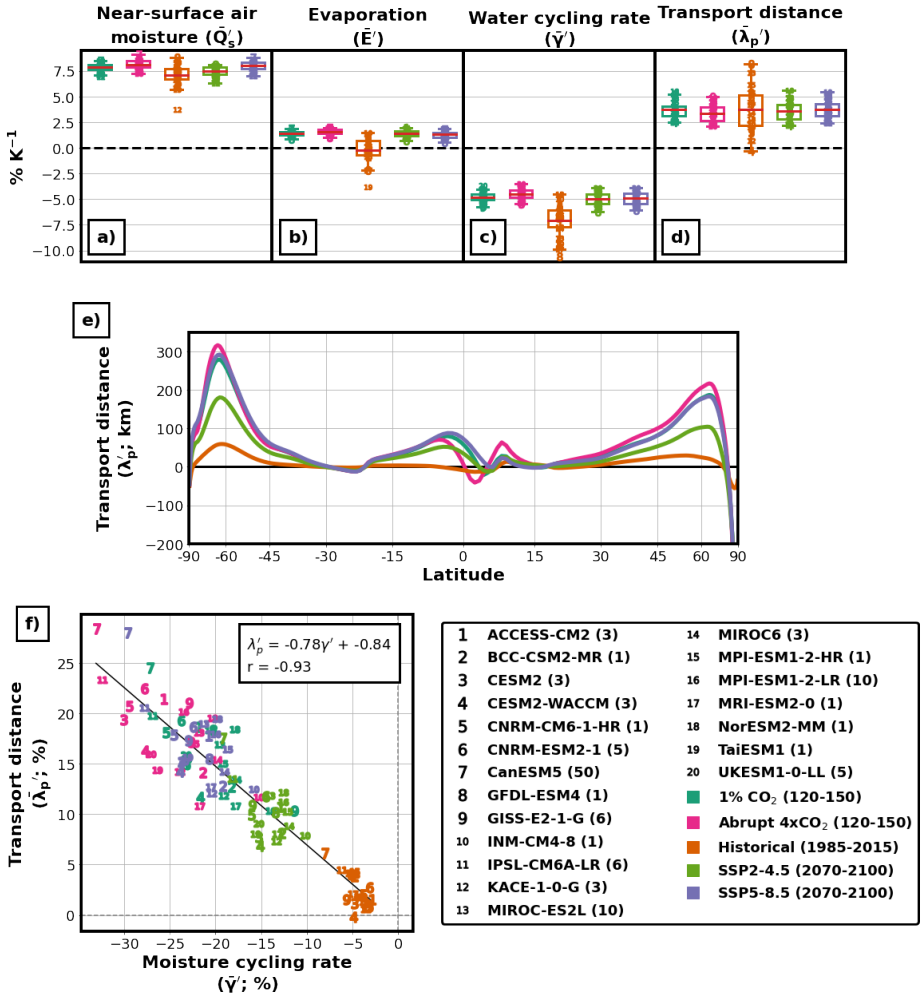

Figure 4.3: Changes in water cycling rate and meridional moisture transport distance across multiple CMIP6 warming experiments. Top panel shows the global mean change in near-surface air moisture (a; $\overline{Q}_s'$), global-mean evaporation (b; $\overline{E}'$), global moisture cycling rate (c; $\overline{\gamma}'$), and global-mean meridional moisture transport distance (d; $\overline{\lambda}_p'$; as defined in Appendix 4.A.1). Values represent the ensemble member average from each model (described in legend; number of ensemble members used reported in parentheses). Panel e shows the change in meridional moisture transport length distance at each latitude. Values are the multimodel ensemble mean from each CMIP6 experiment (colors shown in legend). Panel f shows the relationship between global moisture cycling rate and meridional transport distance across each CMIP6 model and experiment ensemble mean. The black line represents a linear regression across all ESMs and experiments and corresponds to the equation and correlation coefficient shown on plot.

to-one relationship between relative changes in global cycling rate and global mean moisture transport distance. Across ESMs and warming scenarios, there is an approximately 80% increase in transport distance per unit decrease in global cycling rate.

4.3.3 Circulation and high latitude evaporation act to moderate moisture transport distance increase

To better understand why adjustments in moisture transport distance do not have a one-to-one relationship with changes in moisture cycling rate, we compute the zonal change in meridional moisture transport distance implied by a globally uniform change in moisture cycling rate ($\hat{\lambda}'_{p,\overline{\gamma}'}$). This approximated moisture transport distance is calculated by re-approximating $\mathbf{X_e}$ assuming a spatially uniform change in moisture cycling rate (i.e., using a globally uniform change in evaporation and moisture cycling rate, while holding circulation constant). This approximation indicates how moisture transport distance would change if it were solely driven by the global water cycling rate, with no accompanying changes in circulation, moisture content covariability, or evaporation patterns.

The solid lines in Figure 4.4 demonstrate that using only adjustments to the global moisture cycling rate, the approximated transport distance ($\hat{\lambda}'_{p,\overline{\gamma}'}$) captures many first-order aspects of the simulated changes in distance (represented by dashed lines). Specifically, this approximation reflects features such as globally increased transport distances, local maximum in the deep tropics, minima in the subtropics, and approximately linear increases towards the poles in the extratropics.

Though changes in transport distance implied by global moisture cycling rate adjustments capture many key features of the total transport distance response, important regional nuances are missed (compare solid and dashed lines in Figure 4.4). We suggest that changes in evaporation patterns and circulation act to moderate the response to global moisture cycling rate by specifically describing dynamical changes at the ITCZ (e.g., narrowing and shifting; Kang et al. 2008; Lau and Kim 2015; Byrne and O'Gorman 2015), widening of the subtropics (Seager et al. 2007; Seidel et al. 2008), some poleward shifts in midlatitude storm tracks (Hall et al. 1994; Yin 2005; Bengtsson et al. 2006; Chang et al. 2012), and significant increases in high-latitude evaporation (Bintanja and Selten 2014).

We propose that these known circulation and spatial evaporation adjustments can

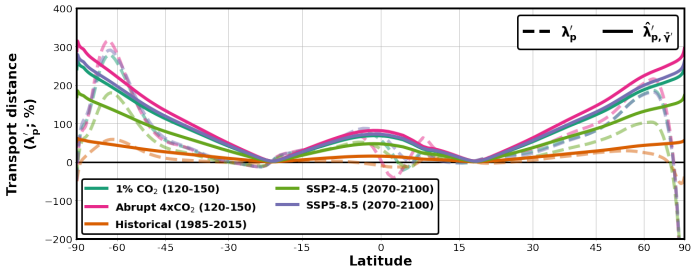

Figure 4.4: Changes in meridional moisture transport distance as approximated by the global moisture cycling rate across multiple CMIP6 warming experiments. Solid lines show the approximated moisture transport distance ($\hat{\lambda}'_{p,\bar{\gamma}'}$). Dashed lines show the actual moisture transport distance change (λ'_p; same as Figure 4.3e). Values are the multimodel ensemble mean from each CMIP6 simulations (colors shown in legend).

explain many of the observed differences between the simulated and approximated (i.e., from only spatially uniform changes in moisture cycling rate) meridional moisture transport distance. For instance, widening of the subtropics leads to increased local evaporation and locally sourced precipitation, with moisture sourced from the equatorward edge of the subtropics shifting towards the deep tropics (particularly noticeable at the poleward edges of the deep tropics), and moisture from the poleward edge of the tropics moving towards the mid- and high latitudes, which reduces mean moisture transport distance in these regions. Also, poleward shifting storm tracks tend to transport remotely sourced moisture further towards the poles, increasing transport distances particularly in the southern hemisphere. Furthermore, strong relative increases in high-latitude evaporation result in locally decreased transport distances.

4.4 A simple and mechanistic framework for regional precipitation change

We have demonstrated that the global moisture cycling rate is a key factor influencing zonal-mean precipitation change under warming (see Section 4.2). In this section, we combine this understanding with changes in global evaporation to show that we can approximate and understand zonal-mean precipitation changes using a set of simplified and mechanistic drivers.

We revisit Equation 4.2, which describes regional precipitation as influenced by changes in evaporation amount at each source ($X_e E'$) and the redistribution of precipitation sources ($X'_e E$). Noting that relative changes in evaporation (η) and the ratio of evaporation to near-surface air moisture (γ) are well approximated by their global means ($\overline{\eta}$, $\overline{\gamma}$, respectively), and that the influence of spatial evaporation patterns ($\tilde{\eta}$) on $X'_e E$ is negligible outside the high latitudes (Figure 4.2b), we modify Equations 4.3 and 4.10 to approximate changes in precipitation using global-mean evaporation, the global moisture cycling rate, and the residual moisture divergence response, as follows:

$$P' \approx \overline{\eta} P + \frac{\overline{\gamma}'}{\overline{\gamma}} \nabla \cdot Q - \alpha_r \nabla \cdot Q \tag{4.13}$$

The first term in Equation 4.13 approximates how precipitation would respond if all regions of precipitation scaled by the global-mean fractional increase in evaporation, analogous to the $X_e E'$ term in Equation 4.3. The second term uses only the

change in the global moisture cycling rate to approximate the change in precipitation due to adjusted moisture sources regions. The third term accounts for the residual moisture divergence response. We interpret these three contributors (terms in Equation 4.13) as additive effects on precipitation. Figure 4.5 depicts these additive effects on zonal-mean precipitation for the multimodel ensemble mean response from the CMIP6 Abrupt 4xCO_2 experiment. These additive effects can be interpreted as follows:

1. Precipitation scales with the global fractional change in evaporation from all source regions (i.e., $X_e E'$ approximated by $\overline{\eta} P$; shown by the blue line, see panel a).

2. Changes in the moisture cycling rate affect the time moisture spends in the atmosphere, altering the distance it is transported from source to sink, thereby redistributing the moisture change from the first term (i.e., $X'_e E$ approximated by $\frac{\overline{\gamma}'}{\overline{\gamma}} \nabla \cdot Q$; shown by the progression from the blue line to the red line, see panel b). This adjustment explains the redistribution of increased precipitation away from the subtropics and into the deep tropics and extratropics.

3. Additional climate adjustments (the residual moisture divergence response; $\alpha_r \nabla \cdot Q$; shown by the progression from the red line to by the pink line, see panel c) modulate precipitation source redistribution. As described in Section 4.2, the residual moisture divergence response is necessary to explain the remaining precipitation redistribution after accounting for changes in the global moisture cycling rate. For example, this response results in narrowing of the ITCZ, widening of the subtropics, and repositioning of the midlatitude precipitation maxima.

Comparing the black and pink lines in Figure 4.5c shows that Equation 4.13 explains most of the change in zonal-mean precipitation under warming. This explanatory power is especially evident outside the high latitudes, where local-scale changes in evaporation likely have a strong influence on local precipitation (Figure 4.2b; also see Bintanja and Selten 2014; Singh et al. 2017; Siler et al. 2021).

Although the residual moisture divergence response term is required to approximate the zonal-mean precipitation change most closely, we argue that an important proportion of the precipitation adjustment can be explained using only global-mean fractional changes in evaporation and moisture cycling rate. It is noteworthy that

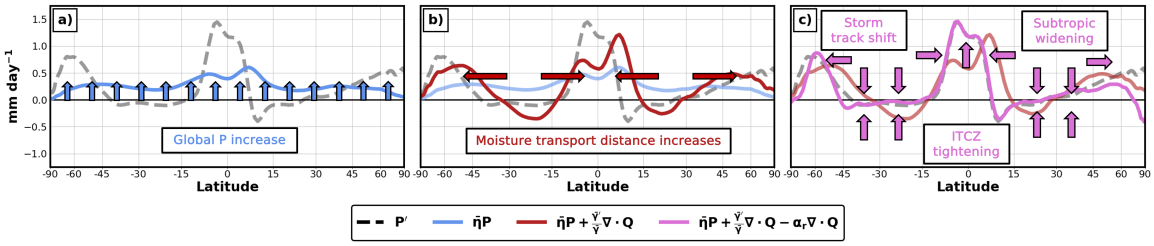

Figure 4.5: Changes in zonal-mean precipitation as approximated by adjustments in global mean evaporation ($\overline{\eta}$), the global water cycling rate ($\overline{\gamma}'$), and the residual moisture divergence response (α_r), which appear in Equation 4.13. Results shown represent the multimodel ensemble mean from the CMIP6 Abrupt 4xCO_2 experiment. The black dashed line represents the simulated zonal-mean precipitation response. The blue line represents a change in zonal-mean precipitation when approximated using only the response in global evaporation (first term in Equation 4.13). The red line represents a change in zonal-mean precipitation when also accounting for adjustments in the global moisture cycling rate (first two terms in Equation 4.13). The pink line represents a change in zonal-mean precipitation when accounting for all three terms in Equation 4.13.

these two adjustments depend on only three factors: hydrological sensitivity, global sensitivity to atmospheric moisture content, and global-mean surface temperature change. As the hydrological sensitivity and global sensitivity of atmospheric moisture content to warming are well constrained between ESMs, this suggests that a significant proportion of zonal-mean precipitation responses between different ESMs and forcing scenarios can be explained by global-mean surface temperature change and baseline climatological patterns precipitation and moisture flux divergence alone.

4.5 Moisture cycling rate important to regional precipitation across multiple forcing drivers under global surface temperature adjustment

Thus far, we have shown that zonal-mean precipitation changes across various CMIP6 ESMs and scenarios can largely be explained using global evaporation and moisture cycling rate, with additional adjustments primarily driven by the residual moisture divergence response. However, the scenarios analyzed above are either entirely driven by changes in CO_2 (Abrupt 4xCO_2 and 1% CO_2) or have CO_2 as the dominant forcing driver (Historical, SSP2-4.5, and SSP5-8.5; see Appendix 4.A.2 for further description of CMIP6 experiment scenarios used). Additionally, the previous analysis does not separate the effects of large-scale surface warming (known as the slow response) from the instantaneous effects of the forcing (fast response), leaving open the question of how much each factor in Equation 4.13 results from general surface temperature changes or the specific forcing type.

In this section, we test our simplified framework (Equation 4.13) to describe zonal-mean precipitation changes under four different forcing drivers and their respective slow and fast responses. We show that the global moisture cycling rate is a significant driver of regional mean precipitation changes across all forcing drivers after surface temperature changes (i.e. the slow response). Furthermore, we demonstrate that the global moisture cycling rate has little effect on regional precipitation under instantaneous radiative forcing and associated fast adjustments (i.e. the fast response).

To understand the influence of each term in Equation 4.13 on zonal-mean precipitation under the slow and fast responses of various forcing drivers, we use output from the Precipitation Driver Response Model Intercomparison Project (PDRMIP; Myhre et al., 2017). PDRMIP is a multimodel ensemble where each contributing modeling

center has simulated different single forcing perturbation experiments. These forcing perturbations were simulated under two configurations: fixed sea surface temperature and sea ice concentration, and fully coupled configurations (Myhre et al., 2017). Investigation of the climate response to each of these configurations allows for the diagnosis of the slow and fast climate responses to multiple forcing drivers (Hansen et al., 2005; Bala et al., 2010). Here, we use output from four different PDRMIP instantaneous perturbation experiments: a doubling of CO_2 concentrations (2xCO2), an increase in incoming solar irradiance by two percent (Sol+2%), a tripling of CH_4 (3xCH4), and a five-fold increase in SO_4 (5xSO4) (see Appendix 4.A.3 for further details on the PDRMIP data used and Appendix 4.A.4 for more information on slow and fast climate response calculations).

Figure 4.6 shows the total (combined slow and fast; left column), slow (middle column), and fast (right column) zonal-mean precipitation responses in terms of the additive contributors described by Equation 4.13 and explained in Section 4.4: adjustments in global evaporation ($\overline{\eta}P$), global moisture cycling rate ($\frac{\overline{\gamma}'}{\overline{\gamma}}\nabla \cdot Q$), and the residual moisture divergence response ($-\alpha_r \nabla \cdot Q$). Values represent the multimodel zonal-mean precipitation changes in PDRMIP simulations. Note that the results for the total response (Figure 4.6, left column) are similar to those shown in Section 4.4.

When decomposing the zonal-mean precipitation response into its slow and fast components (middle and right columns of Figure 4.6, respectively), the importance of global moisture cycling in explaining the precipitation response is apparent for the slow response. Conversly, the global moisture cycling rate is less effective at explaining the redistribution of precipitation in the fast response (Figure 4.6, right column): only after accounting for the residual moisture divergence response can we explain many qualitative features of fast zonal-mean precipitation change. The lack of fidelity in approximating fast zonal-mean precipitation change without the residual moisture divergence term may be driven by strong fast changes in circulation or heterogeneous changes in surface temperature (due to only the land surface warming), though this warrants further study.

As expected by our theoretical frameworks in Section 4.3, global-mean moisture transport distance changes correspond with moisture cycling rate adjustments in both slow and fast responses. Across PDRMIP models and forcing scenarios, a similar relationship exists between the global moisture cycling rate and mean transport distance: a decrease in the global moisture cycling rate corresponds with an increase in the moisture transport distance. The left column of Figure 4.7 shows that changes

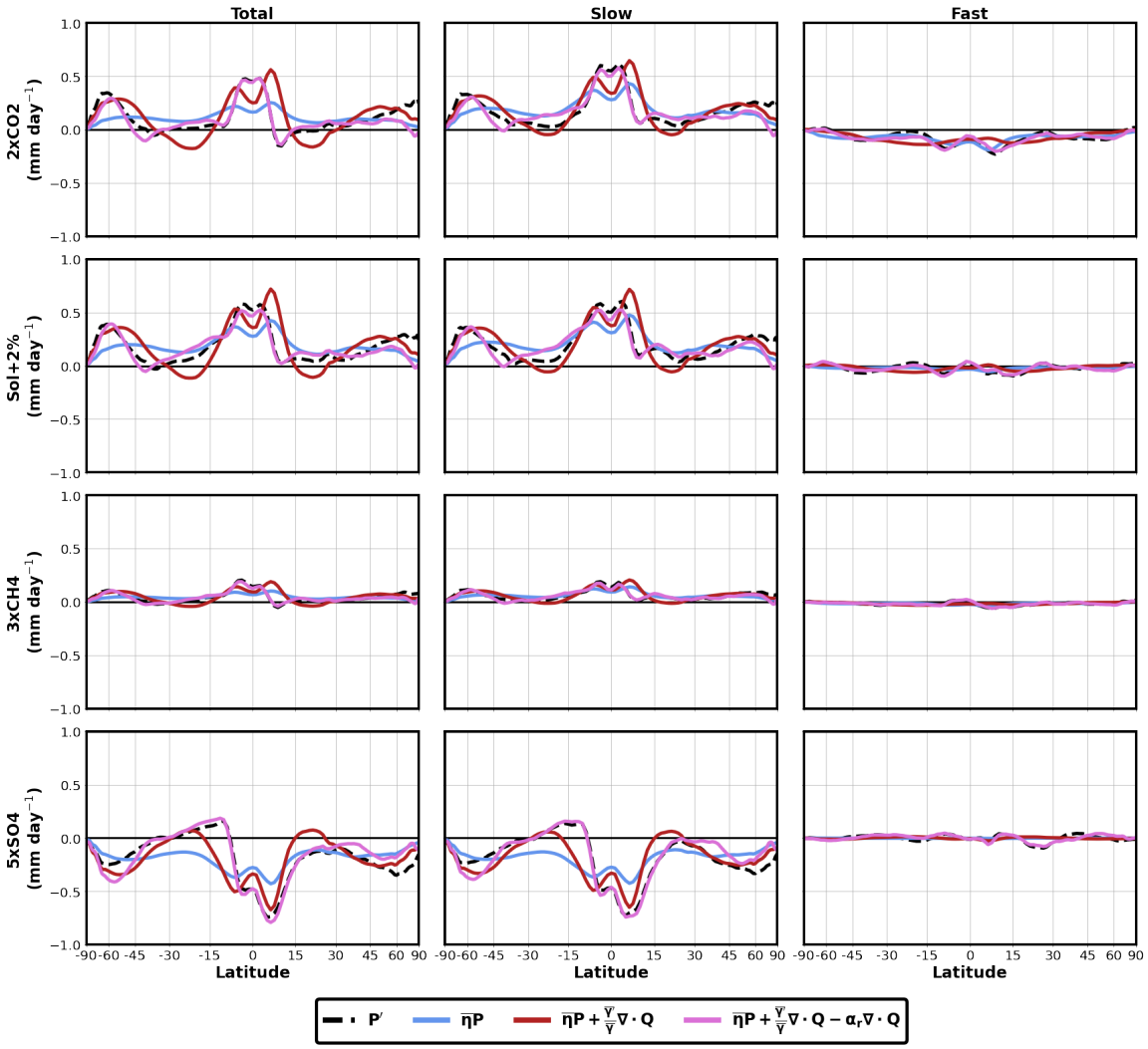

Figure 4.6: Changes in zonal-mean precipitation as approximated by adjustments in global evaporation ($\overline{\eta}$), the global moisture cycling rate ($\overline{\gamma}'$), and residual moisture divergence response (α_r), which appear in Equation 4.13. Results shown represent multimodel means of total (left column), slow (middle column), and fast (right column) response of the three terms in Equation 4.13 from various PDRMIP forcing scenario experiments. Black dashed lines represent the simulated zonal-mean precipitation responses. Blue lines represent a change in zonal-mean precipitation when approximated using only the response in global evaporation (first term in Equation 4.13). Red lines represent a change in zonal-mean precipitation when also accounting for adjustments in the global-mean moisture cycling rate (first two terms in Equation 4.13). Pink lines represent a change in zonal-mean precipitation when accounting for all three terms in Equation 4.13.

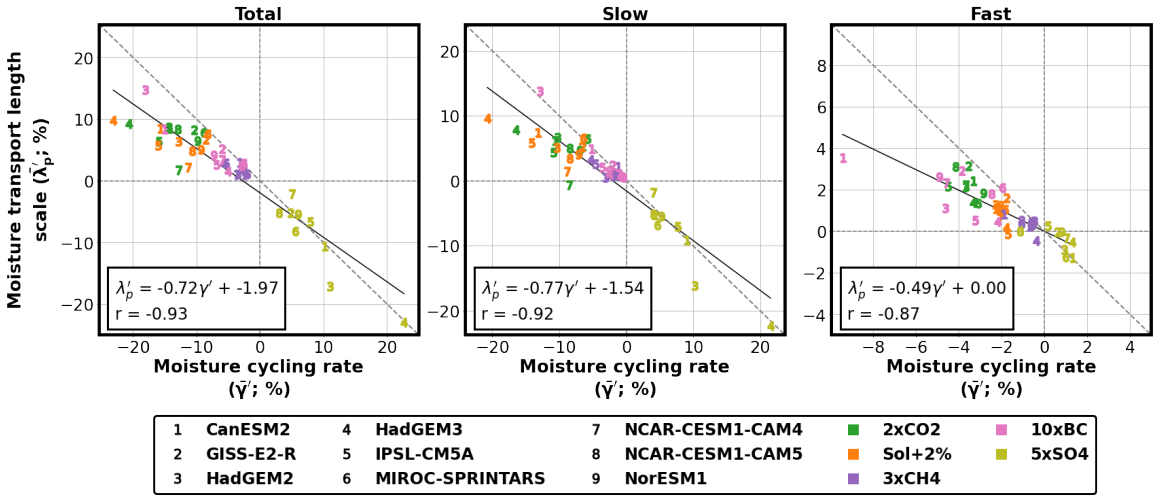

Figure 4.7: Relationship between global-mean atmospheric moisture cycling rate and meridional moisture transport distance across each PDRMIP models and forcing scenarios. Shown are global-mean total (left), slow (middle), and fast (right) responses. The black line represents a linear regression across all models and experiments and corresponds to the equation and correlation coefficient shown on each plot.

in the global moisture cycling rate and transport distance in the total response are highly correlated across PDRMIP models and scenarios, with a relationship similar to that of the CMIP6 simulations analyzed in Section 4.3 (compare to Figure 4.3f). This agreement between the moisture cycling rate and transport distance relationships in PDRMIP and CMIP6 models and scenarios suggests that this strong correlation is a robust feature of the Earth system. However, we note that the translation of transport distance change from fast alterations in the cycling rate is much less efficient than in the slow response ($\sim$0.5% vs. $\sim$0.8% of $\overline{\lambda}_p$ increase per percent of $\overline{\gamma}$ decrease in the fast versus slow responses). This reduced translation between moisture cycling rate and transport distance partially explains the apparent lack of dependence of the fast zonal-mean precipitation response on the global moisture cycling rate.

4.6 Conclusions

We provide a new framework for understanding regional precipitation change in which we describe adjustments in regional mean precipitation under climate forcing as a set of three additive drivers:

1. Global mean evaporation increases, altering moisture available for precipitation

globally.

2. The global rate at which moisture cycles in the atmosphere decreases, lengthening moisture transport distance. In general, longer moisture transport means that precipitation is redistributed from the subtropics into the deep tropics and extratropics.

3. Adjustments in circulation, modified by a small degree by the interactions between circulation and atmospheric moisture, act to moderate this precipitation redistribution.

Using this framework, we find that important aspects of regional precipitation adjustments under warming can be explained by understanding how the global cycling rate of atmospheric moisture changes. These findings are important for two reasons. First, using prior knowledge that the global moisture cycling rate must decrease with warming, we can develop an intuitive, mechanistic understanding of many important aspects of regional precipitation change. Namely, building upon the theories of Singh et al. (2016b) and Siler et al. (2021), we show that as the global moisture cycling rate slows under warming, moisture is transported further on average. The resulting redistribution of precipitation explains the "wet-get-wetter, dry-get-drier" mean precipitation response described by Held and Soden (2006). Importantly, the identified increases in moisture transport distance are robust across two generations of ESMs, suggesting a high degree of certainty that this is indeed a feature of the real world.

The fact that global changes in surface evaporation and moisture cycling explain much of the expected zonal-mean change in precipitation with warming allows us to use simple arguments about changes in global temperature and energy balance to explain regional precipitation adjustments. This provides a powerful degree of predictability for how regional precipitation might change under various forcing scenarios, which can be used to interpret more complex forcing scenarios, such as those that may be relevant for future geoengineering planning.

Furthermore, the connection between the global moisture cycling rate and regional precipitation provides a potential emergent constraint for regional precipitation change in ESM projections. By providing constraints on global mean warming, hydrological sensitivity, and the rate of change in atmospheric water content, we can evaluate which models may be more trustworthy when projecting adjustments in regional precipitation.

We do note, however, that using the global mean moisture cycling rate is ineffective at explaining fast precipitation responses (i.e., changes in precipitation before ocean surface warming occurs). We suggest that this may be due to the fact that other circulation adjustments are important on shorter timescales or because local cycling rates are decoupled from the global mean when changes in surface temperature are concentrated over land. However, ultimately, the fast response is small in magnitude compared to the slow response for most forcing scenarios.

More work is required to improve these approximations and understand how these changes manifest spatially and temporally. We suggest that using numerical water tracers to explicitly resolve Lagrangian moisture cycling rates (or residence time; such as those used by van der Ent and Savenije, 2011; Läderach and Sodemann, 2016; van der Ent and Tuinenburg, 2017; Fiorella et al., 2021) and their effect on moisture transport distance (and thus precipitation redistribution) is a promising method to do this. Such an approach would allow us to resolve the spatial structure in moisture cycling rate changes and evaluate its importance in influencing precipitation patterns.

Furthermore, there is not only a spatial redistribution of precipitation with warming, but also a temporal redistribution. One way this manifests is as increases in extreme precipitation (Trenberth, 1999; O'Gorman and Schneider, 2009; Pendergrass and Hartmann, 2014). Many have previously suggested that a slowing moisture cycling rate (or increased moisture residence time) may act to explain, at least partially, this increase in extreme precipitation (see also Gimeno et al., 2021). As water spends longer in the atmosphere, it is more likely to aggregate into heavier precipitation events. We do not directly investigate this possible influence; however, we suggest that this is another promising avenue for future research that could leverage numerical water tracing methods.

Coupling such tracers with observable quantities, such as water's isotope ratios, would provide a possible pathway to observe changes in water cycling and transport distance and benchmark simulations more precisely (e.g., Dee et al., 2023). We suggest that current and future large-scale observational networks, such as ground-based precipitation isotope observations or satellite-based water vapor isotopic measurements, may provide an avenue to observe a lengthening of the distance that moisture travels through the atmosphere from its place of evaporation to where it precipitates, providing unique insight into expected slowing of moisture cycling rates with warming.

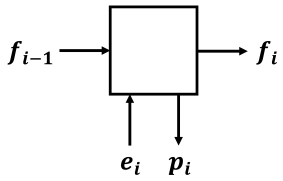

Figure 4.A1: **One-dimensional meridional moisture transport box model.** P_i, E_i, F_i represent the zonal mass of precipitation, evaporation, and column-integrated moisture transport at latitude location i.

4.A Appendix to Chapter 4

4.A.1 Moisture transport box model approximation and calculation of moisture transport length scale

To compute the meridional moisture transport length scale for each simulation, we approximate the zonal mean meridional transport length of moisture using a one-dimensional box model of atmospheric moisture transfer at each latitude (see Figure 4.A1). By assuming that each latitudinal location (i) is well-mixed in space, we approximate the moisture fraction ($x_{i,j}$) at location i originating from location j in both the outgoing moisture transport (f_i) and precipitation (p_i) using:

$$x_{i,j}(j = i) = \frac{e_i}{f_{i-1} + e_i} \tag{4.14}$$

and

$$x_{i,j}(j \neq i) = \frac{x_{i-1,j} f_{i-1}}{f_{i-1} + e_i} \tag{4.15}$$

where $f_0 = 0$, and e_i represents the evaporation at location i. A meridional moisture transport length scale (λ_p) is approximated as:

$$\lambda_{p,i} \equiv \sum_{j=0}^{i} x_{i,j} d_{i,j} \tag{4.16}$$

where $d_{i,j}$ is the horizontal distance from i to j. In this analysis, moisture is assumed to only travel in one direction: northward for regions of positive meridional moisture transport and southward for regions of negative meridional moisture transport.

4.A.2 CMIP6 data

We use data from the Coupled Model Intercomparison Project Phase 6 (CMIP6) ensemble under a variety of warming scenarios (Eyring et al., 2016). For this work, we utilize output from 20 different Earth System Models (ESMs). These ESMs include: ACCESS-CM2, BCC-CSM2-MR, CESM2, CESM2-WACCM, CNRM-CM6-1-HR, CNEM-ESM2-1, CanESM5, GFDL-ESM4, GISS-E2-1-G, INM-CM4-8, IPSL-CM6A-LR, KACE-1-0-G, MIROC-ES2L, MIROC6, MPI-ESM1-2-HR, MPI-ESM1-2-LR, MRI-ESM2-0, NorESM2-MM, TaiESM1, UKESM1-0-LL. Output from experiments representing warming scenarios are used. These scenarios include: a constant 1% annual increase in CO_2 concentrations (1% CO_2), an abrupt quadrupling of CO_2 concentrations (Abrupt 4xCO_2), as well as historical and Shared Socioeconomic Pathways SSP2-4.5 and SSP5-8.5 scenarios (O'Neill et al., 2016). All changes within CMIP6 experiment output is evaluated in reference to each model's preindustrial control simulation. For 1% CO_2 and 4xCO_2 the annual averages of years 120 to 150 were used. For historical, SSP2-4.5, and SSP5-8.5, the average of the last 30 years of each simulation were used (1985–2015 for historical and 2070–2100 for SSP2-4.5 and SSP5-8.5 experiments).

4.A.3 PDRMIP data

We use data from the Precipitation Driver Response Model Intercomparison Project (PDRMIP) ensemble under a variety of forcing scenarios (Myhre et al., 2017). PDRMIP involved simulating the response of single-driver perturbations in both fully-coupled and fixed sea surface temperature and sea ice concentration configurations with multiple ESMs. For this work, we utilize output from ten different ESMs: CanESM2, GISS-E2-R, HadGEM2, HadGEM3, IPSL-CM5A, MIROC-SPRINTARS, MPI-ESM, CESM1-CAM4, CESM1-CAM5, and NorESM1. Output from four different idealized and instantaneous forcing scenarios are used. These scenarios include: a doubling of CO2 concentrations (2xCO2), an increase in incoming solar irradiance by two percent (Sol+2%), a tripling of CH4 (3xCH4), and a five-fold increase in SO_4 (5xSO4).

4.A.4 Calculation of total, fast, and slow responses

We decompose the total precipitation, atmospheric moisture, moisture cycling rate, and moisture transport length scale responses as the combination of their fast and slow responses. We approximate the fast and slow responses using output from a combination of fully coupled and fixed sea surface temperature and sea ice concentration (fSST) simulations, following the methodology originally used by Hansen et al. (2005) to approximate radiative forcing and feedbacks and by applied to global precipitation by Bala et al. (2010) and Andrews et al. (2010). We approximate the total response as the change that occurs under forcing in fully coupled simulations, the fast response as the change in fSST simulations, and the slow response as the difference between the total and fast responses.

Chapter 5

Conclusion

Human influence has caused adjustments in Earth's atmospheric water cycle. If these influences continue at current scales, such changes are likely to intensify in the future. It is imperative that we improve our understanding and projections of these regional water cycle adjustments, enabling human societies to adapt to and mitigate impacts effectively.

This dissertation offers new insights into the large-scale response of the atmospheric water cycle to climate forcings, focusing specifically on the variability of biomass burning emissions and the implications of changes in global moisture cycling for regional precipitation patterns. Across the three chapters, analyses are presented that enhance our understanding of how both short-term aerosol emissions variability and long-term climate change affect the water cycle and its key components, such as precipitation, evaporation, and moisture transport. The findings contribute to the broader field of climate science, helping to illuminate the interconnected nature of our climate system. This conclusion summarizes the key findings of the dissertation and reflects on their broader implications and directions for future research.

5.1 Summary and significance of key findings

5.1.1 Chapter 2: Summary and significance of key findings

Chapter 2 demonstrates that temporal variability in biomass burning emissions affects the hydrologic cycle. The analysis, using output from the CESM2 Large Ensemble, reveals that greater simulated variability in emissions leads to increases in evaporation, atmospheric moisture content, mean precipitation, and precipitation extremes.

These changes align with a thermodynamic response to warming. However, this amplification is moderated by several factors, including increased ocean heat storage, weakened meridional energy transport, and altered precipitation efficiency at higher latitudes. The study suggests that these findings likely apply to other CMIP6 models, as all utilize the same biomass burning emissions inventories as boundary conditions.

The significance of these findings lies in recognizing that interannual variability in biomass burning emissions introduces a previously unidentified source of uncertainty in simulated water cycle projections. This variability influences broad hydrological fields, potentially skewing baseline comparisons and the strength of future projections, particularly in the Northern Hemisphere mid- to high latitudes. The chapter emphasizes the need for careful treatment of biomass burning emissions in future Earth system modeling and highlights the importance of replicating this experiment across different Earth system models to assess the robustness of the results. Understanding this variability is crucial for accurate projections of regional hydrological responses. By incorporating realistic interannual variability of biomass emissions, regional projections and predictions of the global water cycle can be improved.

5.1.2 Chapter 3: Summary and significance of key findings

Chapter 3 investigates how temporal variability in biomass burning aerosol emissions alters overall aerosol radiative forcing, particularly through aerosol-cloud interactions – explaining the mechanism by which temporal variability in biomass burning emissions leads to an amplified water cycle (as described in Chapter 2). The study shows that when realistic interannual variability in emissions is considered, the resulting forcing is weaker (less negative) than under low emissions variability, particularly in the Northern Hemisphere mid- to high latitudes. This weaker time-averaged radiative forcing is attributed to nonlinear aerosol-cloud interaction effects. The findings are significant for understanding aerosol forcing over historical periods and in future projections, as most emissions inventories and models neglect realistic variability, leading to a possible overestimation of the cooling effect associated with aerosols.

This chapter underscores the importance of integrating more accurate representations of aerosol variability into Earth System Models, especially those used in major projects like future coupled model intercomparison projects. Neglecting variability may introduce biases in projections, potentially distorting our understanding of aerosol-induced climate effects and, consequently, the climate response. While the

chapter focuses on biomass burning emissions, the implications extend to other aerosol emission sources influenced by both natural and anthropogenic variability. This study calls for more consistent treatments of aerosol emissions variability in models, either through improved inventories or prognostic fire models, to better capture the complexity of aerosol-climate interactions. These findings are crucial for refining our understanding of aerosol forcing and reducing uncertainties in climate projections, particularly regarding the balance between aerosol-induced cooling and greenhouse gas-induced warming.

5.1.3 Chapter 4: Summary and significance of key findings

Chapter 4 presents a new framework for understanding regional precipitation changes in response to climate warming, identifying three primary drivers: increases in global mean evaporation, slower global moisture cycling, and adjustments in atmospheric circulation. Among these drivers, the global moisture cycling rate emerges as particularly important. As the rate of global moisture cycling decreases, the distance moisture is transported increases, redistributing precipitation from the subtropics to the deep tropics and extratropics. This redistribution helps explain the "wet-get-wetter, dry-get-drier" pattern observed in regional precipitation responses to warming, a pattern and relationship robust across multiple generations of Earth System Models and forcing drivers. The chapter highlights how global changes in evaporation and moisture cycling can account for much of the expected zonal-mean precipitation changes, offering a simplified, mechanistic understanding of regional precipitation adjustments under various forcing scenarios.

The significance of these findings lies in the framework's ability to predict regional precipitation changes using basic principles of global-mean energy balance and temperature. This provides a powerful tool for interpreting complex climate forcing scenarios, including those relevant for future geoengineering efforts. The connection between global moisture cycling and regional precipitation also offers a potential emergent constraint for evaluating Earth System Models, aiding in the identification of models that are most reliable in projecting significant regional precipitation changes. These findings enhance our understanding of how global climate forcings affect regional precipitation, thereby improving the predictability of hydrologic responses under warming.

5.2 Synthesis of Results

The synthesis of this dissertation's findings revolves around a central theme: improving our understanding of how the spatial patterns of the global water cycle adjust under climate forcing. Across the chapters, we deepen our understanding of the atmospheric water cycle's response to different forcings, offering insights into the mechanisms driving these changes and providing tools for improving future projections. Collectively, these chapters converge on explanations for how the spatial patterns of the global atmospheric water cycle adjust in response to different external forcings. Contained in this dissertation are explanations for the amplification of the hydrologic cycle due to biomass burning emissions variability (described in Chapters 2 and 3) and the redistribution of moisture under global-scale warming via altered cycling rates (explained in Chapter 4). These findings not only enhance our theoretical understanding but also offer practical tools for improving the accuracy of climate projections, ultimately helping society better anticipate and adapt to the regional impacts of global climate change.

5.3 Future Directions

The research presented in this dissertation opens several promising avenues for future study, particularly in the context of enhancing our understanding of how climate forcings influence the global and regional water cycle.

One critical area for further investigation involves expanding the analysis of biomass burning emissions variability beyond the CESM2 model to other Earth System Models within the CMIP6 ensemble. The results of Chapters 2 and 3 highlight that different models may exhibit varying sensitivities to this variability, potentially increasing uncertainty in hydrological projections. To address this, future work should focus on replicating the experiments across a broader range of models to assess the robustness of the findings and potentially reduce inter-model spread in hydrological cycle projections.

Another important direction, as outlined in Chapter 3, is the need for better representation of aerosol emissions variability in Earth System Models. The findings suggest that neglecting realistic interannual variability in biomass burning emissions leads to large biases in estimating aerosol radiative forcing, which in turn affects projections of hydrological responses. Future research should aim to develop more

comprehensive emissions inventories that incorporate realistic variability and explore the integration of prognostic fire models into next-generation Earth System Models. Such efforts would not only enhance our understanding of aerosol-induced climate impacts but also provide more accurate projections of the water cycle's adjustments in response to aerosol emissions.

Chapter 4 points to the potential of using global moisture cycling rates as a predictive tool for understanding regional precipitation changes under warming. Future work could build on this framework by employing numerical water tracers to explicitly resolve Lagrangian moisture cycling rates and their influence on precipitation redistribution. This approach would enable us to better capture the spatial structure of moisture transport and evaluate its role in shaping regional precipitation patterns. Additionally, linking these modeling efforts with observational data, such as isotope-based measurements of atmospheric moisture, could provide valuable constraints on model projections and insights into the slowing of moisture cycling rates due to global warming. Expanding the use of observational networks, such as ground-based or satellite-based measurements of water isotopes, would also facilitate the direct observation of changes in moisture transport distances and enhance the benchmarking of Earth System Model predictions and projections.

Furthermore, while Chapter 4 focuses primarily on the slow regional precipitation response to warming, there remains a need to better understand the fast response, particularly in regions where circulation adjustments play a more prominent role. Investigating the decoupling of local moisture cycling from the global mean during the fast adjustment stage in response to radiative forcing could yield new insights into these rapid precipitation adjustments, especially over land. Future research that integrates both fast and slow responses into a comprehensive framework would improve the predictability of regional hydrological changes across various timescales.

Lastly, the connection between slower moisture cycling rates and the intensification of extreme precipitation events, as noted in Chapter 4, presents another fruitful area for future research. Exploring the extent to which changes in moisture residence time contribute to increases in precipitation extremes could help elucidate the relationship between global warming and hydrological extremes. By combining numerical water tracing with extreme precipitation analyses, we could gain a deeper understanding of the mechanisms driving the temporal redistribution of precipitation and the conditions that lead to more intense precipitation events in a warming world.

Bibliography

Allan, R. P., Willett, K. M., John, V. O., and Trent, T. (2022). Global Changes in Water Vapor 1979–2020. *Journal of Geophysical Research: Atmospheres*, 127(12):e2022JD036728. _eprint: https://onlinelibrary.wiley.com/doi/pdf/10.1029/2022JD036728.

Allen, M. R. and Ingram, W. J. (2002). Constraints on future changes in climate and the hydrologic cycle. *Nature*, 419(6903):224–232.

Andrews, T. and Forster, P. M. (2010). The transient response of global-mean precipitation to increasing carbon dioxide levels. *Environmental Research Letters*, 5(2):025212.

Andrews, T., Forster, P. M., Boucher, O., Bellouin, N., and Jones, A. (2010). Precipitation, radiative forcing and global temperature change. *Geophysical Research Letters*, 37(14).

Andrews, T., Forster, P. M., and Gregory, J. M. (2009). A Surface Energy Perspective on Climate Change. *Journal of Climate*, 22(10):2557–2570.

Armour, K. C., Siler, N., Donohoe, A., and Roe, G. H. (2019). Meridional Atmospheric Heat Transport Constrained by Energetics and Mediated by Large-Scale Diffusion. *Journal of Climate*, 32(12):3655–3680.

Bala, G., Caldeira, K., and Nemani, R. (2010). Fast versus slow response in climate change: implications for the global hydrological cycle. *Climate Dynamics*, 35(2):423–434.

Barsugli, J. J. and Battisti, D. S. (1998). The Basic Effects of Atmosphere–Ocean Thermal Coupling on Midlatitude Variability. *Journal of the Atmospheric Sciences*, 55(4):477–493. Publisher: American Meteorological Society Section: Journal of the Atmospheric Sciences.

Bates, B., Kundzewicz, Z. W., and IPCC, editors (2008). *Climate change and water*. IPCC Technical Paper; 6.

Bengtsson, L., Hodges, K. I., and Roeckner, E. (2006). Storm Tracks and Climate Change. *Journal of Climate*, 19(15):3518–3543. Publisher: American Meteorological Society Section: Journal of Climate.

Bintanja, R. and Selten, F. M. (2014). Future increases in Arctic precipitation linked to local evaporation and sea-ice retreat. *Nature*, 509(7501):479–482.

Bonan, D. B., Feldl, N., Zelinka, M. D., and Hahn, L. C. (2023a). Contributions to regional precipitation change and its polar-amplified pattern under warming. *Environmental Research: Climate*, 2(3):035010.

Bonan, D. B., Siler, N., Roe, G. H., and Armour, K. C. (2023b). Energetic Constraints on the Pattern of Changes to the Hydrological Cycle under Global Warming. *Journal of Climate*, 36(10):3499–3522.

Bougiatioti, A., Bezantakos, S., Stavroulas, I., Kalivitis, N., Kokkalis, P., Biskos, G., Mihalopoulos, N., Papayannis, A., and Nenes, A. (2016). Biomass-burning impact on CCN number, hygroscopicity and cloud formation during summertime in the eastern Mediterranean. *Atmospheric Chemistry and Physics*, 16(11):7389–7409.

Broccoli, A. J., Dahl, K. A., and Stouffer, R. J. (2006). Response of the ITCZ to Northern Hemisphere cooling. *Geophysical Research Letters*, 33(1).

Byrne, M. P. and O'Gorman, P. A. (2015). The Response of Precipitation Minus Evapotranspiration to Climate Warming: Why the "Wet-Get-Wetter, Dry-Get-Drier" Scaling Does Not Hold over Land*. *Journal of Climate*, 28(20):8078–8092.

Byrne, M. P. and Schneider, T. (2016). Narrowing of the ITCZ in a warming climate: Physical mechanisms. *Geophysical Research Letters*, 43(21):11,350–11,357. _eprint: https://onlinelibrary.wiley.com/doi/pdf/10.1002/2016GL070396.

Caretta, M. A., Mukherji, A., Arfanuzzaman, M., Betts, R. A., Gelfan, A., Hirabayashi, Y., Lissner, T. K., Lopez Gunn, E., Liu, J., Morgan, R., Mwanga, S., and Supratid, S. (2023). Water. In *Climate Change 2022 – Impacts, Adaptation and Vulnerability: Working Group II Contribution to the Sixth Assessment Report of the Intergovernmental Panel on Climate Change*, pages 551–712. Cambridge University Press, Cambridge.

Carslaw, K. S., Lee, L. A., Reddington, C. L., Pringle, K. J., Rap, A., Forster, P. M., Mann, G. W., Spracklen, D. V., Woodhouse, M. T., Regayre, L. A., and Pierce, J. R. (2013). Large contribution of natural aerosols to uncertainty in indirect forcing. *Nature*, 503(7474):67–71.

Chang, E. K. M., Guo, Y., and Xia, X. (2012). CMIP5 multi-model ensemble projection of storm track change under global warming. *Journal of Geophysical Research: Atmospheres*, 117(D23). _eprint: https://onlinelibrary.wiley.com/doi/pdf/10.1029/2012JD018578.

Chou, C., Chiang, J. C. H., Lan, C.-W., Chung, C.-H., Liao, Y.-C., and Lee, C.-J. (2013). Increase in the range between wet and dry season precipitation. *Nature Geoscience*, 6(4):263–267. Publisher: Nature Publishing Group.

Chou, C. and Neelin, J. D. (2004). Mechanisms of Global Warming Impacts on Regional Tropical Precipitation*. *Journal of Climate*, 17(13):2688–2701.

Cook, B. I., Mankin, J. S., Marvel, K., Williams, A. P., Smerdon, J. E., and Anchukaitis, K. J. (2020). Twenty-First Century Drought Projections in the CMIP6 Forcing Scenarios. *Earth's Future*, 8(6):e2019EF001461. _eprint: https://onlinelibrary.wiley.com/doi/pdf/10.1029/2019EF001461.

Danabasoglu, G., Lamarque, J.-F., Bacmeister, J., Bailey, D. A., DuVivier, A. K., Edwards, J., Emmons, L. K., Fasullo, J., Garcia, R., Gettelman, A., Hannay, C., Holland, M. M., Large, W. G., Lauritzen, P. H., Lawrence, D. M., Lenaerts, J. T. M., Lindsay, K., Lipscomb, W. H., Mills, M. J., Neale, R., Oleson, K. W., Otto-Bliesner, B., Phillips, A. S., Sacks, W., Tilmes, S., van Kampenhout, L., Vertenstein, M., Bertini, A., Dennis, J., Deser, C., Fischer, C., Fox-Kemper, B., Kay, J. E., Kinnison, D., Kushner, P. J., Larson, V. E., Long, M. C., Mickelson, S., Moore, J. K., Nienhouse, E., Polvani, L., Rasch, P. J., and Strand, W. G. (2020). The Community Earth System Model Version 2 (CESM2). *Journal of Advances in Modeling Earth Systems*, 12(2):e2019MS001916.

Dee, S. G., Bailey, A., Conroy, J. L., Atwood, A., Stevenson, S., Nusbaumer, J., and Noone, D. (2023). Water isotopes, climate variability, and the hydrological cycle: recent advances and new frontiers. *Environmental Research: Climate*.

DeRepentigny, P., Jahn, A., Holland, M. M., Kay, J. E., Fasullo, J., Lamarque, J.-F., Tilmes, S., Hannay, C., Mills, M. J., Bailey, D. A., and Barrett, A. P. (2022).

Enhanced simulated early 21st century Arctic sea ice loss due to CMIP6 biomass burning emissions. *Science Advances*, 8(30):eabo2405.

Djehdian, L. A., Chini, C. M., Marston, L., Konar, M., and Stillwell, A. S. (2019). Exposure of urban food–energy–water (FEW) systems to water scarcity. *Sustainable Cities and Society*, 50:101621.

D'Odorico, P., Davis, K. F., Rosa, L., Carr, J. A., Chiarelli, D., Dell'Angelo, J., Gephart, J., MacDonald, G. K., Seekell, D. A., Suweis, S., and Rulli, M. C. (2018). The Global Food-Energy-Water Nexus. *Reviews of Geophysics*, 56(3):456–531. _eprint: https://onlinelibrary.wiley.com/doi/pdf/10.1029/2017RG000591.

Douville, H., Raghavan, K., Renwick, J., Allan, R., Arias, P., Barlow, M., Cerezo-Mota, R., Cherchi, A., Gan, T., Gergis, J., Jiang, D., Khan, A., Pokam Mba, W., Rosenfeld, D., Tierney, J., and Zolina, O. (2021). Water Cycle Changes. In Masson-Delmotte, V., Zhai, P., Pirani, A., Connors, S., Péan, C., Berger, S., Caud, N., Chen, Y., Goldfarb, L., Gomis, M., Huang, M., Leitzell, K., Lonnoy, E., Matthews, J., Maycock, T., Waterfield, T., Yelekçi, O., Yu, R., and Zhou, B., editors, *Climate Change 2021: The Physical Science Basis. Contribution of Working Group I to the Sixth Assessment Report of the Intergovernmental Panel on Climate Change*, pages 1055–1210. Cambridge University Press, Cambridge, United Kingdom and New York, NY, USA.

Eyring, V., Bony, S., Meehl, G. A., Senior, C. A., Stevens, B., Stouffer, R. J., and Taylor, K. E. (2016). Overview of the Coupled Model Intercomparison Project Phase 6 (CMIP6) experimental design and organization. *Geoscientific Model Development*, 9(5):1937–1958.

Fajber, R., Donohoe, A., Ragen, S., Armour, K. C., and Kushner, P. J. (2023). Atmospheric heat transport is governed by meridional gradients in surface evaporation in modern-day earth-like climates. *Proceedings of the National Academy of Sciences*, 120(25):e2217202120.

Fasullo, J. T., Lamarque, J.-F., Hannay, C., Rosenbloom, N., Tilmes, S., DeRepentigny, P., Jahn, A., and Deser, C. (2022). Spurious Late Historical-Era Warming in CESM2 Driven by Prescribed Biomass Burning Emissions. *Geophysical Research Letters*, 49(2):e2021GL097420.

Fiorella, R. P., Siler, N., Nusbaumer, J., and Noone, D. C. (2021). Enhancing Understanding of the Hydrological Cycle via Pairing of Process-Oriented and Isotope Ratio Tracers. *Journal of Advances in Modeling Earth Systems*, 13(10):e2021MS002648.

Forster, P., Storelvmo, T., Armour, K., Collins, W., Dufresne, J.-L., Frame, D., Lunt, D., Mauritsen, T., Palmer, M., Watanabe, M., Wild, M., and Zhang, H. (2021). The Earth's Energy Budget, Climate Feedbacks, and Climate Sensitivity. In Masson-Delmotte, V., Zhai, P., Pirani, A., Connors, S., Péan, C., Berger, S., Caud, N., Chen, Y., Goldfarb, L., Gomis, M., Huang, M., Leitzell, K., Lonnoy, E., Matthews, J., Maycock, T., Waterfield, T., Yelekçi, O., Yu, R., and Zhou, B., editors, *Climate Change 2021: The Physical Science Basis. Contribution of Working Group I to the Sixth Assessment Report of the Intergovernmental Panel on Climate Change*, pages 923–1054. Cambridge University Press, Cambridge, United Kingdom and New York, NY, USA.

Gates, W. L., Boyle, J. S., Covey, C., Dease, C. G., Doutriaux, C. M., Drach, R. S., Fiorino, M., Gleckler, P. J., Hnilo, J. J., Marlais, S. M., Phillips, T. J., Potter, G. L., Santer, B. D., Sperber, K. R., Taylor, K. E., and Williams, D. N. (1999). An Overview of the Results of the Atmospheric Model Intercomparison Project (AMIP I). *Bulletin of the American Meteorological Society*, 80(1):29–55.

Gettelman, A., Hannay, C., Bacmeister, J. T., Neale, R. B., Pendergrass, A. G., Danabasoglu, G., Lamarque, J.-F., Fasullo, J. T., Bailey, D. A., Lawrence, D. M., and Mills, M. J. (2019). High Climate Sensitivity in the Community Earth System Model Version 2 (CESM2). *Geophysical Research Letters*, 46(14):8329–8337.

Gimeno, L., Eiras-Barca, J., Durán-Quesada, A. M., Dominguez, F., van der Ent, R., Sodemann, H., Sánchez-Murillo, R., Nieto, R., and Kirchner, J. W. (2021). The residence time of water vapour in the atmosphere. *Nature Reviews Earth & Environment*, 2(8):558–569.

Gimeno, L., Stohl, A., Trigo, R. M., Dominguez, F., Yoshimura, K., Yu, L., Drumond, A., Durán-Quesada, A. M., and Nieto, R. (2012). Oceanic and terrestrial sources of continental precipitation. *Reviews of Geophysics*, 50(4).

Hall, N. M. J., Hoskins, B. J., Valdes, P. J., and Senior, C. A. (1994). Storm tracks in a high-resolution GCM with doubled carbon dioxide. *Quar-*

terly Journal of the Royal Meteorological Society, 120(519):1209–1230. _eprint: https://onlinelibrary.wiley.com/doi/pdf/10.1002/qj.49712051905.

Hansen, J., Sato, M., Ruedy, R., Nazarenko, L., Lacis, A., Schmidt, G. A., Russell, G., Aleinov, I., Bauer, M., Bauer, S., Bell, N., Cairns, B., Canuto, V., Chandler, M., Cheng, Y., Del Genio, A., Faluvegi, G., Fleming, E., Friend, A., Hall, T., Jackman, C., Kelley, M., Kiang, N., Koch, D., Lean, J., Lerner, J., Lo, K., Menon, S., Miller, R., Minnis, P., Novakov, T., Oinas, V., Perlwitz, J., Perlwitz, J., Rind, D., Romanou, A., Shindell, D., Stone, P., Sun, S., Tausnev, N., Thresher, D., Wielicki, B., Wong, T., Yao, M., and Zhang, S. (2005). Efficacy of climate forcings. *Journal of Geophysical Research: Atmospheres*, 110(D18).

Held, I. M. and Soden, B. J. (2006). Robust Responses of the Hydrological Cycle to Global Warming. *Journal of Climate*, 19(21):5686–5699.

Heyblom, K. B., Singh, H. A., Rasch, P. J., and DeRepentigny, P. (2022). Increased Variability of Biomass Burning Emissions in CMIP6 Amplifies Hydrologic Cycle in the CESM2 Large Ensemble. *Geophysical Research Letters*, 49(5):e2021GL096868.

Heyblom, K. B., Singh, H. A., Rasch, P. J., and Hirasawa, H. (2023). Variability in Biomass Burning Emissions Weakens Aerosol Forcing Due To Nonlinear Aerosol-Cloud Interactions. *Geophysical Research Letters*, 50(11):e2022GL102685.

Hoesly, R. M., Smith, S. J., Feng, L., Klimont, Z., Janssens-Maenhout, G., Pitkanen, T., Seibert, J. J., Vu, L., Andres, R. J., Bolt, R. M., Bond, T. C., Dawidowski, L., Kholod, N., Kurokawa, J.-i., Li, M., Liu, L., Lu, Z., Moura, M. C. P., O'Rourke, P. R., and Zhang, Q. (2018). Historical (1750–2014) anthropogenic emissions of reactive gases and aerosols from the Community Emissions Data System (CEDS). *Geoscientific Model Development*, 11(1):369–408.

Hunke, E. C., Lipscomb, W. H., Turner, A. K., Jeffery, N., and Elliot, S. (2015). CICE: The los alamos sea ice model documentation and software user's manual version 5.1. Technical Report LA-CC-06-012, Los Alamos National Laboratory.

Hwang, Y.-T. and Frierson, D. M. W. (2010). Increasing atmospheric poleward energy transport with global warming. *Geophysical Research Letters*, 37(24).

Jungclaus, J. H., Bard, E., Baroni, M., Braconnot, P., Cao, J., Chini, L. P., Egorova, T., Evans, M., González-Rouco, J. F., Goosse, H., Hurtt, G. C., Joos, F., Kaplan,

J. O., Khodri, M., Klein Goldewijk, K., Krivova, N., LeGrande, A. N., Lorenz, S. J., Luterbacher, J., Man, W., Maycock, A. C., Meinshausen, M., Moberg, A., Muscheler, R., Nehrbass-Ahles, C., Otto-Bliesner, B. I., Phipps, S. J., Pongratz, J., Rozanov, E., Schmidt, G. A., Schmidt, H., Schmutz, W., Schurer, A., Shapiro, A. I., Sigl, M., Smerdon, J. E., Solanki, S. K., Timmreck, C., Toohey, M., Usoskin, I. G., Wagner, S., Wu, C.-J., Yeo, K. L., Zanchettin, D., Zhang, Q., and Zorita, E. (2017). The PMIP4 contribution to CMIP6 – Part 3: The last millennium, scientific objective, and experimental design for the PMIP4 *past1000* simulations. *Geoscientific Model Development*, 10(11):4005–4033. Publisher: Copernicus GmbH.

Kacarab, M., Thornhill, K. L., Dobracki, A., Howell, S. G., O'Brien, J. R., Freitag, S., Poellot, M. R., Wood, R., Zuidema, P., Redemann, J., and Nenes, A. (2020). Biomass burning aerosol as a modulator of the droplet number in the southeast Atlantic region. *Atmospheric Chemistry and Physics*, 20(5):3029–3040.

Kang, S. M., Held, I. M., Frierson, D. M. W., and Zhao, M. (2008). The Response of the ITCZ to Extratropical Thermal Forcing: Idealized Slab-Ocean Experiments with a GCM. *Journal of Climate*, 21(14):3521–3532.

Kiehl, J. T. (2007). Twentieth century climate model response and climate sensitivity. *Geophysical Research Letters*, 34(22).

Kravitz, B., Robock, A., Tilmes, S., Boucher, O., English, J. M., Irvine, P. J., Jones, A., Lawrence, M. G., MacCracken, M., Muri, H., Moore, J. C., Niemeier, U., Phipps, S. J., Sillmann, J., Storelvmo, T., Wang, H., and Watanabe, S. (2015). The Geoengineering Model Intercomparison Project Phase 6 (GeoMIP6): simulation design and preliminary results. *Geoscientific Model Development*, 8(10):3379–3392.

Kvalevåg, M. M., Samset, B. H., and Myhre, G. (2013). Hydrological sensitivity to greenhouse gases and aerosols in a global climate model. *Geophysical Research Letters*, 40(7):1432–1438.

Lamarque, J.-F., Bond, T. C., Eyring, V., Granier, C., Heil, A., Klimont, Z., Lee, D., Liousse, C., Mieville, A., Owen, B., Schultz, M. G., Shindell, D., Smith, S. J., Stehfest, E., Van Aardenne, J., Cooper, O. R., Kainuma, M., Mahowald, N., McConnell, J. R., Naik, V., Riahi, K., and van Vuuren, D. P. (2010). Historical (1850–2000) gridded anthropogenic and biomass burning emissions of reactive gases

and aerosols: methodology and application. *Atmospheric Chemistry and Physics*, 10(15):7017–7039.

Lau, W. K. M. and Kim, K.-M. (2015). Robust Hadley Circulation changes and increasing global dryness due to CO2 warming from CMIP5 model projections. *Proceedings of the National Academy of Sciences*, 112(12):3630–3635. Publisher: Proceedings of the National Academy of Sciences.

Lau, W. K.-M., Wu, H.-T., and Kim, K.-M. (2013). A canonical response of precipitation characteristics to global warming from CMIP5 models. *Geophysical Research Letters*, 40(12):3163–3169. _eprint: https://onlinelibrary.wiley.com/doi/pdf/10.1002/grl.50420.

Lawrence, D. M., Fisher, R. A., Koven, C. D., Oleson, K. W., Swenson, S. C., Bonan, G., Collier, N., Ghimire, B., van Kampenhout, L., Kennedy, D., Kluzek, E., Lawrence, P. J., Li, F., Li, H., Lombardozzi, D., Riley, W. J., Sacks, W. J., Shi, M., Vertenstein, M., Wieder, W. R., Xu, C., Ali, A. A., Badger, A. M., Bisht, G., van den Broeke, M., Brunke, M. A., Burns, S. P., Buzan, J., Clark, M., Craig, A., Dahlin, K., Drewniak, B., Fisher, J. B., Flanner, M., Fox, A. M., Gentine, P., Hoffman, F., Keppel-Aleks, G., Knox, R., Kumar, S., Lenaerts, J., Leung, L. R., Lipscomb, W. H., Lu, Y., Pandey, A., Pelletier, J. D., Perket, J., Randerson, J. T., Ricciuto, D. M., Sanderson, B. M., Slater, A., Subin, Z. M., Tang, J., Thomas, R. Q., Martin, M. V., and Zeng, X. (2019). The community land model version 5: Description of new features, benchmarking, and impact of forcing uncertainty. *Journal of Advances in Modeling Earth Systems*, 11(12):4245–4287.

Liu, C. and Allan, R. P. (2013). Observed and simulated precipitation responses in wet and dry regions 1850–2100. *Environmental Research Letters*, 8(3):034002. Publisher: IOP Publishing.

Liu, X., Ma, P.-L., Wang, H., Tilmes, S., Singh, B., Easter, R. C., Ghan, S. J., and Rasch, P. J. (2016). Description and evaluation of a new four-mode version of the Modal Aerosol Module (MAM4) within version 5.3 of the Community Atmosphere Model. *Geoscientific Model Development*, 9(2):505–522.

Lorenz, D. J. (2014). Understanding Midlatitude Jet Variability and Change Using Rossby Wave Chromatography: Poleward-Shifted Jets in Response to External

Forcing. *Journal of the Atmospheric Sciences*, 71(7):2370–2389. Publisher: American Meteorological Society Section: Journal of the Atmospheric Sciences.

Läderach, A. and Sodemann, H. (2016). A revised picture of the atmospheric moisture residence time. *Geophysical Research Letters*, 43(2):924–933.

Manabe, S. and Wetherald, R. T. (1975). The Effects of Doubling the CO2 Concentration on the climate of a General Circulation Model. *Journal of the Atmospheric Sciences*, 32(1):3–15. Publisher: American Meteorological Society Section: Journal of the Atmospheric Sciences.

Marshall, J., Ferreira, D., Campin, J.-M., and Enderton, D. (2007). Mean Climate and Variability of the Atmosphere and Ocean on an Aquaplanet. *Journal of the Atmospheric Sciences*, 64(12):4270–4286.

Mekonnen, M. M. and Hoekstra, A. Y. (2016). Four billion people facing severe water scarcity. *Science Advances*, 2(2):e1500323. Publisher: American Association for the Advancement of Science.

Ming, Y., Ramaswamy, V., and Persad, G. (2010). Two opposing effects of absorbing aerosols on global-mean precipitation. *Geophysical Research Letters*, 37(13).

Miranda, J. J., Scholz, I., Agard, J., Al-Ghanim, K., Bobylev, S. N., Dube, O. P., Hathie, I., Kanie, N., Madise, N. J., Malekpour, S., Montoya, J. C., Pan, J., Persson, A., Sagar, A., and Shackell, N. (2023). *Global Sustainable Development Report 2023: Times of crisis, times of change: Science for accelerating transformations to sustainable development*. United Nations.

Mitchell, J. F. B., Wilson, C. A., and Cunnington, W. M. (1987). On Co2 climate sensitivity and model dependence of results. *Quarterly Journal of the Royal Meteorological Society*, 113(475):293–322.

Muller, C. J. and O'Gorman, P. A. (2011). An energetic perspective on the regional response of precipitation to climate change. *Nature Climate Change*, 1(5):266–271.

Myhre, G., Forster, P. M., Samset, B. H., Hodnebrog, O., Sillmann, J., Aalbergsjø, S. G., Andrews, T., Boucher, O., Faluvegi, G., Fläschner, D., Iversen, T., Kasoar, M., Kharin, V., Kirkevåg, A., Lamarque, J.-F., Olivié, D., Richardson, T. B., Shindell, D., Shine, K. P., Stjern, C. W., Takemura, T., Voulgarakis, A., and Zwiers,

F. (2017). PDRMIP: A Precipitation Driver and Response Model Intercomparison Project—Protocol and Preliminary Results. *Bulletin of the American Meteorological Society*, 98(6):1185–1198.

Neale, R. B. and Hoskins, B. J. (2000). A standard test for AGCMs including their physical parametrizations: I: the proposal. *Atmospheric Science Letters*, 1(2):101–107.

O'Gorman, P. A. and Schneider, T. (2009). The physical basis for increases in precipitation extremes in simulations of 21st-century climate change. *Proceedings of the National Academy of Sciences*, 106(35):14773–14777.

O'Neill, B. C., Tebaldi, C., van Vuuren, D. P., Eyring, V., Friedlingstein, P., Hurtt, G., Knutti, R., Kriegler, E., Lamarque, J.-F., Lowe, J., Meehl, G. A., Moss, R., Riahi, K., and Sanderson, B. M. (2016). The Scenario Model Intercomparison Project (ScenarioMIP) for CMIP6. *Geoscientific Model Development*, 9(9):3461–3482.

O'Gorman, P. A., Allan, R. P., Byrne, M. P., and Previdi, M. (2012). Energetic Constraints on Precipitation Under Climate Change. *Surveys in Geophysics*, 33(3):585–608.

O'Gorman, P. A. and Muller, C. J. (2010). How closely do changes in surface and column water vapor follow Clausius–Clapeyron scaling in climate change simulations? *Environmental Research Letters*, 5(2):025207.

Pandis, S. N., Harley, R. A., Cass, G. R., and Seinfeld, J. H. (1992). Secondary organic aerosol formation and transport. *Atmospheric Environment. Part A. General Topics*, 26(13):2269–2282.

Peixoto, J. P. and Oort, A. H. (1992). *Physics of Climate*. American Institute of Physics.

Pendergrass, A. G., Conley, A., and Vitt, F. M. (2018). Surface and top-of-atmosphere radiative feedback kernels for CESM-CAM5. *Earth System Science Data*, 10(1):317–324.

Pendergrass, A. G. and Hartmann, D. L. (2014). Changes in the Distribution of Rain Frequency and Intensity in Response to Global Warming. *Journal of Climate*, 27(22):8372–8383.

Pincus, R., Forster, P. M., and Stevens, B. (2016). The Radiative Forcing Model Intercomparison Project (RFMIP): experimental protocol for CMIP6. *Geoscientific Model Development*, 9(9):3447–3460.

Polson, D., Hegerl, G. C., Allan, R. P., and Sarojini, B. B. (2013). Have greenhouse gases intensified the contrast between wet and dry regions? *Geophysical Research Letters*, 40(17):4783–4787. _eprint: https://onlinelibrary.wiley.com/doi/pdf/10.1002/grl.50923.

Previdi, M. (2010). Radiative feedbacks on global precipitation. *Environmental Research Letters*, 5(2):025211.

Ramanathan, V., Crutzen, P. J., Kiehl, J. T., and Rosenfeld, D. (2001). Aerosols, Climate, and the Hydrological Cycle. *Science*, 294(5549):2119–2124.

Reutter, P., Su, H., Trentmann, J., Simmel, M., Rose, D., Gunthe, S. S., Wernli, H., Andreae, M. O., and Poschl, U. (2009). Aerosol- and updraft-limited regimes of cloud droplet formation: influence of particle number, size and hygroscopicity on the activation of cloud condensation nuclei (CCN). *Atmos. Chem. Phys.*, page 14.

Riahi, K., van Vuuren, D. P., Kriegler, E., Edmonds, J., O'Neill, B. C., Fujimori, S., Bauer, N., Calvin, K., Dellink, R., Fricko, O., Lutz, W., Popp, A., Cuaresma, J. C., KC, S., Leimbach, M., Jiang, L., Kram, T., Rao, S., Emmerling, J., Ebi, K., Hasegawa, T., Havlik, P., Humpenöder, F., Da Silva, L. A., Smith, S., Stehfest, E., Bosetti, V., Eom, J., Gernaat, D., Masui, T., Rogelj, J., Strefler, J., Drouet, L., Krey, V., Luderer, G., Harmsen, M., Takahashi, K., Baumstark, L., Doelman, J. C., Kainuma, M., Klimont, Z., Marangoni, G., Lotze-Campen, H., Obersteiner, M., Tabeau, A., and Tavoni, M. (2017). The Shared Socioeconomic Pathways and their energy, land use, and greenhouse gas emissions implications: An overview. *Global Environmental Change*, 42:153–168.

Richardson, T. B., Forster, P. M., Andrews, T., Boucher, O., Faluvegi, G., Fläschner, D., Hodnebrog, O., Kasoar, M., Kirkevåg, A., Lamarque, J.-F., Myhre, G., Olivié, D., Samset, B. H., Shawki, D., Shindell, D., Takemura, T., and Voulgarakis, A. (2018). Drivers of Precipitation Change: An Energetic Understanding. *Journal of Climate*, 31(23):9641–9657.

Richardson, T. B., Forster, P. M., Andrews, T., and Parker, D. J. (2016). Understanding the Rapid Precipitation Response to CO2 and Aerosol Forcing on a Regional Scale*. *Journal of Climate*, 29(2):583–594.

Richter, I. and Xie, S.-P. (2008). Muted precipitation increase in global warming simulations: A surface evaporation perspective. *Journal of Geophysical Research: Atmospheres*, 113(D24).

Rissman, T. A., Nenes, A., and Seinfeld, J. H. (2004). Chemical Amplification (or Dampening) of the Twomey Effect: Conditions Derived from Droplet Activation Theory. *Journal of the Atmospheric Sciences*, 61(8):919–930.

Rodgers, K. B., Lee, S.-S., Rosenbloom, N., Timmermann, A., Danabasoglu, G., Deser, C., Edwards, J., Kim, J.-E., Simpson, I. R., Stein, K., Stuecker, M. F., Yamaguchi, R., Bódai, T., Chung, E.-S., Huang, L., Kim, W. M., Lamarque, J.-F., Lombardozzi, D. L., Wieder, W. R., and Yeager, S. G. (2021). Ubiquity of human-induced changes in climate variability. *Earth System Dynamics*, 12(4):1393–1411.

Samset, B. H., Myhre, G., Forster, P. M., Hodnebrog, O., Andrews, T., Faluvegi, G., Fläschner, D., Kasoar, M., Kharin, V., Kirkevåg, A., Lamarque, J.-F., Olivié, D., Richardson, T., Shindell, D., Shine, K. P., Takemura, T., and Voulgarakis, A. (2016). Fast and slow precipitation responses to individual climate forcers: A PDRMIP multimodel study. *Geophysical Research Letters*, 43(6):2782–2791.

Scheff, J. and Frierson, D. (2012a). Twenty-First-Century Multimodel Subtropical Precipitation Declines Are Mostly Midlatitude Shifts. *Journal of Climate*, 25(12):4330–4347. Publisher: American Meteorological Society Section: Journal of Climate.

Scheff, J. and Frierson, D. M. W. (2012b). Robust future precipitation declines in CMIP5 largely reflect the poleward expansion of model subtropical dry zones. *Geophysical Research Letters*, 39(18). _eprint: https://onlinelibrary.wiley.com/doi/pdf/10.1029/2012GL052910.

Schewe, J., Heinke, J., Gerten, D., Haddeland, I., Arnell, N. W., Clark, D. B., Dankers, R., Eisner, S., Fekete, B. M., Colón-González, F. J., Gosling, S. N., Kim, H., Liu, X., Masaki, Y., Portmann, F. T., Satoh, Y., Stacke, T., Tang, Q., Wada, Y., Wisser, D., Albrecht, T., Frieler, K., Piontek, F., Warszawski, L., and Kabat, P.

(2014). Multimodel assessment of water scarcity under climate change. *Proceedings of the National Academy of Sciences*, 111(9):3245–3250. Publisher: Proceedings of the National Academy of Sciences.

Seager, R. and Naik, N. (2012). A Mechanisms-Based Approach to Detecting Recent Anthropogenic Hydroclimate Change. *Journal of Climate*, 25(1):236–261. Publisher: American Meteorological Society Section: Journal of Climate.

Seager, R., Naik, N., and Vecchi, G. A. (2010). Thermodynamic and Dynamic Mechanisms for Large-Scale Changes in the Hydrological Cycle in Response to Global Warming. *Journal of Climate*, 23(17):4651–4668.

Seager, R., Ting, M., Held, I., Kushnir, Y., Lu, J., Vecchi, G., Huang, H.-P., Harnik, N., Leetmaa, A., Lau, N.-C., Li, C., Velez, J., and Naik, N. (2007). Model Projections of an Imminent Transition to a More Arid Climate in Southwestern North America. *Science*, 316(5828):1181–1184. Publisher: American Association for the Advancement of Science.

Seidel, D. J., Fu, Q., Randel, W. J., and Reichler, T. J. (2008). Widening of the tropical belt in a changing climate. *Nature Geoscience*, 1(1):21–24. Publisher: Nature Publishing Group.

Seinfeld, J. H., Bretherton, C., Carslaw, K. S., Coe, H., DeMott, P. J., Dunlea, E. J., Feingold, G., Ghan, S., Guenther, A. B., Kahn, R., Kraucunas, I., Kreidenweis, S. M., Molina, M. J., Nenes, A., Penner, J. E., Prather, K. A., Ramanathan, V., Ramaswamy, V., Rasch, P. J., Ravishankara, A. R., Rosenfeld, D., Stephens, G., and Wood, R. (2016). Improving our fundamental understanding of the role of aerosolcloud interactions in the climate system. *Proceedings of the National Academy of Sciences*, 113(21):5781–5790. Publisher: Proceedings of the National Academy of Sciences.

Siler, N., Bailey, A., Roe, G. H., Buizert, C., Markle, B., and Noone, D. (2021). The Large-Scale, Long-Term Coupling of Temperature, Hydrology, and Water Isotopes. *Journal of Climate*, 34(16):6725–6742.

Siler, N., Bonan, D. B., and Donohoe, A. (2023). Diagnosing Mechanisms of Hydrologic Change under Global Warming in the CESM1 Large Ensemble. *Journal of Climate*, 36(23):8243–8257.

Siler, N., Roe, G. H., and Armour, K. C. (2018). Insights into the Zonal-Mean Response of the Hydrologic Cycle to Global Warming from a Diffusive Energy Balance Model. *Journal of Climate*, 31(18):7481–7493.

Singh, H. A., Bitz, C. M., Nusbaumer, J., and Noone, D. C. (2016a). A mathematical framework for analysis of water tracers: Part 1: Development of theory and application to the preindustrial mean state. *Journal of Advances in Modeling Earth Systems*, 8(2):991–1013.

Singh, H. K. A., Bitz, C. M., Donohoe, A., Nusbaumer, J., and Noone, D. C. (2016b). A Mathematical Framework for Analysis of Water Tracers. Part II: Understanding Large-Scale Perturbations in the Hydrological Cycle due to CO2 Doubling. *Journal of Climate*, 29(18):6765–6782.

Singh, H. K. A., Bitz, C. M., Donohoe, A., and Rasch, P. J. (2017). A Source–Receptor Perspective on the Polar Hydrologic Cycle: Sources, Seasonality, and Arctic–Antarctic Parity in the Hydrologic Cycle Response to CO2 Doubling. *Journal of Climate*, 30(24):9999–10017.

Smith, C., Nicholls, Z., Armour, K., Collins, W., Forster, P., Meinshausen, M., Palmer, M., and Watanabe, M. (2021). The Earth's Energy Budget, Climate Feedbacks, and Climate Sensitivity Supplementary Material. In Masson-Delmotte, V., Zhai, P., Pirani, A., Connors, S., Péan, C., Berger, S., Caud, N., Chen, Y., Goldfarb, L., Gomis, M., Huang, M., Leitzell, K., Lonnoy, E., Matthews, J., Maycock, T., Waterfield, T., Yelekçi, O., Yu, R., and Zhou, B., editors, *Climate Change 2021: The Physical Science Basis. Contribution of Working Group I to the Sixth Assessment Report of the Intergovernmental Panel on Climate Change*.

Smith, C. J., Kramer, R. J., Myhre, G., Alterskjær, K., Collins, W., Sima, A., Boucher, O., Dufresne, J.-L., Nabat, P., Michou, M., Yukimoto, S., Cole, J., Paynter, D., Shiogama, H., O'Connor, F. M., Robertson, E., Wiltshire, A., Andrews, T., Hannay, C., Miller, R., Nazarenko, L., Kirkevåg, A., Olivié, D., Fiedler, S., Lewinschal, A., Mackallah, C., Dix, M., Pincus, R., and Forster, P. M. (2020). Effective radiative forcing and adjustments in CMIP6 models. *Atmospheric Chemistry and Physics*, 20(16):9591–9618.

Smith, C. J., Kramer, R. J., Myhre, G., Forster, P. M., Soden, B. J., Andrews, T., Boucher, O., Faluvegi, G., Fläschner, D., Hodnebrog, O., Kasoar, M., Kharin,

V., Kirkevåg, A., Lamarque, J.-F., Mülmenstädt, J., Olivié, D., Richardson, T., Samset, B. H., Shindell, D., Stier, P., Takemura, T., Voulgarakis, A., and Watson-Parris, D. (2018). Understanding Rapid Adjustments to Diverse Forcing Agents. *Geophysical Research Letters*, 45(21):12,023–12,031.

Smith, R., Jones, P., Briegleb, B., Bryan, F., Danabasoglu, G., Dennis, J., Dukowicz, J., Eden, C., Fox-Kemper, B., Gent, P., Hecht, M., Jayne, S., Jochum, M., Large, W., Lindsay, K., Maltrud, M., Norton, N., Peacock, S., Vertenstein, M., and Yeager, S. (2010). The Parallel Ocean Program (POP) reference, manual ocean component of the Community Climate System Model (CCSM) and Community Earth System Model (CESM). *LANL Tech. Report*.

Stephens, G. L., Slingo, A., Webb, M. J., Minnett, P. J., Daum, P. H., Kleinman, L., Wittmeyer, I., and Randall, D. A. (1994). Observations of the Earth's Radiation Budget in relation to atmospheric hydrology: 4. Atmospheric column radiative cooling over the world's oceans. *Journal of Geophysical Research: Atmospheres*, 99(D9):18585–18604. _eprint: https://onlinelibrary.wiley.com/doi/pdf/10.1029/94JD01151.

Stott, P. A., Gillett, N. P., Hegerl, G. C., Karoly, D. J., Stone, D. A., Zhang, X., and Zwiers, F. (2010). Detection and attribution of climate change: a regional perspective. *WIREs Climate Change*, 1(2):192–211. _eprint: https://onlinelibrary.wiley.com/doi/pdf/10.1002/wcc.34.

Szopa, S., Naik, V., Adhikary, B., Artaxo, P., Berntsen, T., Collins, W., Fuzzi, S., Gallardo, L., Kiendler-Scharr, A., Klimont, Z., Liao, H., Unger, N., and Zanis, P. (2021). Short-Lived Climate Forcers. In Masson-Delmotte, V., Zhai, P., Pirani, A., Connors, S., Péan, C., Berger, S., Caud, N., Chen, Y., Goldfarb, L., Gomis, M., Huang, M., Leitzell, K., Lonnoy, E., Matthews, J., Maycock, T., Waterfield, T., Yelekçi, O., Yu, R., and Zhou, B., editors, *Climate Change 2021: The Physical Science Basis. Contribution of Working Group I to the Sixth Assessment Report of the Intergovernmental Panel on Climate Change*, pages 817–922. Cambridge University Press, Cambridge, United Kingdom and New York, NY, USA.

Taylor, K. E., Stouffer, R. J., and Meehl, G. A. (2012). An Overview of CMIP5 and the Experiment Design. *Bulletin of the American Meteorological Society*, 93(4):485–498.

Trenberth, K. E. (1999). Conceptual Framework for Changes of Extremes of the Hydrological Cycle with Climate Change. *Climatic Change*, 42(1):327–339.

Trenberth, K. E., Dai, A., Rasmussen, R. M., and Parsons, D. B. (2003). The Changing Character of Precipitation. *Bulletin of the American Meteorological Society*, 84(9):1205–1218.

Twomey, S. (1977). The Influence of Pollution on the Shortwave Albedo of Clouds. *Journal of Atmospheric Sciences*, 34(7):1149–1152.

Utsumi, N., Seto, S., Kanae, S., Maeda, E. E., and Oki, T. (2011). Does higher surface temperature intensify extreme precipitation? *Geophysical Research Letters*, 38(16).

Vallis, G. K., Zurita-Gotor, P., Cairns, C., and Kidston, J. (2015). Response of the large-scale structure of the atmosphere to global warming. *Quarterly Journal of the Royal Meteorological Society*, 141(690):1479–1501. _eprint: https://onlinelibrary.wiley.com/doi/pdf/10.1002/qj.2456.

van der Ent, R. J. and Savenije, H. H. G. (2011). Length and time scales of atmospheric moisture recycling. *Atmospheric Chemistry and Physics*, 11(5):1853–1863.

van der Ent, R. J. and Tuinenburg, O. A. (2017). The residence time of water in the atmosphere revisited. *Hydrology and Earth System Sciences*, 21(2):779–790.

van der Werf, G. R., Randerson, J. T., Giglio, L., van Leeuwen, T. T., Chen, Y., Rogers, B. M., Mu, M., van Marle, M. J. E., Morton, D. C., Collatz, G. J., Yokelson, R. J., and Kasibhatla, P. S. (2017). Global fire emissions estimates during 1997–2016. *Earth System Science Data*, 9(2):697–720.

van Marle, M. J. E., Kloster, S., Magi, B. I., Marlon, J. R., Daniau, A.-L., Field, R. D., Arneth, A., Forrest, M., Hantson, S., Kehrwald, N. M., Knorr, W., Lasslop, G., Li, F., Mangeon, S., Yue, C., Kaiser, J. W., and van der Werf, G. R. (2017). Historic global biomass burning emissions for CMIP6 (BB4CMIP) based on merging satellite observations with proxies and fire models (1750–2015). *Geoscientific Model Development*, 10(9):3329–3357.

Wallace, J. and Hobbs, P. (2006). *Atmospheric Science: An Introductory Survey*. International geophysics series. Elsevier Academic Press.

Wilks, D. S. (2016). "The Stippling Shows Statistically Significant Grid Points": How Research Results are Routinely Overstated and Overinterpreted, and What to Do about It. *Bulletin of the American Meteorological Society*, 97(12):2263–2273.

Yin, J. H. (2005). A consistent poleward shift of the storm tracks in simulations of 21st century climate. *Geophysical Research Letters*, 32(18). _eprint: https://onlinelibrary.wiley.com/doi/pdf/10.1029/2005GL023684.

Zanchettin, D., Khodri, M., Timmreck, C., Toohey, M., Schmidt, A., Gerber, E. P., Hegerl, G., Robock, A., Pausata, F. S. R., Ball, W. T., Bauer, S. E., Bekki, S., Dhomse, S. S., LeGrande, A. N., Mann, G. W., Marshall, L., Mills, M., Marchand, M., Niemeier, U., Poulain, V., Rozanov, E., Rubino, A., Stenke, A., Tsigaridis, K., and Tummon, F. (2016). The Model Intercomparison Project on the climatic response toVolcanic forcing (VolMIP): experimental design and forcing input data for CMIP6. *Geoscientific Model Development*, 9(8):2701–2719.

Zelinka, M. D., Myers, T. A., McCoy, D. T., Po-Chedley, S., Caldwell, P. M., Ceppi, P., Klein, S. A., and Taylor, K. E. (2020). Causes of Higher Climate Sensitivity in CMIP6 Models. *Geophysical Research Letters*, 47(1):e2019GL085782.